UNIVERSITY OF PATRAS

SCHOOL OF NATURAL SCIENCES

DEPARTMENT OF MATERIAL SCIENCE

“DEVELOPMENT AND INVESTIGATION OF MICROSTRUCTURES BY USE OF LASER FOR PHOTONIC APPLICATIONS”

PhD THESIS

LOUKAS ATHANASEKOS

April 2014

UNIVERSITY OF PATRAS

SCHOOL OF NATURAL SCIENCES

DEPARTMENT OF MATERIAL SCIENCE

“DEVELOPMENT AND INVESTIGATION OF MICROSTRUCTURES BY USE OF LASER FOR PHOTONIC APPLICATIONS”

PhD THESIS

LOUKAS ATHANASEKOS

ΠΑΝΕΠΙΣΤΗΜΙΟ
ΠΑΤΡΩΝ
UNIVERSITY OF PATRAS

Ευρωπαϊκή Ένωση
Ευρωπαϊκό Κοινωνικό Ταμείο

ΕΠΙΧΕΙΡΗΣΙΑΚΟ ΠΡΟΓΡΑΜΜΑ
ΕΚΠΑΙΔΕΥΣΗ ΚΑΙ ΔΙΑ ΒΙΟΥ ΜΑΘΗΣΗ
επένδυση στην κοινωνία της γνώσης
ΥΠΟΥΡΓΕΙΟ ΠΑΙΔΕΙΑΣ ΚΑΙ ΘΡΗΣΚΕΥΜΑΤΩΝ
ΕΙΔΙΚΗ ΥΠΗΡΕΣΙΑ ΔΙΑΧΕΙΡΙΣΗΣ

ΕΣΠΑ
2007-2013
πρόγραμμα για την ανάπτυξη
ΕΥΡΩΠΑΪΚΟ ΚΟΙΝΩΝΙΚΟ ΤΑΜΕΙΟ

Με τη συγχρηματοδότηση της Ελλάδας και της Ευρωπαϊκής Ένωσης

April 2014

SUPERVISING COMMITTEE

1. **Nikolaos A. Vainos**, Department of Material Science, University of Patras, Greece (Supervisor)
2. **Robert W. Eason**, Optoelectronics Research Centre, University of Southampton, UK
3. **Asterios Pispas**, Theoretical & Physical Chemistry Institute, National Hellenic Reasearch Foundation, Greece

EXAMINATION COMMITTEE

1. **Nikolaos A. Vainos**, Department of Material Science, University of Patras, Greece
2. **Robert W. Eason**, Optoelectronics Research Centre, University of Southampton, UK
3. **Asterios Pispas**, Theoretical & Physical Chemistry Institute, National Hellenic Reasearch Foundation, Greece
4. **Stelios Couris,** Department of Physics, University of Patras, Greece
5. **Alexandros Vanakaras,** Department of Material Science, University of Patras, Greece
6. **Emmanuel Paspalakis,** Department of Material Science, University of Patras, Greece
7. **Sotirios Baskoutas,** Department of Material Science, University of Patras, Greece

“There are two ways of spreading light; to be the candle or the mirror that reflects it”, Edith Wharton, American novelist

“Dare to reach out your hand into the darkness, to pull another hand into the light”, Norman B. Rice, 49th mayor of Seattle

Abstract

In the current PhD thesis a thorough study is performed on the design, fabrication and analysis of microstructures created by use of laser methods. The work comprises the design and fabrication of organic, inorganic and hybrid microstructures for use in photonics applications. In addition, several techniques are applied for the fabrication and replication of photonic diffractive microstructures. Fabricated structures are tested as potential functional photonic sensors for humidity, ammonia and temperature detection. Furthermore, a detailed study on polymer-based microstructures creation by laser radiation forces is attempted both theoretically and experimentally. The created 2D and 3D free-standing micro/nanostructures are optically characterized.

Περίληψη

Στην παρούσα διδακτορική διατριβή παρουσιάζεται μια ενδελεχής μελέτη στην σχεδίαση, κατασκευή και ανάλυση μικροδομών που δημιουργούνται με τη χρήση δέσμης λέιζερ. Η εργασία περιλαμβάνει τον σχεδιασμό και την κατασκευή οργανικών, ανόργανων και υβριδικών μικροδομών για χρήση τους σε εφαρμογές φωτονικής. Επιπρόσθετα, εφαρμόζονται διάφορες τεχνικές για την κατασκευή και αναπαραγωγή φωτονικών περιθλαστικών μικροδομών. Οι δομές ελέγχονται ως λειτουργικοί φωτονικοί αισθητήρες για την ανίχνευση υγρασίας, αμμωνίας και θερμοκρασίας. Ακόμα, πραγματοποιείται μια λεπτομερής μελέτη πάνω στη δημιουργία μικροδομών βασισμένων σε πολυμερή με χρήση δυνάμεων ακτινοβολίας λέιζερ τόσο σε θεωρητικό όσο και σε πειραματικό επίπεδο. Οι δημιουργούμενες δισδιάστατες και τρισδιάστατες μικρο/νανοδομές ελεύθερου χώρου χαρακτηρίζονται οπτικά.

Thesis outline

The work is divided into six chapters. The first chapter is an introductory overview on micro/nanofabrication and laser materials processing where the main concepts are discussed. The second chapter is dedicated to the concept of direct laser microfabrication for polymeric and hybrid structures. A comparative study on the effect of 193 and 157nm excimer laser irradiation on TMOS-$NiCl_2$ sol-gel material is performed to reveal ablation characteristics. Furthermore, irradiation of 193nm excimer laser light on Polydimethylsiloxane (PDMS) and polymeric/hybrid materials (Polydimethylsiloxane (PDMS), Polyisoprene- poly(acrylic acid) and TEOS-MAA-PEG :Au) is also studied. The chapter concludes with the investigation of 193nm excimer laser microprocessing on Polymer Optical Fibers (POFs) with a view to utilizing them as photonic sensors.

The next chapter is dedicated to rapid prototyping and replication of optical microstructures. In more detail, the work comprises the design of Diffractive Optical Elements (D.O.E.) such as diffraction gratings and Fresnel lenses of various characteristics, by using special CAD software. Prior to the fabrication, a thorough calculation is performed for the determination of the fabrication characteristics e.g. radius of each zone. The final designs are then transferred to actual devices mainly for sensing applications.

Computer Generated Holography is also employed in order to obtain designs of complex shape and functionalities, mainly for optical interconnect applications. A plethora of designs is obtained, each one producing a different fanout, according to specific application needs. Designs are transferred to metal substrates and can be used in many photonic applications. Moreover, soft lithography techniques are used in order to obtain microstructures (diffraction gratings) for sensing applications. Diffraction gratings are fabricated by negative photolithography and the use of commercial photo resist. Subsequently, they were coated with a suitable layer to form a complex system comprising modulated effective index of refraction and modified surface grating profiles. The devices created are then utilized as potential relative humidity (RH) photonic sensors.

The capability of the rapid prototyping soft lithographic techniques for the efficient replication of gratings with efficient incorporation of various sensing materials is demonstrated and compared to classical prototyping photolithographic techniques. A modified Solvent Assisted MicroMolding (SAMIM) technique with fewer processing steps in the production of the grating is proposed. Diffractive structures are successfully created on thin films with the aid of an inkjet materials printer. The design, implementation and analysis of diffractive patterns with both organic and inorganic materials on silica substrates by use of an inkjet printer are performed. The chapter concludes with a dye deposition lithography attempt for sensing applications.

The fourth chapter discusses the concept of photonic structures for sensor applications. Diffractive gratings have been fabricated and tested as potential ammonia sensors. Furthermore, multilayer metal/metal-oxide diffraction gratings, fabricated with sputtering techniques, are tested in a photonic temperature sensing scheme. Prior to that, theoretical calculations are performed to obtain optimum fabrication parameter values.

The POF photonic sensors previously fabricated with the use of an excimer laser are tested for humidity and ammonia vapor sensing. The materials used comprised Cobalt Chloride ($CoCl_2$) / tetramethoxyorthosilicate (TMOS) based composite and a polystyrene sulfonate-b-*tert*-butylstyrene diblock copolymer. The results obtained confirm the efficient and low cost implementation of POF sensors for a variety of measurands.

The key role of laser radiation forces in the manipulation and fabrication of micro/nanostructures is thoroughly examined in Chapter 5. Radiation forces, chain entanglement and optical field structuring and waveguiding are extensively discussed in order to theoretically prove the mechanisms involved during the process. Following the proof of concept, a study on microstructure creation by laser radiation is carried out. Several forms of microstructures in planar and three-dimensional free standing micro-objects are demonstrated and discussed, in addition to a unique polymer fiber drawing operation, by the sole use of radiation forces. Emerging concepts on materials microstructuring in two and three dimensions would take advantage of the chemically inert nature of the process to yield a rich palette of microfabrication tools.

The thesis is concluded in chapter 6, emphasizing the main results obtained during the current work and giving future prospects.

Acknowledgments

This research has been co-financed by the European Union (European Social Fund – ESF) and Greek national funds through the Operational Program "Education and Lifelong Learning" of the National Strategic Reference Framework (NSRF) - Research Funding Program: Heracleitus II. Investing in knowledge society through the European Social Fund.

The current PhD research work has been performed in the Materials Science department of University of Patras and in the Theoretical and Physical Chemistry Institute, National Hellenic Research Foundation, Athens. First, I would like to thank all the committee for their useful notes and corrections and especially Prof. Eason for his remarks on both scientific and editing issues. Also, I would like to express my gratitude to my supervisor, Prof. Nikos Vainos, whose expertise, understanding, generous guidance and support made it possible for me to work on this exciting topic. Many thanks also go to Dr. Stergios Pispas and collaborators for the material synthesis and for giving their precious advice regarding the topic of my research. I would also like to thank Prof. Koutselas, Dr. Karoutsos and Dr. Alexandropoulos for their help and support throughout the last years. Many thanks go to Prof. Sigalas for his collaboration in the theoretical analysis and design of metal/oxide grating structures. Moreover, Prof. Toal and Dr. Naydenova from Dublin Institute of Technology are acknowledged for fruitful collaboration. In addition, Dr. Riziotis from NHRF is acknowledged for useful discussions. The collaboration, support and useful discussions on the exciting topic of structure creation by radiation forces with Prof. Fytas, Dr. Loppinet and Dr. Anyfantakis of FORTH-IESL Crete are gratefully acknowledged.

Finally, I am grateful to Miltos Vasileiadis for his invaluable cooperation, the many useful technical and scientific discussions, his help with the figures and his support. His thirst for knowledge has always been an inspiration for me. I would also like to thank all my teachers and colleagues who gave their faith in me and urged me to do better. Last, but not least, this dissertation would not have been possible without the support of my parents, Kostas and Efi, my sister, Maria and my wife, Eleni.

CONTENTS

1. Introduction

In 1967 Pierre Aigrain, a French scientist, coined the term “photonics” to describe a new field of study and enterprise that emerged as a synthesis of a number of disciplines all involved in the mastery of the photon: optics, material science, electrical engineering, nanotechnology, physics and chemistry. Its importance can be seen from the multitude of application sectors where photonics increasingly drives innovation, including information & communication, imaging, lighting, organic & large area electronics, displays, manufacturing, life sciences & health care as well as safety & security [1].

Since the advent of the first laser in 1960, photonics applications have made major contributions to many aspects of the economy. One of the most widely used photonics application is in telecommunications [2]. The successful introduction of optical fibers as a new medium for transferring huge data packages via optical pulses accelerated the further development in the field. Photonics applications are widely used in medicine, with the establishment of the biophotonics field [3]. The diversity of photonics becomes apparent, as it is used in the military for night vision and surveillance systems [4]. The necessity of photonics has been extended even in the area of aerospace. Propagation issues together with demanding applications relating to space require the use of advanced technological tools which have led to a plethora of photonic elements [5].

1.1 Interference and Diffraction: Optics & applications

One of the most important phenomena of photonics and optics is **interference** which is an optical effect occurring when two or more light beams are superimposed. For interference to occur there should be a spatial and temporal overlap of the two light fields, resulting in the sum of their separate amplitudes in the superimposed beams. Among other effects, interference governs the operation of interferometers [6], which are used for a wide range of applications, and are also the basis of holography [7].

Another interesting optical phenomenon is **diffraction**. Diffractive optics is based on the principle of diffraction which it is not considered in conventional optics. A diffractive optical element (DOE) consists of a periodic pattern, typically with a spacing comparable with the wavelength used. The function of the diffractive optical element is exclusively determined by the geometry and spatial variations in the width and depth of its fringe pattern. The pattern is recorded as refractive index variations of the film and hence the light phase is affected by the element.

1.2 Micro and Nanofabrication methods in photonics

The necessity for faster, smaller, cheaper and of course better devices has led the photonics field in the struggle for novel micro and nanofabrication techniques. The latter can be divided in two main categories: top-down and bottom-up processes [8]. The top-down processes involve the removal or reformation of atoms to create the desired structure. One of the most commonly used techniques falls under the general term of lithography, subcategories of which are photolithography, electron beam lithography, ion beam lithography, optical lithography and soft lithography, to name a few. Another top-down method comes under the general term of micromachining. This involves the use of a laser source with a wavelength suitable for the application needed. Common laser sources are excimer lasers, Nd:YAG lasers and CO_2 lasers, with a wavelength range from the UV up to the IR spectral region.

In the bottom-up processes, atoms, molecules or nanoparticles can be used as the building blocks for the creation of complex structures. Main techniques of that type, to name a few, are Physical Vapor Deposition, Chemical Vapor Deposition, plasma-assisted deposition such as magnetron sputtering, Molecular Beam Epitaxy and Electrodeposition.

1.3 Laser-Materials processing: Fundamentals-Interactions & Applications

Surface processing is crucial for the microfabrication of devices in order to become functional. Its absorption properties can be controlled by altering the texture [9]. Thus, multiscale surface modification is a critical factor in the development of new material structures.

The main advantage of the laser as a material processing tool is the ability to precisely control the exact location and rate that energy is deposited through the proper selection of laser processing parameters. The predominant methods for control include beam focusing and beam shaping with homogenizers [10], amplitude masks, refractive elements [11], and DOEs [12]. However, more advanced optical devices can be used such as spatial light modulators (SLMs) [13] and deformable mirrors [14], allowing real-time modulation of the beam’s intensity profile on the surface. There has been extensive work in the area of beam shaping with a number of articles and books [15]. In addition, once inside the material, absorption causes the light intensity to decay with depth at a rate determined by the material’s absorption coefficient. The optical penetration or absorption depth is defined as the length at which intensity of the transmitted light falls to e^{-1} of its initial value at the interface. Energy absorption is approximately confined within the absorption depth. Therefore, by choosing a wavelength with relatively short absorption depth, local surface modification can be achieved without changing the bulk of the material.

The absorption coefficient determines the light absorption as a function of depth. The time needed for the excited states to transfer energy depends on the specific material and the specific mechanisms within the materials. Defects and quantum- confined electronic states can play a significant role in slowing down the thermalization time. If the laser-induced excitation rate is low compared to the thermalization rate, the absorbed laser energy can be considered as being directly transformed into heat. Such processes are called **photothermal** and the response of material can be treated in a solely thermal way. For instance, laser processing of metals or semiconductors with slow laser pulse times (>ns) is typically characterized by photothermal mechanisms. In other cases, the excitation energies can be sufficient to directly break bonds (photo-decomposition). This type of non-thermal material modification is typically referred to as **photochemical** processing. During purely photochemical processing, the temperature of the system remains relatively unchanged, as for instance irradiation of polymers with short wavelength laser light, where the photon energy is on the order of the chemical bond energy. Similarly, ultrafast femtosecond laser pulses can enable photochemical processing of metals and semiconductors [16]. However, even in those cases, it is possible for thermal modifications to occur after the excited states thermalize with lattice phonons [17]. Material responses that exhibit both thermal and non-thermal mechanisms are typically referred to as **photophysical**.

An important factor in those simplified treatments is the **thermal diffusion length** (in the order of microns) which is defined as:

$$l_T \approx \zeta \sqrt{D\tau} \quad [1.1]$$

Where :

$$D = \frac{\kappa}{\rho c_p} \quad [1.2]$$

Is the thermal diffusivity of the material, κ is the thermal conductivity, ρ is the density and c_p is the specific heat capacity.

The prefactor ζ is a geometric constant which depends on the particular geometry of the problem (i.e., bulk versus thin film absorption).

The latter characterizes the distance over which temperature changes propagate in some characteristic time τ. Typically, τ is considered to be the laser beam dwell time or temporal pulse width, in which case we can consider the thermal diffusion length as a measure of how far the energy spreads during the laser irradiation. Following this initial interaction, further thermal propagation leads to elevated temperatures at distances beyond this length. The spread in energy during the pulse is combined with energy spread after the pulse and can lead to changes in the material properties. The region over which these changes occur is defined as the **heat affected zone (HAZ)** (in the order of microns) and exhibits a number of significant differences relative to the bulk material. Given the treatment of laser absorption, the importance of lasers for surface modifications and the ways to control these interactions can be understood. For opaque materials, the optical absorption depth is very small. With short laser times, thermal diffusion length is similarly small. In such a case, all of the optical energy can be considered as absorbed in a thin surface layer of the material with a profile matching that of the beam and without significant thermal diffusion out of this region during the initial interaction. Furthermore, that confinement can be relaxed by increasing the absorption and diffusion lengths through the appropriate choice of laser wavelength and increased dwell time.

The details of the material response will depend on the particular material and the laser processing conditions. As mentioned earlier, in the case of a photothermal process, the material response will be a function of the local material heating and cooling rates, maximum temperatures reached, and temperature gradients. Due to the extreme material heating rates, the changes to the material can be significant. Fluence levels above the melting threshold lead to the formation of molten material pools on the surface. The molten material will support much higher atomic mobilities and solubilities than in the solid phase and can result in rapid material homogenization.

Laser ablation is the removal of material from a substrate which is accomplished by direct absorption of laser energy [18]. This is usually discussed in the context of pulsed lasers, although it is also possible with intense CW irradiation. The onset of ablation occurs above a threshold laser fluence which depends on the absorption mechanism, material properties, microstructure, morphology, presence of defects and on laser parameters. With multiple pulses, the ablation threshold may decrease due to accumulation of defects. Above the ablation threshold, the thickness or volume of material removed per pulse typically shows a logarithmic increase with fluence.

If the fluence of a laser beam incident on a material surface is high enough to surpass the threshold value (F_{th}), which is a characteristic value for each material, material decomposition will occur. According to the **Beer-Lambert law**, the beam intensity will drop exponentially along the propagation path inside the material. Thus, for $F_o \geq F_{th}$ values:

$$F(x) = F_o \bullet e^{-ax} \qquad [1.3]$$

Where :

F_o (W/cm^2) is the initial beam intensity

α (cm^{-1}) is the absorption coefficient

x (cm) is the depth below the material surface.

If the case of intense light, the materials linear response does not hold anymore, giving rise to nonlinear optical processes. The dominant reason is that at high concentrations the molecules interact electrostatically with each other due to close proximity leading to deviations from the linear absorption coefficient.

Materials can be divided in four main categories: metals, ceramics, polymers and composites. Metallic materials are characterized by high reflectivities to laser radiation, thus consideration of laser wavelength must be taken into account such that an efficient laser-material interaction can be obtained. Lasers can be successfully used for the machining and forming of polymeric materials by direct ablation of the material. Lasers are well-suited for the processing of ceramic materials due to very high absorptivity of ceramics to laser radiation. Depending on the type of constituent materials, the composites have widely different processing routes, and lasers are primarily used in the area of machining and forming.

A variety of mechanisms for material removal may be active during laser ablation depending on the particular material and laser processing parameters such as wavelength, fluence, and pulse length [19]. At low fluences, photothermal mechanisms for ablation include material evaporation and sublimation. With higher fluence, heterogeneous nucleation of vapor bubbles leads to normal boiling. If heating is sufficiently rapid for the material to reach its critical temperature, rapid homogenous nucleation and expansion of vapor bubbles lead to explosive boiling (phase explosion) carrying off solid and liquid material fragments [20]. These thermal mechanisms can be understood as thermodynamic phase changes in response to the high temperatures. When the excitation time is shorter, non-thermal, photochemical ablation mechanisms can occur. For instance, with ultrafast pulses, direct ionization and the formation of plasma can lead to athermal phase transformations and direct bond-breaking. In polymers and biological materials which exhibit long thermalization times, photochemical ablation can still occur with short wavelength nanosecond lasers, producing well defined ablated regions with small HAZs [21]. In all cases, material removal is accompanied by a highly directional plume ejected from the irradiated zone. The dense vapor plume may contain solid and liquid clusters of material. At high intensities, a significant fraction of the species may become ionized, producing a plasma. Also, with longer pulses, interaction of the light with the plume may be significant. The volume of material that is directly excited by the laser does not have much time to transfer energy to the surrounding material before being ejected. Therefore, the ablated volume becomes more precisely defined by the laser's spatial profile and optical penetration depth, and the remaining material has less residual energy, which reduces the HAZ [22]. During ns ablation, shielding of the surface by the ejected ablation plume can reduce the energy absorbed by the material. Material responses often involve a combination of ablation, surface melting, and thermally activated processes which can lead to cumulative changes in the material.

1.4 Laser Processing – Direct and Indirect methods for photonic applications

By choosing the appropriate laser parameters, precise control of the final material properties can be achieved. By using a laser, rapid heating of the surface can be achieved with little thermal penetration. The heating and quench rates, and thus resulting material properties, can be precisely controlled by adjusting laser parameters such as pulse length (or scan speed for CW lasers) and fluence [23]. **Laser cleaning** utilizes intense laser radiation to remove contaminants from a solid surface in a controllable manner while leaving the underlying substrate largely unaffected. The technique exploits differences in the optical and thermal properties of the underlying substrate and the contaminant layer. **Laser micromachining** is one of the most widely used techniques for direct micro-structuring. Excimer laser sources emitting in the ultraviolet (UV) provide many advantages and are widely used for a variety of materials processing applications, due to the fact that they result in superior quality at relatively low-energy density levels, stems from the short absorption depth and the minimal thermal effects. The etching properties of a wide range of solid materials have been studied for the development of optical microstructures [24]. In addition, vacuum ultraviolet (VUV) laser photons have shown several advantages in comparison to longer wavelengths because of the confinement of the photochemical changes [25, 26, 27].

Surface processing of hybrid materials is very important in the struggle for novel microstructures for photonic applications. Numerous fabrication methods have been reported and in many cases conventional lithography cannot be applied, due to the mechanical and chemical sensitivity of the materials. Direct laser etching thus becomes a preferred fabrication method, enabling the fabrication of simple grating structures [28] or even more complex features on a material surface by controlled ablation [29, 30, 31]. In addition, excimer laser can also be used for the modification of thin films at ambient temperature where, among other things, it results in the change of the film from hydrophilic to hydrophobic [32].

1.4 References

1. http://cordis.europa.eu/technology-platforms/photonics_en.html

2. Kaminow I., Li T. and Willner A.E., “Optical Fiber Telecommunications”, Elsevier(2013)

3. Prasad P.N., “Introduction to Biophotonics”, John Wiley& Sons (2004)

4. Petersen J.K., “Handbook of Surveillance Technologies”, CRC Press(2012)

5. Adamovsky G., Baumbick R. J. and Tabib-Azar M., Proc. SPIE 3330, 200(1998)

6. Hariharan, P., “Basics of Interferometry”, Elsevier (2007)

7. Toal V., "Introduction to Holography", CRC Press(2012) –8. Kelsall R., Hamley I. and Geoghegan M., “Nanoscale Science and Technology”, Wiley, 2005

9. Campbell P., J. Opt. Soc. Am. B 10 (12), 2410(1993)

10. Zhang S.Y., Ren Y.H., Lupke G., Appl. Opt. 42 (4), 715(2003)

11. Romero L.A., F.M. Dickey, J. Opt. Soc. Am. A: 13(4), 751(1996)

12. Momma C., Nolte S., Kamlage G., Von Alvensleben F., Tunnermann A., Appl. Phys. A Mater. Sci. Process. 67, 517(1998)

13. Sanner N., Huot N., Audouard E., Larat C., Huignard J.P., Loiseaux B., Opt. Lett. 30 (12), 1479(2005)

14. Nemoto K., Nayuki T., Fujii T., Goto N., Kanai Y., Appl. Opt. 36(30), 7689(1997)

15. Heinemann S., Opt. Commun. 119, 613 (1995)

16. Chichkov B.N., Momma C., Nolte S., Von Alvensleben F., Tunnermann A., Appl. Phys. A Mater. Sci. Process. 63 (2), 109(1996)

17. Hirayama Y., Obara M., Appl. Surf. Sci. 197, 741(2002)

18. Eason R.W., “Pulsed Laser Deposition of thin films: applications-led growth of functional materials”, John Wiley & Sons(2007)

19. Chrisey D.B., Hubler G.K., “Pulsed Laser Deposition of Thin Films”, Wiley-Interscience, New York(1994)

20. Bulgakova N.M., Bulgakov A.V., Appl. Phys. A Mater. Sci. Process. 73(2), 199(2001)

21. Garrison B.J., Srinivasan R., J. Appl. Phys. 57(8), 2909(1985)

22. Liu X., Du D., Mourou G., IEEE J. Quantum Electron. 33(10), 1706(1997)

23. Hick A.J., Heat Treat. Met. 10(1), 3(1983)

24. Vainos N. A., Mailis S., Pissadakis S., Boutsikaris L., Parmiter P. J. M., Dainty P. and Hall T. J., Appl. Optics 35, 6304(1996)

25. Truica-Marasescu F., Pham S. and Wertheimer M. R., Nucl. Instrum. Methods Phys. Res 265, 31(2007)

26. Cefalas A C Appl. Surf. Sci. 247 577(2005)

27. Douvas A. M., Petrou P. S., Kakabakos S. E., Misiakos K., Argitis P., Sarantopoulou E., Kollia Z. and Cefalas A. C., Anal. Bioanal. Chem. 381, 1027(2005)

28. Vasileiadis M., Athanasekos L., Meristoudi A., Alexandropoulos D., Mousdis G., Karoutsos V., Botsialas A. and Vainos N. A., Opt. Lett. 35 1476(2010)

29. Neiss E., Flury M., Gerard P., Mager L., Rehspringer J. L., Fort A., Montgomery P., Fontaine J., Engel T. and Benatmane A., Appl. Sur. Sc. 254, (1986)

30. Mailis S., Zergioti I., Koundourakis G., Ikiades A., Patentalaki A., Papakonstantinou P., Vainos N. A. and Fotakis C., Appl. Optics 38, 2301(1999)

31. Winfield R. J., Meister M., Crean G. M. and Paineau S., Mat. Sc. in Sem. Proc. 3, 481(2000)

32. Takeda S., Ikuta Y., Hirano M. and Hosono H., J. Mater. Res. 16, 1003(2001)

2. Investigation of Direct Laser microfabrication for special polymeric and hybrid photonic structures

2.1 Introduction

Microfabrication is a strategic field in microelectronics, optoelectronics and microsystems technologies. The development of this sector has led to revolution of information technologies and todays information era [1]. Microfabrication is also widely used in all specialized fields, including sensors [2], microreactors [3], combinatorial arrays [4], microelectromechanical systems (MEMS) [5], microanalytical systems [6], micro-optical systems [7, 8] and more. Here, the use of microfabrication techniques is studied for the development of optical elements mainly for sensing applications.

2.2 193 and 157 nm excimer laser processing of TMOS-$NiCl_2$ sol-gel material

Ablative ultraviolet laser surface processing is a generic single-step approach that can be applied successfully to composite materials. Applications involve micro/nanostructure formation for use in hybrid photonic and optoelectronic devices and other applications. Thus, in this work, sol-gel tetramethyl orthosilicate (TMOS) derived composite thin films comprising embedded $NiCl_2$ nanoparticles, were illuminated and processed by 193 nm and 157 nm excimer laser radiation. The effect of different laser fluences of 193 nm and the number of pulses of 157 nm on the material surface was studied. AFM imaging was used to evaluate the effects of the irradiation.

The material used in this work was synthesized by use of tetramethyl orthosilicate (TMOS) mixed with deionized water, HCl 0.1 M, and isopropanol. The $NiCl_2$ nanoparticles were *in situ* synthesized with addition of stoichiometric equivalents of $NiCl_2 \cdot 6H_2O$, and 5% w/v solution was obtained. The mixture was left stirring for 2 days and then was aged for two weeks. The final thin films were obtained with a spin coating technique. AFM and SEM analyses revealed a good dispersion of $NiCl_2$ nanoparticles with a smooth overall film surface [9].

Two separate laser processing experimental workstations were used. The experimental setup with the 157 nm molecular fluorine laser (Lambda Physik, LPF 200) consists of a 316 stainless steel vacuum chamber equipped with a computer-controlled X-Y-Z-θ translation stage, where the TMOS-$NiCl_2$ samples were placed, as well as the focusing optics. The laser beam delivered 25 mJ per pulse with a 15 ns FWHM and were focused with a high purity CaF_2 lens down to 100μm.

In the 193 nm processing case, an excimer laser micro-processing workstation based on an ArF excimer nanosecond laser source is used. The system is equipped with special optics and an XYZ nanopositioning system. It operates in an automated way via computer control and special software and allows real time monitoring of the ablation process via a CCD camera system. Laser fluence is controlled by a variable attenuator and monitored by a calibrated pyroelectric power meter. A first observation of etched areas showed that sol-gel is a quite controllable material suitable for high quality direct laser etching.

2.2.1 Unexposed area

AFM measurements were carried out to reveal the morphology of the surface. Figure 2-1a shows the AFM image of the non-exposed TMOS-$NiCl_2$ nanocomposite and its cross-section along one scanned line, shown in Figure 2-1b. The Z-scale of the image is ~ 55 nm and the imaging area is 2 × 2 μm. The AFM image reveals structures 150 nm wide. We note here that the nanomaterials are prepared by in situ synthesis, which continuous even after spin coating. For this reason the particle distribution is not known in advance. From previous experimental work performed in ultrathin films, AFM measurements showed a good dispersion of nanoparticles with sizes of 30-220 nm [10]. Furthermore, the salt material is in its complex form which depends on the atmospheric environment especially via the exchange of hydroxyl or water groups. For the thicker thin films such as used in the present work, a direct estimate of nanoparticle size distribution cannot be made reliably due to packing issues but a rough estimate of the mean size of the order of 50-100 nm may be deduced.

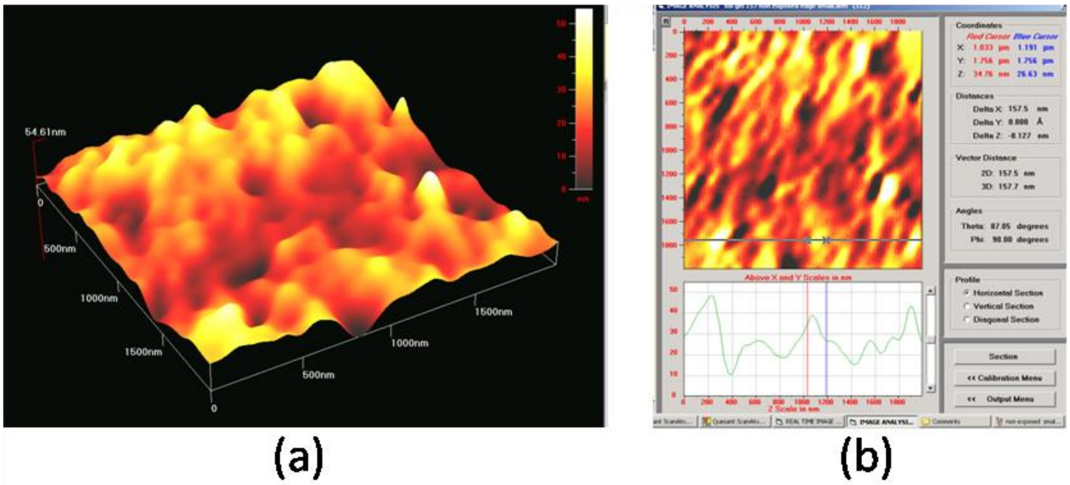

Coordinates
Red Cursor Blue Cursor
X: 1.033 μm 1.191 μm
Y: 1.756 μm 1.756 μm
Z: 34.76 nm 26.63 nm

Distances
Delta X: 157.5 nm
Delta Y: 0.000 Å
Delta Z: -8.127 nm

Vector Distance
2D: 157.5 nm
3D: 157.7 nm

Angles
Theta: 87.05 degrees
Phi: 90.00 degrees

Profile
● Horizontal Section
○ Vertical Section
○ Diagonal Section

(a) (b)

Figure 2-1: (a) AFM image of the non exposed-area of TMOS-$NiCl_2$ (2μm x 2μm). (b) 2D AFM image of the non-exposed area of TMOS-$NiCl_2$ (2μm x 2μm). The cross-section along one scanned line reveals structures 150 nm wide.

For the non-irradiated sample the pitch is irregularly distributed in the x direction and is between 0.3-1.5 μm (Figure 2-2a). In addition craters appear on the top of all the hill-like structures.The typical surface roughness (z-direction) of the non-exposed film is 30 nm (Figure 2-2b)

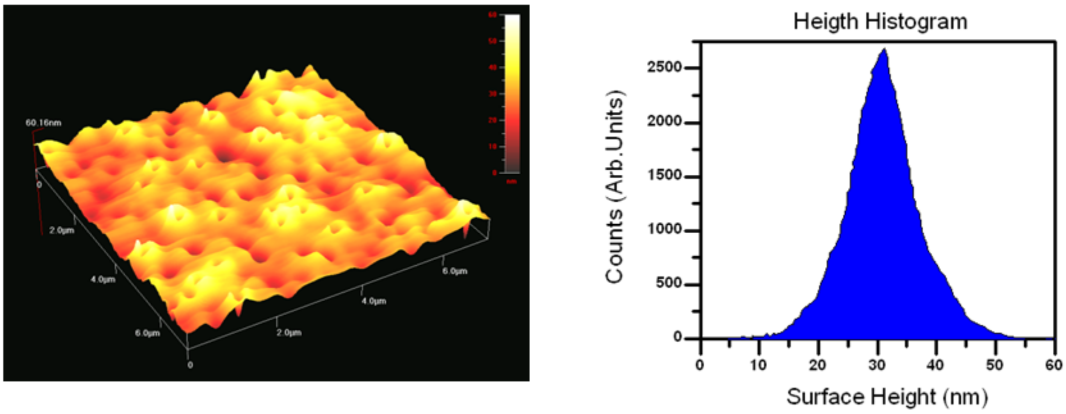

(a) (b)

Figure 2-2: (a) AFM image of non-exposed area of TMOS-$NiCl_2$ sample. (b) Surface roughness histogram (z-direction) of non-exposed areas. The distribution is relatively symmetric with a maximum at 30 nm.

2.2.2 Processing with an F_2 excimer laser (157 nm)

Surface morphology imaging of films, both prior and after exposure at 193 and 157 nm was performed with an AFM (Innova Veeco). The AFM images are obtained using the intermittent contact mode at ambient conditions with a silicon cantilever. High-resolution images of the film surfaces are obtained at different scanning areas at the maximum scanning rate of 0.5 Hz and with 600×600 pixel image resolution. Following irradiation with one laser pulse, the difference of surface morphology and roughness is clearly demonstrated in the AFM image of the edge between exposed and non-exposed areas (30µm x 30µm) (figure 2-3).

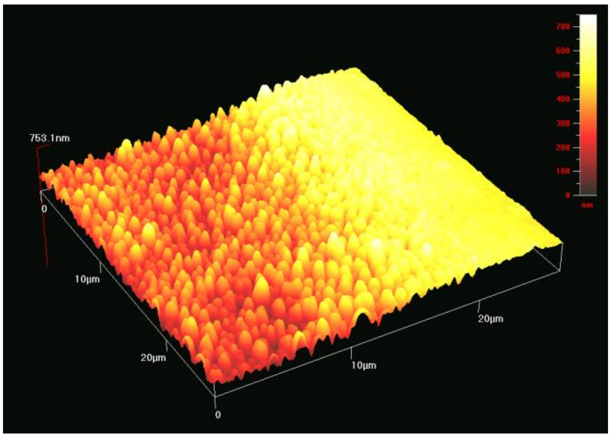

Figure 2-3: AFM image of the edge between exposed and non-exposed areas following 157 nm irradiation. The rms surface roughness of the non-exposed area is ~30 nm and the exposed area ~250 nm.

The edge is well defined thus suggesting photochemical dissociation of the exposed areas. The edge height difference between the two areas is ~ 400 nm at 1.2 J/cm^2 per laser pulse (figure 2-4).

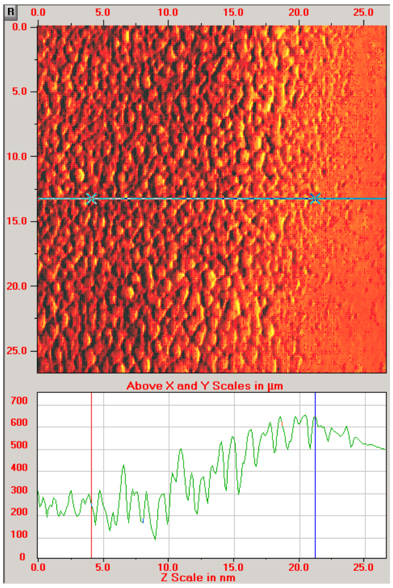

Figure 2-4: 2D AFM image of radiated/unirradiated areas of TMOS-NiCl$_2$ sample. The step height of the boundary (edge) is ~ 400 nm is produced by one laser pulse at 1.2 J/cm^2 energy density.

Following 157 nm irradiation, the surface increases its roughness (figure 2-5), giving granular and elongated structures with typical average height values around 240 nm at 1.2 J/cm^2 per pulse (figure 2-6).

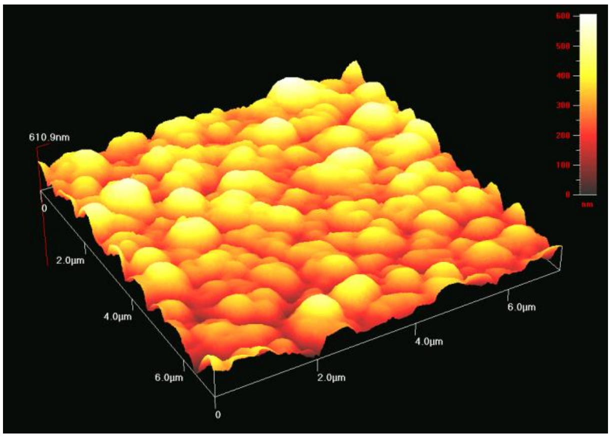

Figure 2-5: AFM image of the TMOS-NiCl$_2$ sample following 157 nm exposure with one pulse at 1.2 J/cm^2. The surface roughness is increased giving granular and elongated structures.

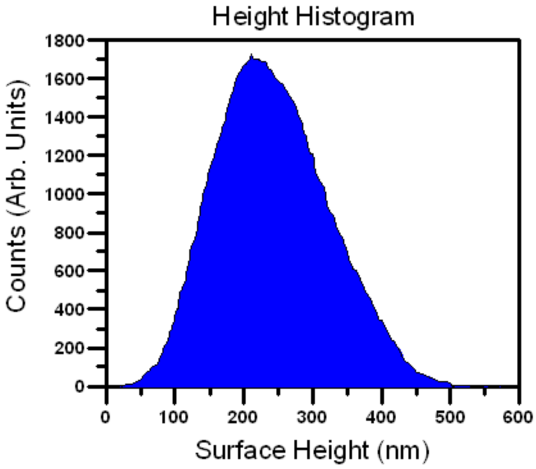

Figure 2-6: Height distribution histogram of the observed structures for an area 7 µm × 7 µm following 157 nm exposure with one pulse at 1.2 J/cm^2.

The etching depth at 157 nm, as measured with a profilometer, is shown in figure 2-7 and indicates the presence of two different linear regions, may be suggesting the presence of competing processes.

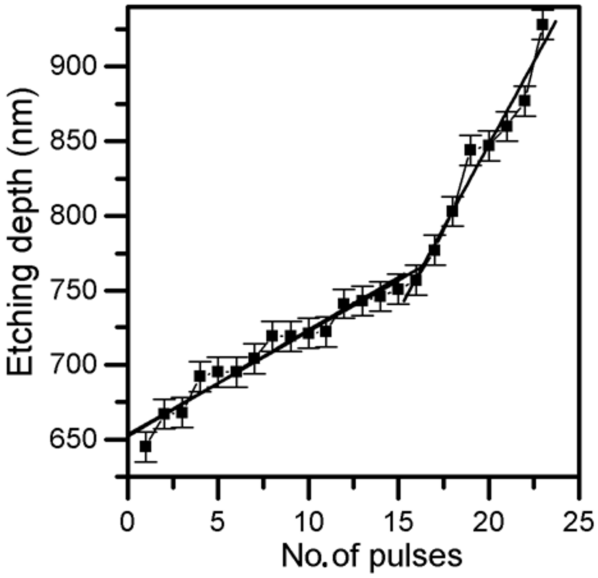

Figure 2-7: The etching depth as a function of no of laser pulses at 157 nm, measured with a profilometer. The laser fluence is 1.2 J/cm^2 per pulse.

The etching rate (nm/pulse) as a function of laser pulses is given in figure 2-8. The etching rate decreases exponentially. Obviously this is due to surface glassification and carbonization of the matrix element (figures 2-5, 2-6).

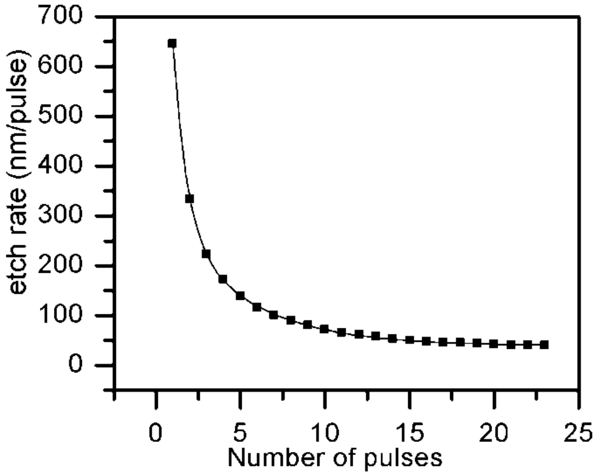

Figure 2-8: The etching rate (nm/pulse) as a function of laser pulses at 157 nm decreases exponentially. The laser fluence is 1.2 J/cm^2 per pulse.

Following irradiation at 157 nm, the surface of the film appears to show a self–assembled structured in comparison to the rather irregular image of the non-exposed film. The average size of the self-assembled structures (pitch) along the x axis is decreasing with increasing number of pulses (laser exposure). The typical pitch size along the x-direction is decreasing from ~ 720 nm (Figure 2-9) to 520 nm for 20 focused laser pulses (1.2 J/cm^2 per laser pulse). The surface roughness is increased to 240 nm (Figure 2-6) and 450 nm following irradiation with one and five laser pulses respectively. Repeating analysis with 20 laser pulses showed that the roughness is decreasing to 320 nm. Taking into consideration that at 157 nm one photon breaks one chemical bond, most of the organic photofragments are ejected away from the substrate with supersonic speed [11]. During irradiation material is constantly removed, but at the same time the remaining composites are clustered together to form new structures due to the strong electrostatic forces from the high accumulation of electrons on the metal particles. The association of the pitch size with the laser fluence is rather difficult to determine, due to the fact that the surface morphology depends not only to the illumination parameters, but also on the type of material, film thickness and heat dissipation from the substrate.

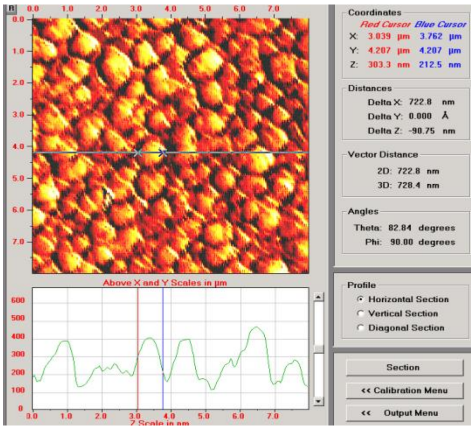

Coordinates

	Red Cursor	Blue Cursor
X:	3.039 µm	3.762 µm
Y:	4.207 µm	4.207 µm
Z:	303.3 nm	212.5 nm

Distances

Delta X: 722.8 nm
Delta Y: 0.000 Å
Delta Z: -90.75 nm

Vector Distance

2D: 722.8 nm
3D: 728.4 nm

Angles

Theta: 82.84 degrees
Phi: 90.00 degrees

Profile

● Horizontal Section
○ Vertical Section
○ Diagonal Section

Figure 2-9: 2D AFM image of the TMOS-NiCl$_2$ sample following 157 nm exposure with one laser pulse at 1.2J/cm^2 per pulse. The typical pitch size along the x direction is ~ 720 nm.

2.2.3 Processing with an ArF excimer laser (193 nm)

A series of typical ablated craters is shown in figure 2-10a. Even more sophisticated structures can be fabricated on TMOS-NiCl$_2$, such as diffraction gratings, as shown in figure 2-10b. Despite the fact that there is some evidence of scattering issues, the treated areas may prove suitable for optical applications. Previous works of the group have successfully demonstrated such structures fabricated on the TMOS-NiCl$_2$ material for sensing applications [12]. In addition, processing of PMMA thin films at 157 nm increased the detection sensitivity of methanol, ethanol and water vapours by 400% [13].

The profile of the craters is of almost rectangular shape, with minimal redeposition of material as shown in figure 2-10c.

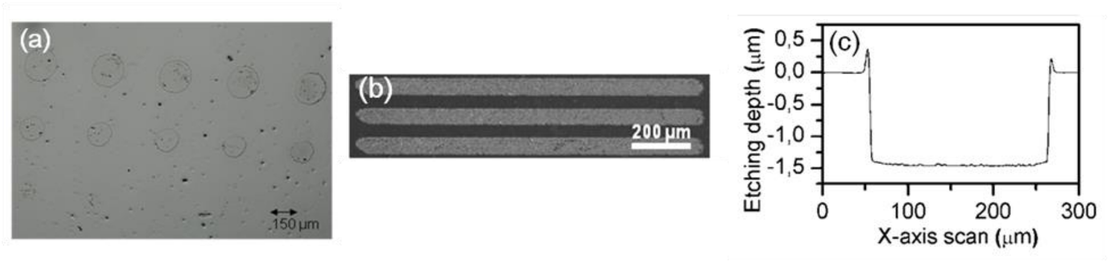

Figure 2-10: (a) Typical optical microscope image of ablated TMOS-$NiCl_2$ sol-gel material after 193 nm laser irradiation at various fluence values. (b) TMOS-$NiCl_2$ grating structure by direct laser etching for sensing applications. (c) Typical hole profile of TMOS-$NiCl_2$ material created by one pulse of 193 nm laser at 25 mJ/cm^2 fluence (Tencor Alpha-Step 500IQ).

Figure 2-11 represents the dependence of the ablation depth on the laser fluence on the material for single laser pulse irradiation. The comparatively moderate fluences have a high impact on the ablation depth of the material owing to the higher penetration of the 193 nm radiation, thus suggesting that 193 nm source is a very useful tool for TMOS-$NiCl_2$ processing.

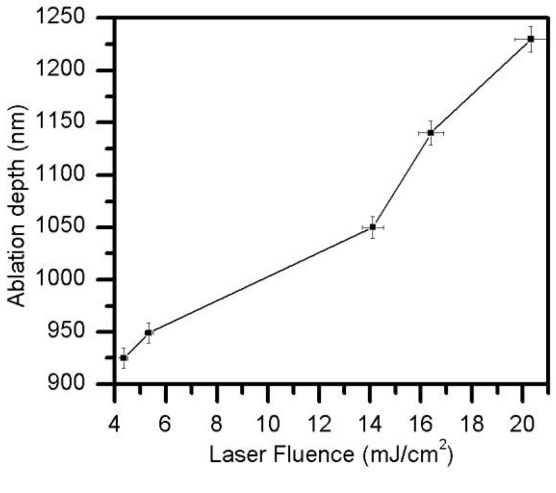

Figure 2-11: Single pulse etching upon 193 nm illumination as a function of laser fluence for TMOS-$NiCl_2$. Error bars are set to ±3% for laser fluence and ±1% for ablation depth.

The AFM image of the edge between irradiated and non-irradiated areas with one laser pulse at 4.3 mJ/cm^2 fluence is shown in figure 2-12.

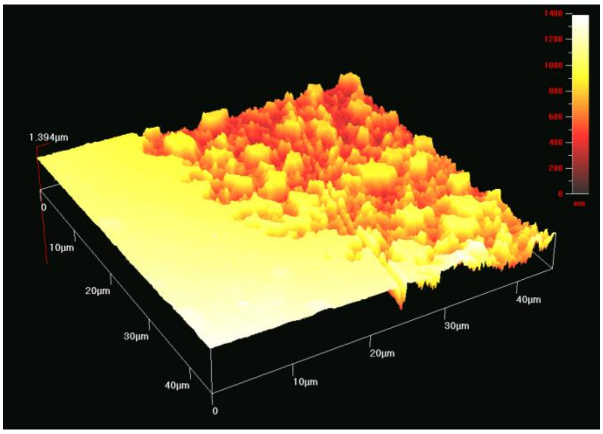

Figure 2-12: AFM image of the edge between single laser pulse irradiated area at 4.3 mJ/cm^2 fluence, and non-irradiated areas, using 193 nm laser irradiation.

The roughness of the irradiated areas (figure 2-13) is increased as compared to that of non-irradiated areas, shown in figure 2-2a. The AFM analysis (7μm x 7 μm) indicates the presence of volcano crater shapes.

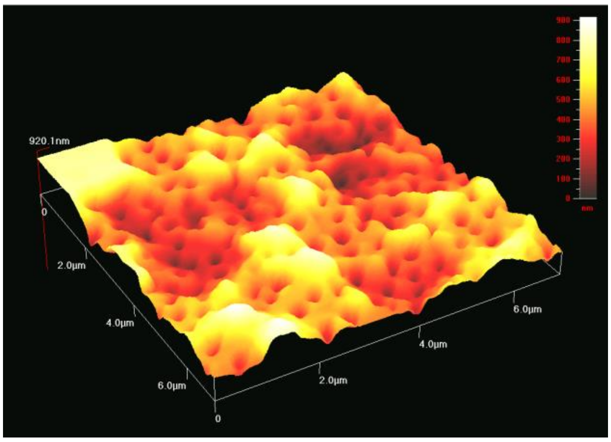

Figure 2-13: Surface morphology of the irradiated areas with the 193 nm laser source.

The surface roughness is greatly altered and it consists of areas with different size distribution. The broader one peaks at 500 nm, and the narrower at 770 nm, as presented in the AFM scan of figure 2-14. Although the presence of an area at 770 nm can be attributed to the fact that the irradiation with 193nm laser beam causes the photo-dissociation of bonds and the formation of new ones, the fact that the area appears narrow indicates a possible systematic error thus the area is an artifact.

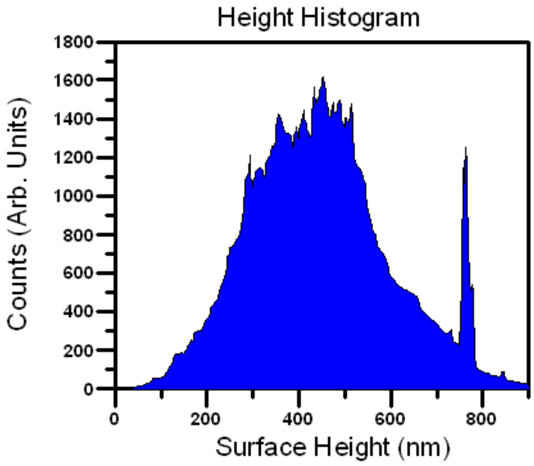

Figure 2-14: Size distribution after irradiation with the 193 nm excimer laser

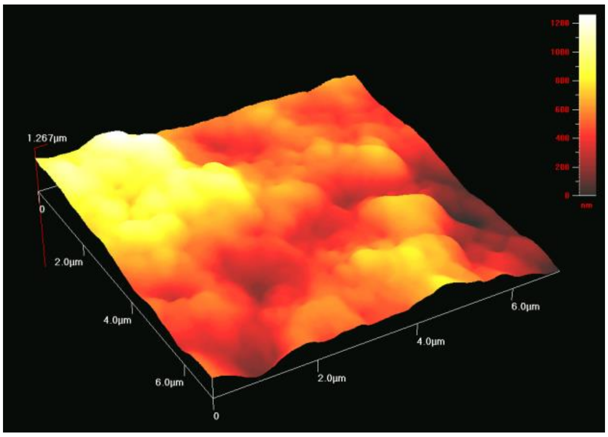

Figure 2-15: Surface morphology of the irradiated areas with 193 nm laser source at 20 mJ/cm^2.

Figure 2-15 depicts a result of higher irradiation fluence. The crater-like shapes seem to disappear in this case. However, the roughness (average height), the rms roughness (rms deviation) and the particulate distribution appear to be increasing and depend significantly on the uniformity of the laser beam and the local nature of the target material.

2.2.4 Comparative Aspects

The numerous advantages of UV-VUV excimer lasers over infrared (IR) or visible lasers are drawn from the higher absorptivity of most materials in the UV region. Laser energy is almost perfectly coupled into the material resulting in high quality processing with minimal or completely absent thermal effects in the processed area and this justifies the preference in thin film processing and surface modification. In addition, the shorter wavelength of UV lasers as compared to IR and visible ones allows high optical resolution leading to high precision. Moreover, due to the short pulse duration there is not enough time for the energy to diffuse into adjacent areas and thus heat the non-exposed material. This results in high precision features, whereas in the IR regime the thermal impact is relatively larger.

By focusing on the edges between irradiated and non-irradiated areas for the two cases, AFM analysis revealed that 157 nm laser radiation causes surface photochemical dissociation of the exposed areas and thus results in well-defined edges, whereas the 193 nm radiation induces deeper ablation effects in the exposed areas, causing sloped edges and larger inhomogeneity. In addition, the morphology of irradiated areas with 157 nm and 193 nm is highly dissimilar. The 157 nm irradiation results in the increase of surface roughness. The surface morphology of the material is also significantly altered upon illumination with the 193 nm source. The AFM results reveal the presence of volcano crater shapes. The surface roughness is greatly altered and it consists of areas with different size distribution. The volcanic craters do not appear at 157 nm, suggesting that besides surface ablation, additional processes are taking place after the interaction of radiation with matter.

The photochemistry in the VUV region (157 nm) is different from 193 nm and other UV wavelengths [14, 15, 16]. For most of the organic materials, the density of dissociative excited electronic states around 7.8 eV (157 nm) is high therefore the absorption of one photon by the organic molecule at 157 nm implies complete bond breaking. The parent molecule breaks up into small fragments, atomic, diatomic or triatomic species ejected away from the substrate with supersonic speed [11]. The dissociation processes from the excited electronic states populated by the absorption of laser photons in the UV region (248 nm and 193 nm) coexist with relaxation processes that convert part of the photon energy to thermal energy [17, 18]. Consequently different dissociation pathways occur at this wavelength region due to simultaneous photochemical and thermal effects. In both cases there is no evidence of differential ablation in the nanocomposite constituents. This is corroborated by the highly energetic nature of the photons and the dissociative ablation resulting in multicomponent ejection. It should be mentioned, though, that 157 nm VUV excimer lasers are more difficult to use due to the requirement of vacuum and the special and more expensive optics needed.

TMOS-$NiCl_2$ sol-gel thin films were irradiated with 157 nm and 193 nm excimer lasers. The impact of 193 nm laser fluence and 157 nm number of pulses was studied, by monitoring the surface before and after laser exposure aiming to understand the influence of UV irradiation on the film structure and surface morphology, and optimize the processing of composite materials.

Modification of surface roughness of the organic films is expected to enhance the adsorption of various detectable chemical agents. In parallel the chemical modification of the surface at 157 nm enhances the target-probe binding strength and thus the detection sensitivity in sensing applications.

Optimization of the excimer laser radiation process will result in the improvement of the quality and resolution of the fabricated features towards obtaining nanoscale level processing, thus opening new horizons in the fabrication of nanostructures in several application fields.

2.3 193 nm laser processing of Polydimethylsiloxane (PDMS)

Surface modification of PDMS material is a very important factor in the quest for novel microstructures for photonic applications [19]. While in many cases conventional lithography techniques cannot be applied, due to the softness of the material, new techniques have to be applied. Direct laser etching is a modification method that can be applied in most cases where accuracy is the keystone of the process.

Polydimethylsiloxane (PDMS) films that were spin coated on silica substrates were illuminated by UV excimer laser. An ArF laser at 193 nm was used at several numbers of pulses while keeping all other illumination conditions steady. AFM imaging was used to evaluate the effects of the irradiation process and it was found that surface morphology was modified in a controllable way. Physical and chemical properties strongly depend on the illumination conditions. Applications involve micro/nanostructure patterning by direct laser etching for use in photonic and optoelectronic devices.

The PDMS samples (Dow Corning Sylgard 184) were prepared by mixing the base and the curing agent in the ratio 10:1 by mass weight. The mixture was poured in a glass bottle and then degassed under low vacuum (10^{-2} mbar) for 30 min. films were then formed from the degassed PDMS by spin-coating (WS-400BX Laurell Technologies, North Wales, PA), at 5000 revolutions per minute (rpm). The spin coating was performed for 30 sec, with an acceleration of 85 rpm/sec until the required speed is reached. The substrates were microscope slides. Following spin coating, curing is allowed at ambient conditions (23^0C) for more than 7 days in order to retain the full mechanical and electrical properties. The thickness of the PDMS film measured using a Tencor Alpha Step profile meter was 10.86 μm. After curing, the samples were placed in the irradiation chamber.

The experimental set-up used is shown in figure 2-16. The laser is an ArF UV laser emitting at 193 nm. The micropositioning stage movement was PC controlled via a Labview program. The laser beam spot size was 0.059 mm^2 and the laser fluence was found to be 810 mJ/cm^2. The repetition rate of pulses was kept at 1 sec.

The number of pulses was gradually increasing and monitoring of the etching process was performed.

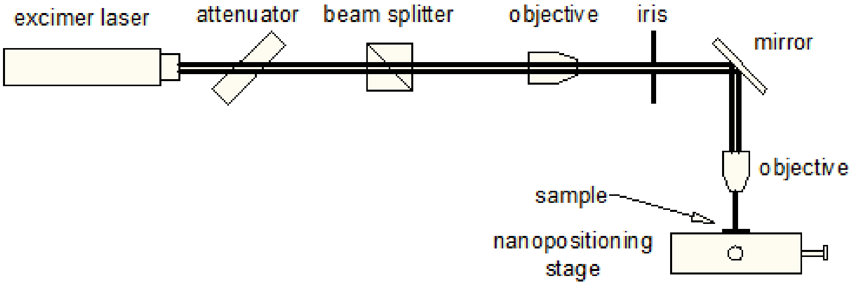

Fig.2-16: Experimental set-up used for PDMS illumination

Some typical results of holes created by laser light illumination of PDMS are shown in figure 2-17.

Figure 2-17: Typical optical microscope image of ablated PDMS material

In more detail, in figure 2-18a the laser-material interaction is apparent, inducing deformations in the surface, while the non-illuminated area is smooth. In figure 2-18b, a typical spot is shown, while in figure 2-18c a close-up of a spot reveals an interesting phenomenon where the laser power is not highly focused on the center of the spot and thus the left area is not so granulated as compared to the center and right areas. An alternative scenario would suppose that the film is not perpendicular to the beam normal, but it is rather tilted. A series of spots is shown in figure 2-18d. while at the bottom there are visible single spots that stem from a single pulse of moderate power, in the center of the image, there are overlapping spots, mainly due to fact that the high power of the laser resulted in wide craters. It should be noted here that the dark spot on the right is just a mark for observation facilitation and has been done by applying multiple pulses on the same region. In figure 2-18e, a close-up of an overlapping spot is shown. A second spot (spot in a apot) is clearly visible which is explained as the result of a previous pulse. Finally, in figure 2-18f, a series on spots clearly separated from each other is shown. Again, on the bottom right position, there is a dark mark for defining the film topology.

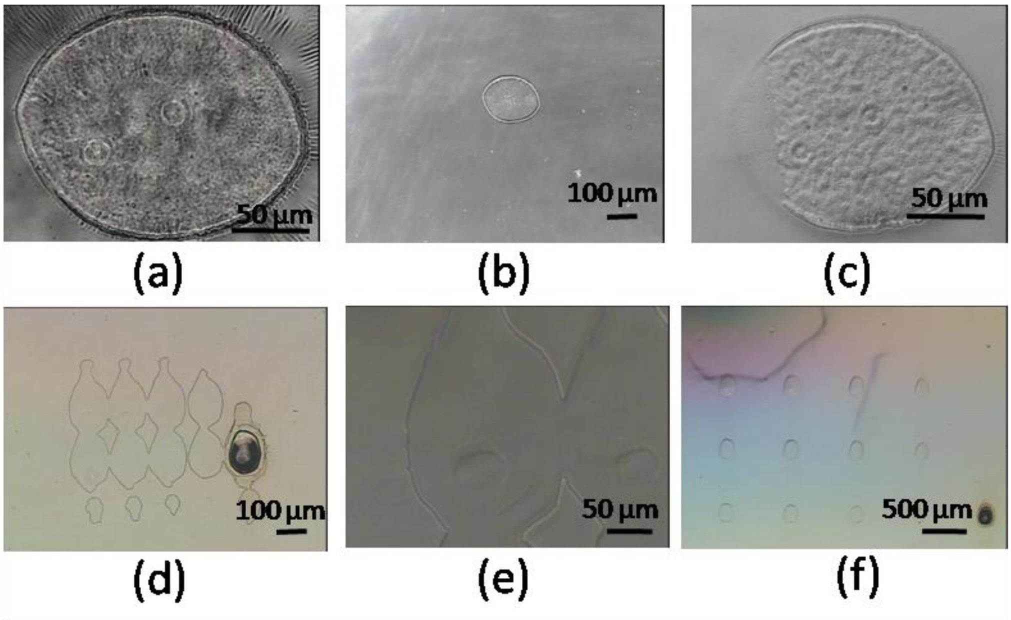

Figure 2-18: (a) – (f) Typical spots on PDMS resulting from 193nm illumination (optical microscope images)

PDMS material is rather soft, resulting in a crater-like profile of holes upon laser illumination, as shown in figure 2-19a. In addition, by applying multiple pulses on the same region, the effect of each pulse (for a given pulse energy) on the ablation depth could be measured, as shown in figure 2-19b.

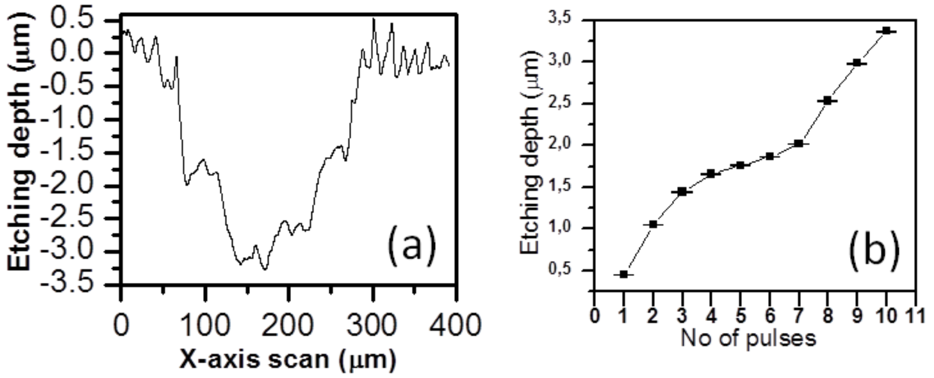

Figure 2-19: (a) Surface profile of a typical PDMS crater upon 193 nm illumination. (b) Ablation depth v. No of pulses in PDMS material (193 nm illumination)

In order to characterize the result of 193nm illumination on PDMS, a thorough AFM study was performed, with morphology measurements before and after exposure at 193 nm. Thus, in figure 2-20, an AFM image (2-20a) of the non-exposed areas of the PDMS sample is shown, whereas in 2-20b the surface roughness histogram (z-direction) is found to be almost symmetric around the maximum surface roughness value (134 nm).

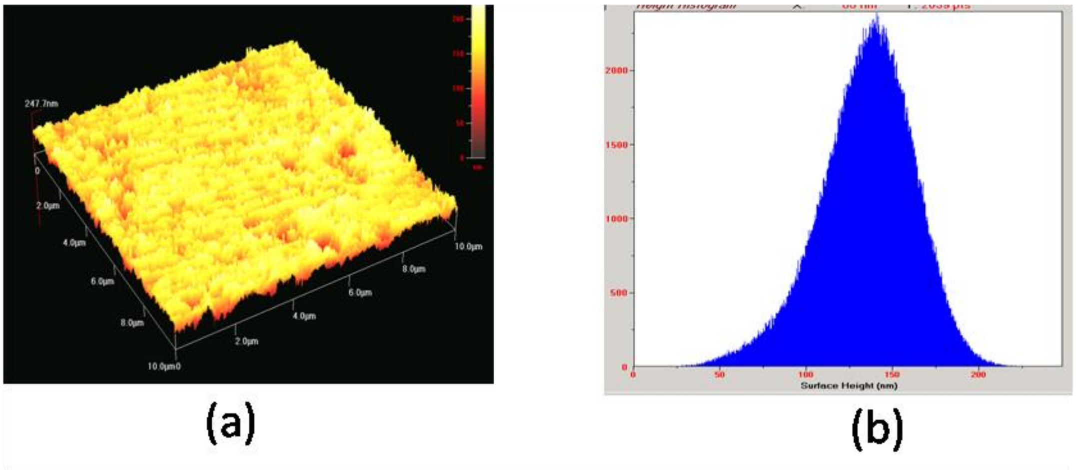

Figure 2-20 :(a) AFM image and roughness distribution histogram of the non-exposed areas of the PDMS sample (10 μm × 10 μm scanned area). (b) The surface roughness histogram (z-direction) is symmetric around the maximum surface roughness (134 nm).

On applying laser illumination on the PDMS surface, the latter changes dramatically, as shown in figure 2-21.

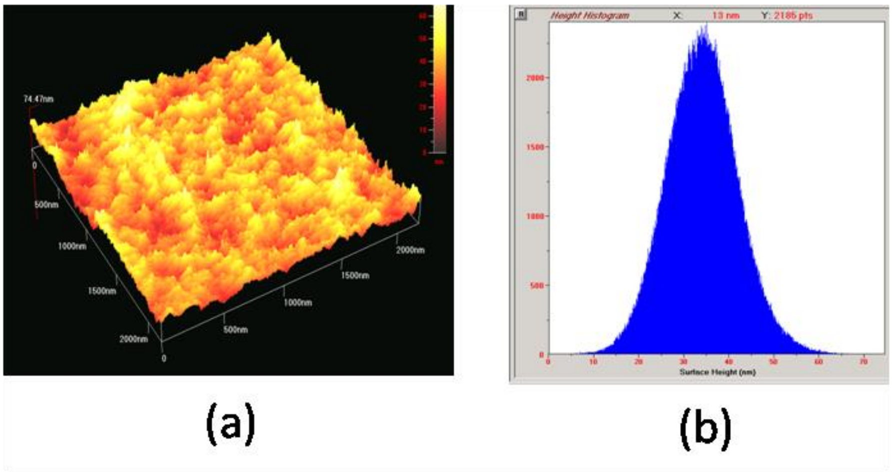

(a) (b)

Figure 2-21: (a) AFM image and (b) roughness distribution histogram of PDMS sample (2 μm × 2 μm scanned area) exposed with 193 nm radiation. The maximum surface roughness is now at 35 nm.

The morphology alterations at the edge between exposed and unexposed regions of the material are shown in AFM images of figure 2-22.

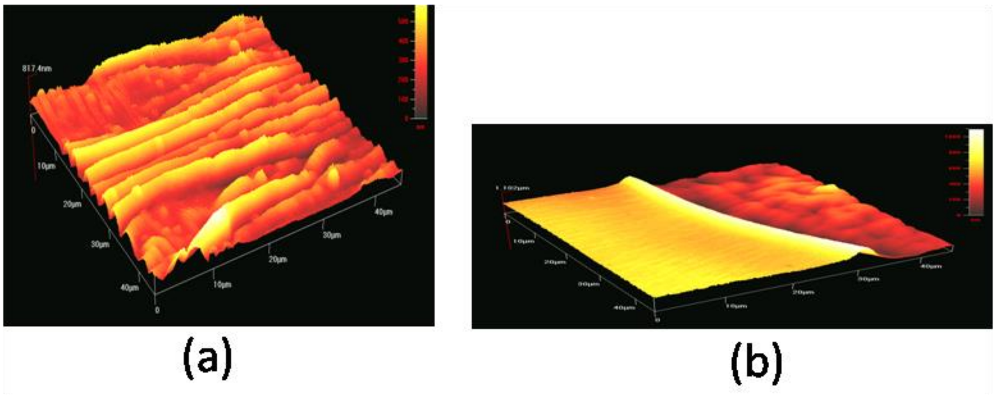

(a) (b)

Figure 2-22: (a) AFM image morphology of the edge between exposed and non-exposed area of a PDMS sample. (b) non-exposed area close to the edge

Moreover, on applying different number of pulses on the material, interesting results were obtained, as shown in figure 2-23.

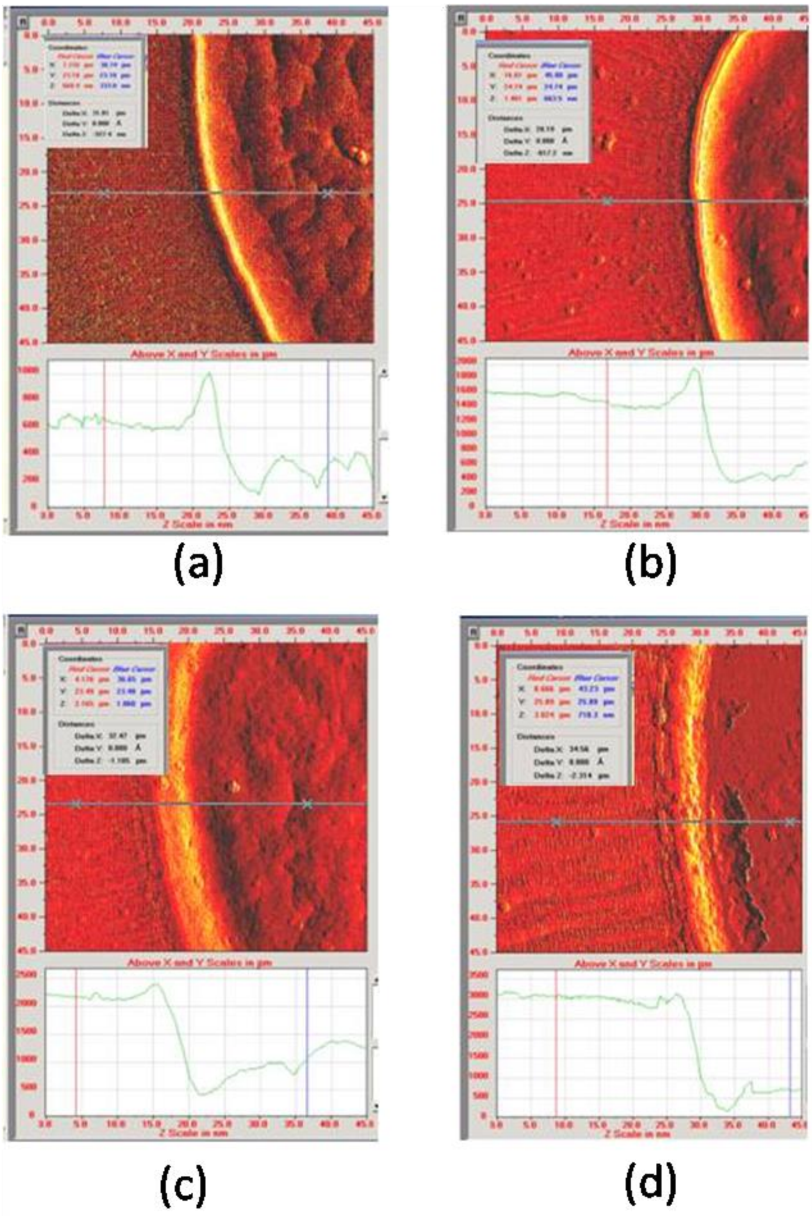

(a) (b)

(c) (d)

Figure 2-23: 2D AFM images of unirradiated/radiated areas of PDMS for different numbers of pulses. The step height of the boundary (edge) was 327 nm for (a) 1 pulse (b) 817 nm for 4 pulses (c) 1µm for 6 pulses and (d) 2.3µm for 9 pulses with 50 mJ/cm^2 energy per pulse.

PDMS films were illuminated with 193 nm excimer laser with increasing number of pulses. Samples were studied before and after exposure using 193 nm laser light to understand the influence of UV irradiation on the film's chemical structure and surface morphology. The irradiation caused photo-dissociation of bonds. The chemical changes were accompanied by surface morphology modification.

2.4 Other polymer and hybrid materials

Extending the study of the effect that excimer laser illumination has on soft materials, a comparative study was performed between Polyisoprene- poly(acrylic acid) (IAA-3:Au 4:1) and hybrid inorganic-organic material, TEOS-MAA-PEG :Au 2:1. Thin films of both materials were illuminated with 193 nm laser pulses. The resulting graph for the ablation depth as a function of laser fluence in the case of pure polymer is shown in figure 2-24a. It was noticed that at the region of about 400 nm, the curve does not continue its almost linear shape, but reaches a plateau, instead. This can be attributed to possible resolidification phenomena. In addition, the resulting graph for the hybrid material is shown in figure 2-24b.

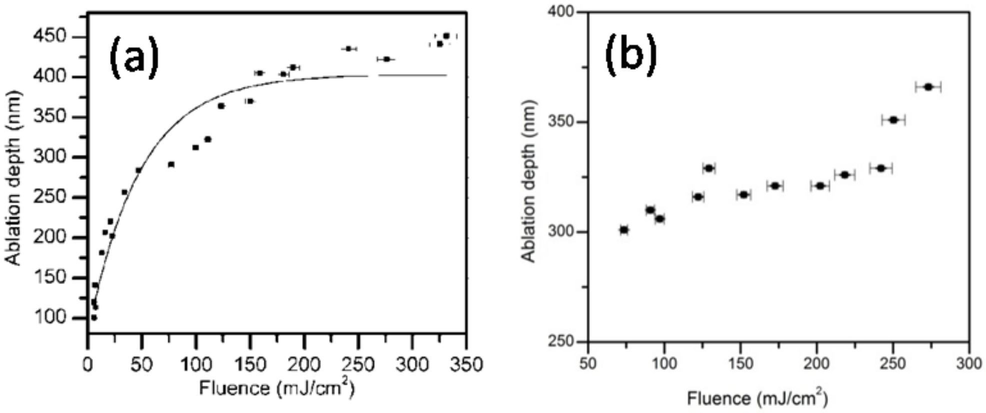

Figure 2-24: Ablation depth v. laser fluence for (a) PI-PAA material and (b) TEOS-MAA-PEG :Au

As can be deduced from the above graphs, IAA-3 material being softer, reacts in a different way as compared to the hybrid TEOS-MAA-PEG upon laser illumination.

2.5 Laser microprocessing on Polymer Optical Fibers (POFs) for photonic sensor applications

Polymer Optical Fibers (POF) have been proposed as a promising sensor platform [20, 21, 22] due to the combination of a wide sensing capability with low complexity and cost, which offer the attractive possibility for their effective integration in several current and challenging applications. On the other hand, tailoring the optical interfaces of sensing materials by means of structures leads to enhanced functional responses. It effectively allows the efficient interaction of materials with the environment in addition to advanced means for sensor interrogation, an important aspect for engineering functional devices [23, 24, 25, 26].

In this context, a key issue here relates to the availability of fabrication methods suitable to process mechanically and chemically sensitive materials. Different types of lasers, from continuous wave (cw) to pulsed excimer and ultrashort femtosecond pulses at various wavelengths, from the ultraviolet (UV) to infrared (IR), have been deployed for surface modification and structuring in various materials [27, 28, 29]. The ArF excimer laser source operating at λ=193nm, becomes a prime tool for microprocessing materials and fabricating diffractive optical elements (DOEs) [30], modification of polymer materials [31] or silica fibers [32]. Indeed, earlier works that demonstrated the potential of polymer processing using 193 nm UV laser radiation have considered it as the ideal tool [33] and the use in structuring POFs with high controllably thus becomes favorable as compared to conventional (e.g. mechanical knife) etching techniques.

In this work the effect of deep ultraviolet laser illumination on POFs is studied, having as an ultimate goal the fabrication of photonic sensing devices. The fabrication results are evaluated in the frame of potential photonic sensor case studies addressing ammonia and humidity detection.

2.5.1 Experimental procedures

The experimental laser-based microfabrication station is presented in figure 2-25. It comprises an ArF excimer laser source operating at 193 nm, and a prototype optical system for laser beam delivery system. It is capable of direct processing at the micron and submicron regime, depending on the nature of the material. An X-Y-Z nanopositioning stage allowing 80nm absolute positioning accuracy is employed to hold the sample under processing. The microfabrication system is fully computer-controlled via custom software. A CCD camera is also attached to the system for real time monitoring of the microfabrication process.

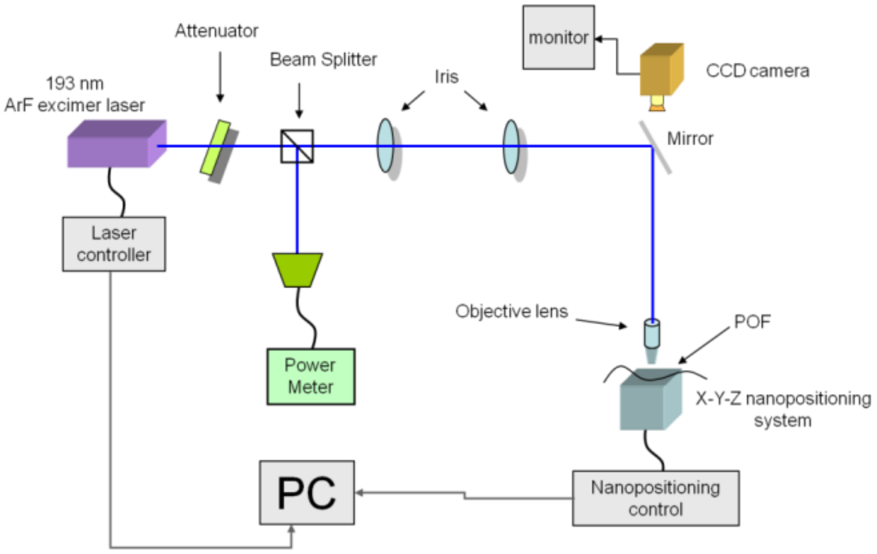

Figure 2-25: Experimental setup which includes an ArF excimer laser, an X-Y-Z PC-driven nanopositioning stage, a power meter and a series of optics for the direction of the beam onto the POF.

A schematic representation of the microcavities can be found in figure 2-26.

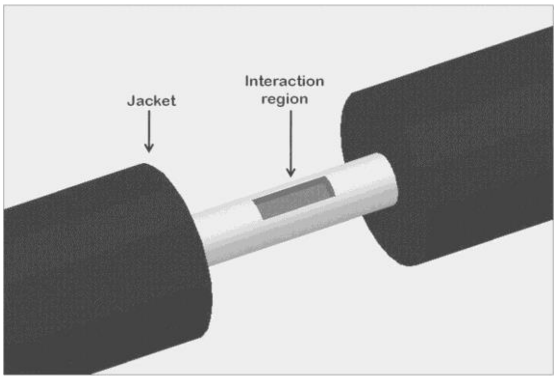

Figure 2-26: Schematic of the microcavities created on the POF surface

A system for on-line monitoring of transmission loss during fiber microstructuring has been configured using suitable laser beam coupling optics and a Newport 2832-C Dual Channel power meter, as shown in figure 2-25.

In this work the processing of Polymer Optical Fiber-POF ESKA GH-4001P, Mitsubishi-Rayon Co., having a 1 mm total diameter and 980 μm core diameter is performed. The fiber core material is poly(methylmethacrylate) (PMMA) having refractive index n_{core}=1.49 at λ= 650 nm, and the cladding material is its fluorinated variant having n_{clad}=1.46 at λ= 650 nm. The absorption coefficient of the POF materials at λ=193 nm is expected to be α (193) =2000 cm^{-1} [34].

Several POF samples of exactly the same length were prepared and used for processing. The laser pulse fluence was adjusted between 3 J/cm^2 and 20 J/cm^2 by using a computer-controlled variable optical attenuation system and laser pulse repetition rate was set at 10 Hz to minimize possible heat accumulation. A real time image of the micromachining process can be found in figure 2-27.

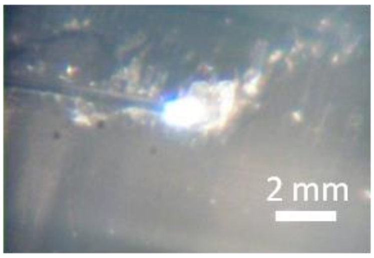

Figure 2-27: Photo of the ablation process taken by moving the fiber. The ablation plasma and the crater left behind are apparent.

Figure 2-28 presents typical etched structures which have as expected a conical form. An experimental protocol has been designed and applied by taking into account laser etching properties of the fiber materials and structure geometry. The depth of the structure was set as the significant variable which was changed systematically by multiple step-and-repeat irradiation by the focused laser beam.

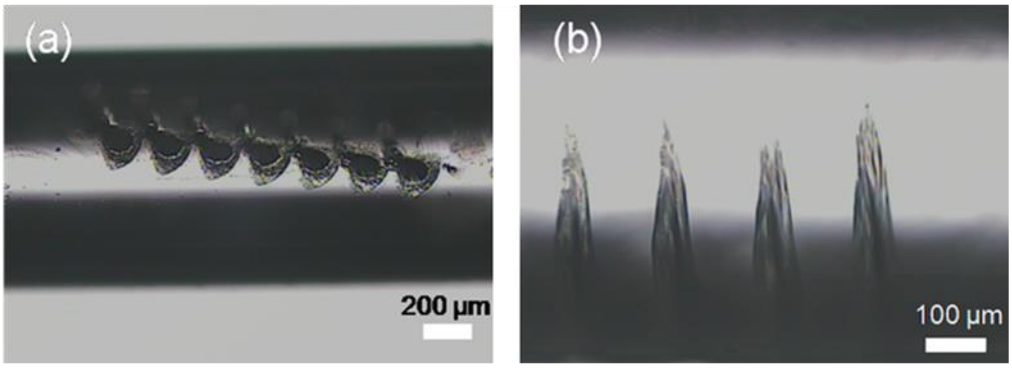

Figure 2-28: Optical microscope images of (a) top view of etched structures and (b) side view of etched structures imaged through the POF cylinder surface.

On each sample, a different degree of loss was induced by direct laser etching, starting from the cladding towards the core center. The dimensions of the etched structure were measured by using an optical microscope. The ablated volume was calculated and it was subsequently used as the main parameter for studying the induced propagation loss and assessing structured fiber performance.

Figure 2-29(a) presents the variation of measured etch depth as a function of laser fluence at λ=193nm. The differences between clad and core material are not considered at this point and the result represents the overall effect. The observed ablation threshold fluence values were found to be F_{th}(clad)=121 ± 5 mJ/cm^2 for the cladding and F_{th}(core)= 101± 5 mJ/cm^2 for the core and are consistent with earlier works [35]. The different threshold value of 80 mJ/cm^2 found for pure PMMA may be attributed to the difference of the material used [36]. A linear trend from outer surface to about 400 μm etch depth is observed while etching saturation occurs above the 500μm etching depth and accumulative fluence above 40 J/cm^2, range in which the limited depth of focus of the system also starts affecting the operation. As the laser beam penetrates through the cladding and into the core region, the high order modes first become radiating and propagation loss increases. Scattering becomes more profound as the structures approach the center of the core, leading gradually to great loss and practically to inhibition of propagation. Figure 2-29(b) presents the observed behavior as a function of total ablated volume. A 3dB loss point is found at about 5×10^{-4} cm^3 volume which represents a regime for useful operation.

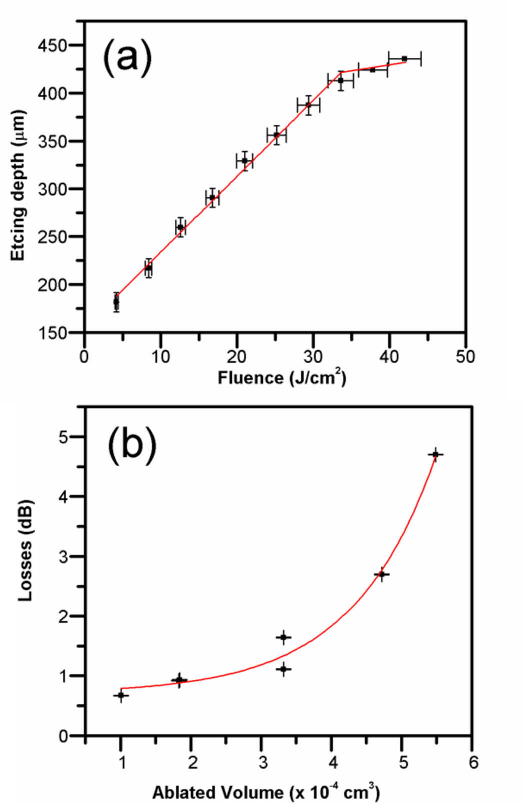

Figure 2-29: Experimental plots of (a) the effect of the cumulative laser fluence on the etching depth of POF and (b) the measured propagation loss as a function of the total ablated POF volume.

To further investigate the effect, the propagation loss during the etching operation was monitored in real time. Figure 2-30 presents the induced losses as a function of etch depth. Two linear regions having different slopes are observed. A first region, measured from the surface to about 10 μm depth shows a Power Loss/unit etch depth = $(0.015 \pm 3 \cdot 10^{-3})$ dB/μm while for the deeper regime from about 10 μm to 50 μm a value Power Loss/unit etch depth =$(0.007 \pm 3 \cdot 10^{-4})$dB/μm was found.

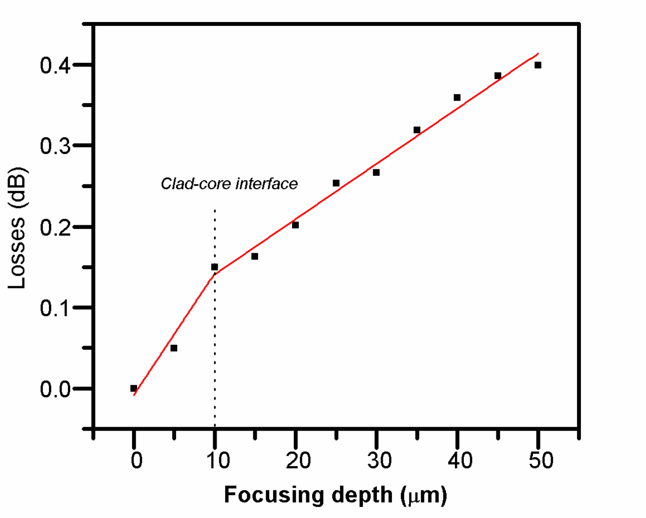

Figure 2-30: Experimental real-time monitored dependence of propagation power losses as a function of the depth of etched structures.

Various shapes of grooves and holes were etched in POF samples using different ablation parameters including pulse repetition rate and laser fluence in order to evaluate the operation. Figures 2-31a and 2-31b depict Scanning Electron Micrographs (SEM) obtained using a ZEISS EVO MA 10 microscope, of a groove created along the fiber axis. Figures 2-31c and 2-31d present the creation of holes in the fiber surface. Visible debris is attributed to recasting or resolidification phenomena following material ablation.

Once, under high fluence conditions, an ultraviolet photon is absorbed by the polymer chain, photochemical processes take place [37]. The ablation products and the products of these photochemical reactions are related to the type of polymer and irradiation wavelength. Poly (methyl methacrylate) (PMMA) which is the fiber core material, upon UV illumination depolymerizes, forming the monomer.

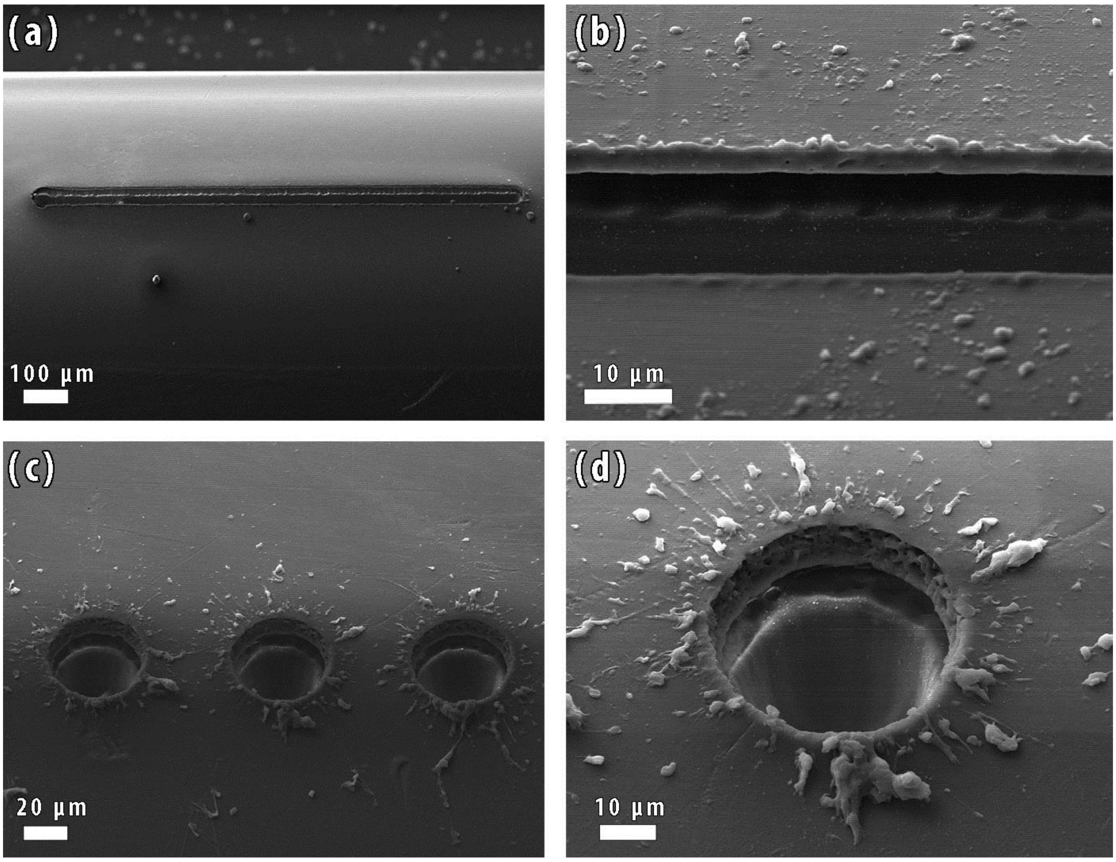

Figure 2-31 : (a) Panoramic image of a groove created along the fiber. (b) Close up of a groove. Some residues is visible. (c) Holes created upon laser illumination and (d) close up of an ablated hole.

As can be seen in figure 2-32, upon performing laser ablation on the POF surface, the different layers are clearly separated, namely the cladding region and the core region. The latter is attributed to the different absorption characteristics that the two regions exhibit.

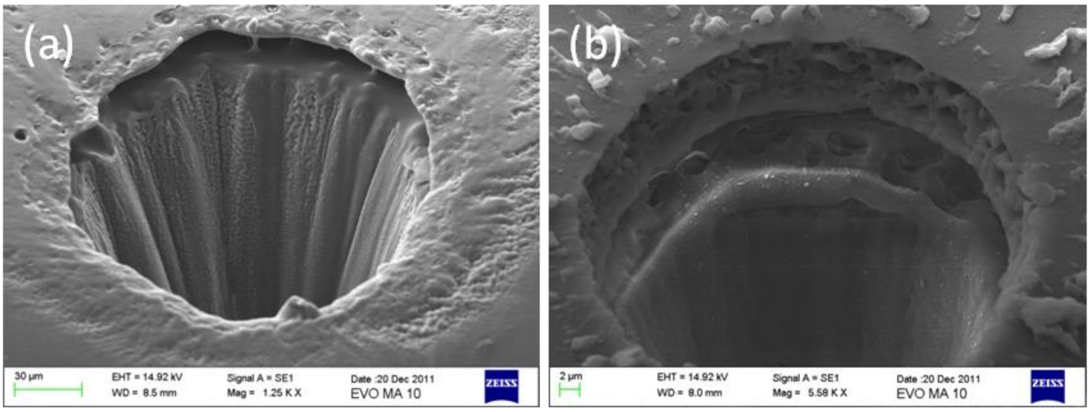

Figure 2-32: SEM images of two holes created on the POF surface. The (a) absence or (b) presence of remnants depends on laser fluence values.

Figures 2-33a and 2-33b, also show a represantative result of the effect of changing the laser fluence, by which it is possible to control the quality of the created structure.

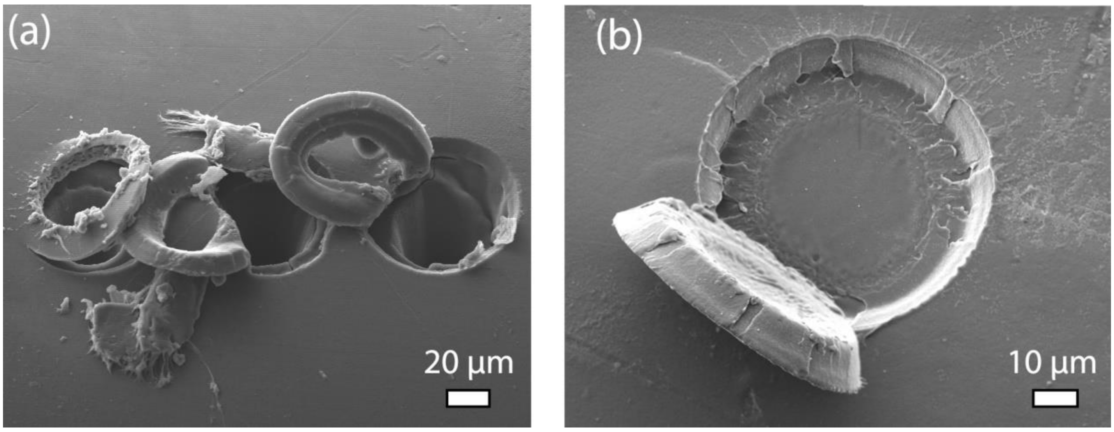

Figure 2-33: (a) Series of ablated holes where the cladding is clearly detached . (b) Close up of an ablated hole. The diameter is about 70 μm.

Further interesting observations considering figures 2-33a and 2-33b can be discussed here. At the first stage of the experiments, a low number of pulses (1-10 pulses) at 10 Hz repetition rate at laser energy (2.9 ± 0.5) μJ and respective fluence 93 mJ/cm^2 was incident on the sample but no etching effect was visible. The onset of etching is thus not sharply defined in the case of fluorinated polymer, i.e. the cladding material. It can thus be deduced that the fraction of incident energy that is absorbed in the volume in order to break the bonds and precede etching, is relatively high. This can be attributed to incubation effects and is related to the modification of the material by the first laser pulses which often results in an increase of the absorption at the irradiation wavelength. While ablation of PMMA with excimer laser does not involve incubation phenomena [38, 39], in the case of the cladding material (fluorinated polymer), incubation may appear. Incubation is often present in polymers that show weak absorption at the irradiated wavelength.

By gradually increasing the number of pulses (10-100 pulses with a 10 pulse step) while keeping all other characteristics unaltered, i.e. repetition rate and laser power, a threshold was reached where the top region of the POF is detached/ separated from the rest of the sample. In figure 2-34, the succession of created holes for increasing number of pulses reveals the threshold which appears for about 50-60 pulses. SEM images revealed that the cladding material does not hold strong affinity with the core material (pure PMMA) upon laser illumination. Ablation of organic polymers by a laser pulse is a volume explosion that is caused by a rise in pressure and temperature within the mass of the material that undergoes ablation. The ejected material forms a blast wave which in turn forces the fluorinated polymer to be detached.

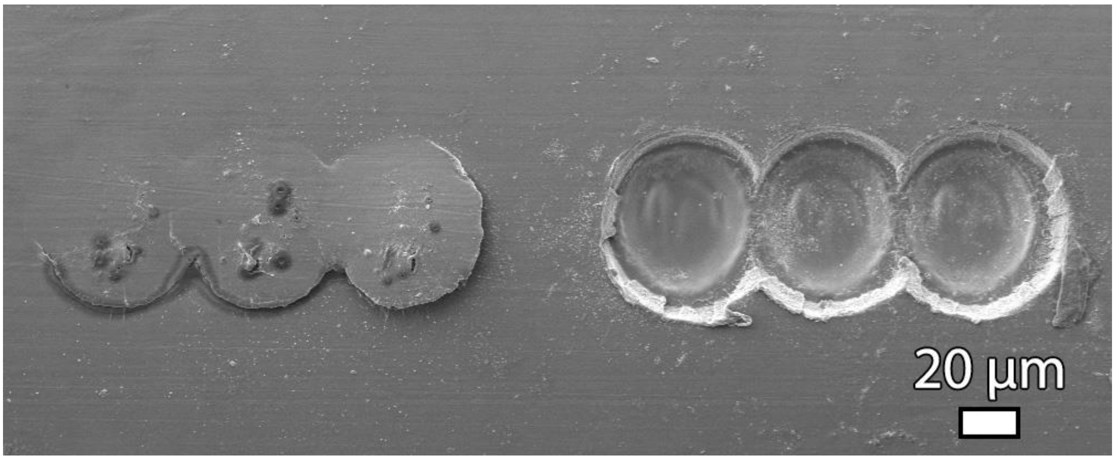

Figure 2-34: SEM image showing the threshold where cladding is separated from the core.

The interesting results of figure 2-34 can be further explained as follows: Fluorinated polymers are thermally more stable due to the fact that the C-O-F binding energy is one of the highest [40]. Moreover, the size and electrical charge of the fluorine atoms compared with the hydrogen ones are higher, and so the molecular mobility is confined and the electrostatic interactions between adjacent atom groups is increased, resulting in a rigid molecular structure. Thus, both phenomena contribute to a higher glass transition temperature. Therefore, fluorinated PMMA (cladding material) is more temperature-resistant and less soluble than non-fluorinated PMMA (core material). In fluorinated polymer, all the hydrogen have been replaced with fluorine atoms. The greater mass of the fluorine atom leads to minimal diffusion phenomena.

The effect of laser illumination on the POF surface was further studied by creating a series of lines along the fiber. Upon light coupling on POF, an impressive output appeared, as shown in figure 2-35. The condition for Total Internal Reflection (T.I.R.) of laser light in the fiber core does not hold anymore, thus light escapes.

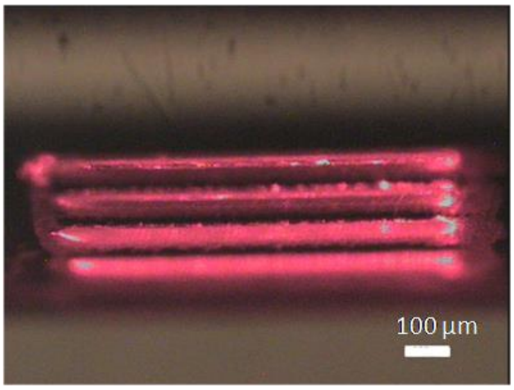

Figure 2-35: Optical microscope image of light escaping from fiber core, creating an impressive output

Moreover, a series of holes with gradually increasing fluence is shown below in figure 2-36a, outlining the importance of laser intensity on micromachining processes. In figure 2-36b, two spots on POF surface are shown that have been created with pulses of different intensity.

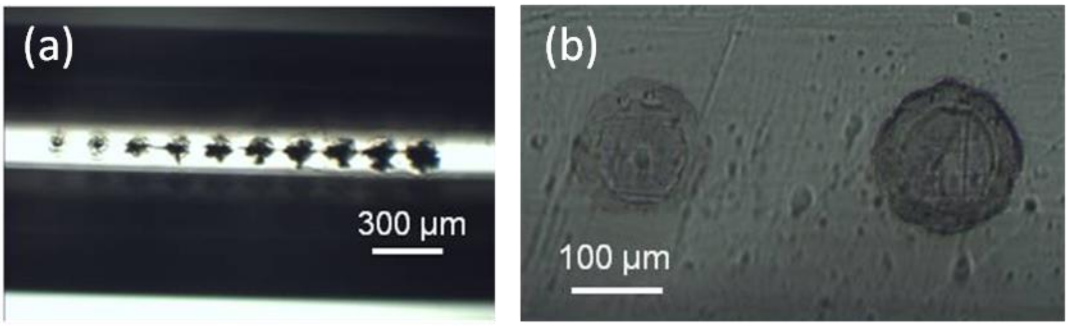

Figure 2-36: (a) A series of holes on POF surface created with gradually increasing fluence. The differences are apparent. (b) Two spots on POF surface, as a result of lower (left) and higher (right) laser fluence.

Moreover, a series of holes were created on a section of the fiber, as shown in figure 2-37.

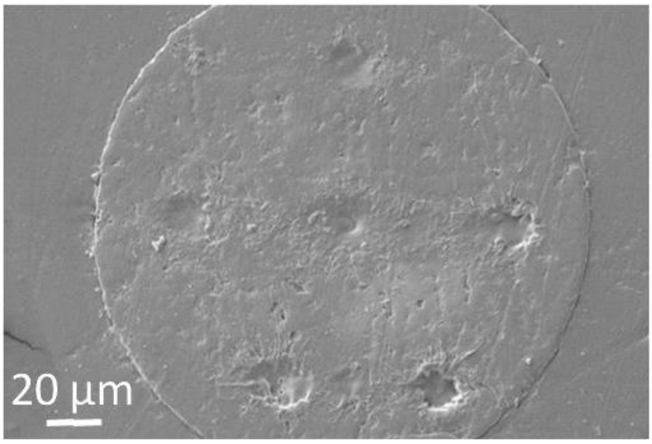

Figure 2-37: Spots created on a section of a fiber.

In order to minimize residue on the POF surface after illumination with the excimer laser, Tetrahydrofuran (THF) was chosen, as a good solvent for PMMA. As shown in figure 2-38, after THF treatment, the PMMA melts, leaving a bad quality surface. Thus, THF solution had to be further diluted and then used for a shorter period of time.

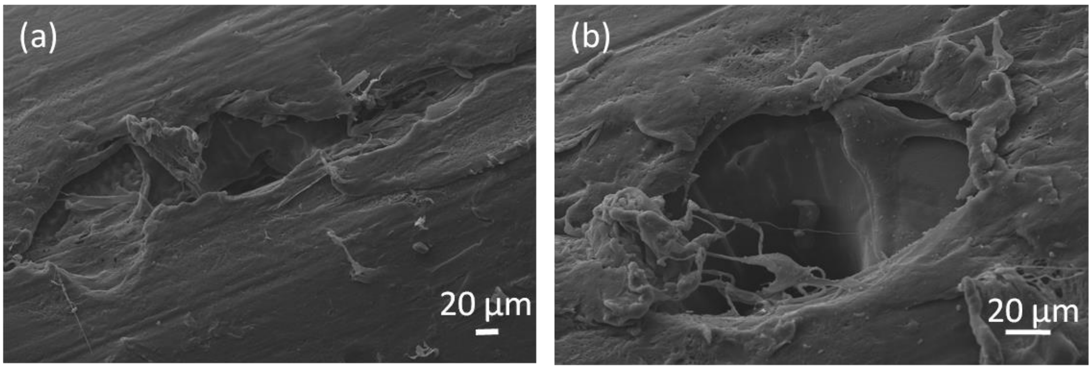

Figure 2-38: (a) The result of THF treatment on POF surface (PMMA). (b) Zoomed-in SEM image of a hole after THF treatment

A zoomed-out SEM image of a processed POF surface is shown in figure 2-39.

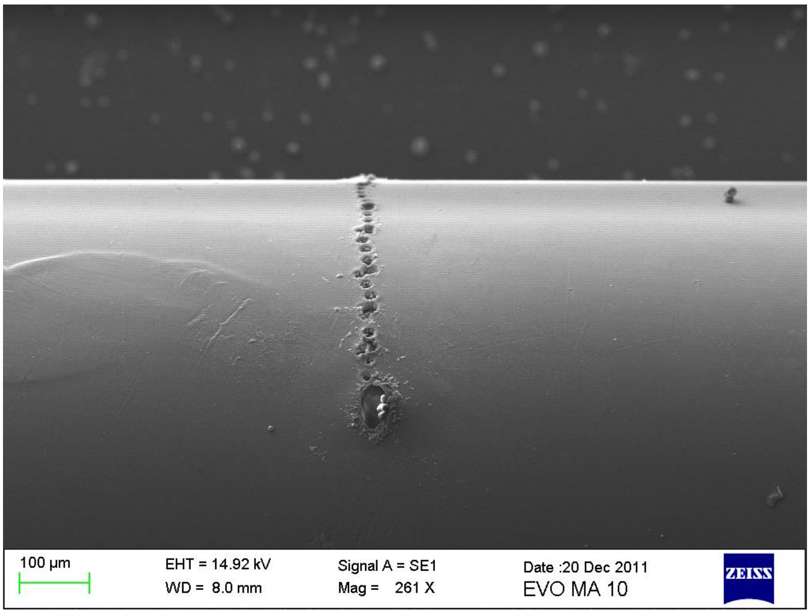

Figure 2-39: Panoramic SEM image of POF surface after creating a series of holes perpendicular to the fiber.

The SEM image of figure 2-39 reveals the relative sizes of the POF surface and the diameter of the holes created with the excimer laser.

2.6 References

1. Barrett C.R., Mater. Res. Soc. Bull. XVIII, No.7:3–10(1993)

2. Bryzek J., Sensors 4, 38(1996)

3. Clark R.A., Hieptas P.B., Ewing A.G., Anal. Chem. 69, 259(1997)

4. Briceno G., Chang H.Y., Sun X.D., Schultz P.G., Xiang X.D., Science 270, 273(1995)

5. Bryzek J., Peterson K., McCulleyW.,IEEE Spectrum 31, 20(1994)

6. Manz A., Chimia 59,140(1996)

7. Wu M.C., Lin L.Y., Lee S.S., King C.R., Laser Focus World 68(1996)

8. Herzig H.P., “Micro-Optics: Elements, Systems and Applications”, London: Taylor & Francis(1997)

9. Vasileiadis M., Athanasekos L., Meristoudi A., Alexandropoulos D., Mousdis G., Karoutsos V., Botsialas A. and Vainos N. A., Opt. Lett. 35, 1476(2010)

10. Tsigara A., Madamopoulos N., Hands M., Athanasekos L., Meristoudi A., Mousdis G., Manasis G., Koutselas I. and Vainos N. A., Proc. of SPIE 6377 63770B-1(2006)

11. Cefalas A. C., Appl. Surf. Sci. 247, 577(2005)

12. Mailis S., Zergioti I., Koundourakis G., Ikiades A., Patentalaki A., Papakonstantinou P., Vainos N. A. and Fotakis C. Appl. Optics 38, 2301(1999)

13. Sarantopoulou E., Kovac J., Kollia Z., Raptis I., Kobe S. and Cefalas A. C., Surf. Inter. Anal. 40, 400(2008)

14. Cefalas A. C., Vassilopoulos N., Sarantopoulou E., Kollia Z. and Skordoulis C., Appl. Phys. A 70, 21(2000)

15. Takao H., Okoshi M. and Inoue N., Appl. Physics A 79, 1571(2004)

16. Ihlemann J., Schulz-Ruhtenberg M. and Fricke-Begemann T., J. of Physics Conf. series 59, 206(2007)

17. Feng Y., Liu Z. Q. and Yi X. S., Appl Sur. Science 156, 177(2000)

18. Castex M. C., Bityurin N., Olivero C., Muraviov S., Bronnikova N. and Riedel D., Appl. Sur. Science 168, 175(2000)

19. Deepak K. L., Rao S., Venugopal R. and Narayana D., Pramana-Journal of Physics 75, 6, 1221(2010)

20. Riziotis C., Pruneri V., Smith P. G. R. and Vasilakos A. V., Jour. of Sensors 171748(2009)

21. Riziotis C., Dimas D., Katsikas S. and Boucouvalas A. C., COMADEM Proc. 669(2010)

22. Dimas D., Katsikas S., Boucouvalas A. C. and Riziotis C., COMADEM Proc. 30(2011)

23. Vasileiadis M., Athanasekos L., Meristoudi A., Alexandropoulos D., Mousdis G., Karoutsos V., Botsialas A. and Vainos N. A. Opt. Lett. 35, 1476(2010)

24. Aspiotis N., El Sachat A., Athanasekos L., Vasileiadis M., Mousdis G., Pispas S., Vainos N. A. and Riziotis C., Sensor Letters 11, 1415(2013)

25. Vasileiadis M., Alexandropoulos D., Athanasekos L., Karoutsos V., Sigalas M. and Vainos N., Jour. of Optics 12, 124016(2010)

26. Meristoudi A. et al, J. of Optics A: Pure and Applied Optics 11, 034005(2009)

27. Koo J., Smith P. G. R., Williams R. B., Riziotis C., Grossel M. C., Opt. Mater. 23, 583(2003)

28. Liang S., Scully P. J., Schille J., Vaugham J., Benyezzar M., Liu D. and Perrie W., J. Laser Micro/Nanoengineering 5, 68, (2010)

29. Mailis S., Riziotis C., Wellington I. T., Smith P. G. R., Gawith C. B. E. and Eason R. W., Opt. Lett. 28, 1433(2003)

30. Winfield R. J., Meister M., Crean G. M. and Paineau S., Mater. Sci. Semicond. Process 3, 481(2000)

31. Rytlewski P. and Zenkiewicz M., Appl. Surf. Sci. 256, 857(2009)

32. Konstantaki M., Pissadakis S., Pispas S., Madamopoulos N. and Vainos N. A. Appl. Opt. 45, 4567(2006)

33. Chen Y. T., Naessens K., Baets R., Liao Y. S. and Tseng A., Opt. Rev. 12, 427(2005)

34. Dahotre N., “Lasers in Surface Engineering”, Emptek Inc. Ontario, Canada(1998)

35. Srinivasan R. and Braren B., Jour. Polym. Sci.: Polymer Chemistry 22, 2601(1984)

36. Van Saarloos P., Vernon C. F., Chirila T. V. and Klauber C., Polymer Bulletin 33, 331(1994)

37. Lippert T., Plasma Processes and Polymers 2, 525(2005)

38. Srinivasan R., Braren B., Seeger D. E. and Dreyfus R. W., Macromolecules 19, 916(1986)

39. Srinivasan R., J. Appl. Phys. 73, 2743(1993)

40. Wochnowski C., Hanada Y., Cheng Y., Metev S., Vollertsen F., Sugioka K. and Midorikawa K., Jour. of Appl. Pol. Sc. 100, 1229(2006)

3. Prototyping and replication of special optical microstructures

3.1 Introduction

Photonic applications, in many cases, demand the creation and use of low cost microstructures that can be easily fabricated. Thus, many conventional techniques have to be avoided. In such cases, alternative techniques (computer generated holography, photolithography, soft lithography, material deposition in materials printer) become ideal tools for rapid prototyping and replication of photonic microstructures, such as diffraction gratings, Fresnel zone plates and holographic structures.

3.2 Design

3.2.1 Diffraction grating design

In this work, the design of diffraction gratings of various characteristics was performed. In an attempt to design diffraction gratings, special CAD software (Autocad®) was used. Lines of 10 mm long with a spacing dictated by the grating period sought were designed. Then, by applying the ARRAY command, the same pattern was replicated by the number needed to reach 10 mm of overall width. Thus, the designed gratings were 10 mm by 10 mm in size, with several different periods. In a complementary effort, crossed gratings were also designed, by applying the above mentioned procedure. Some of the designs are shown below in figures 3-1a & b:

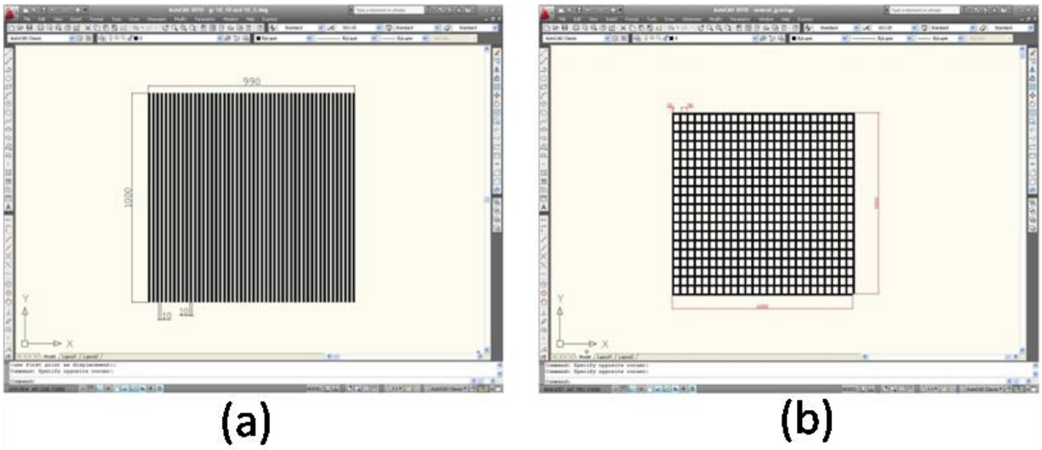

(a) (b)

Figure 3-1: (a) & (b) Typical gratings, as designed in special software.

In figure 3-2 below, typical grating structures, both simple and crossed, are presented. It should be noted, though, that the dimensions are not to the same scale.

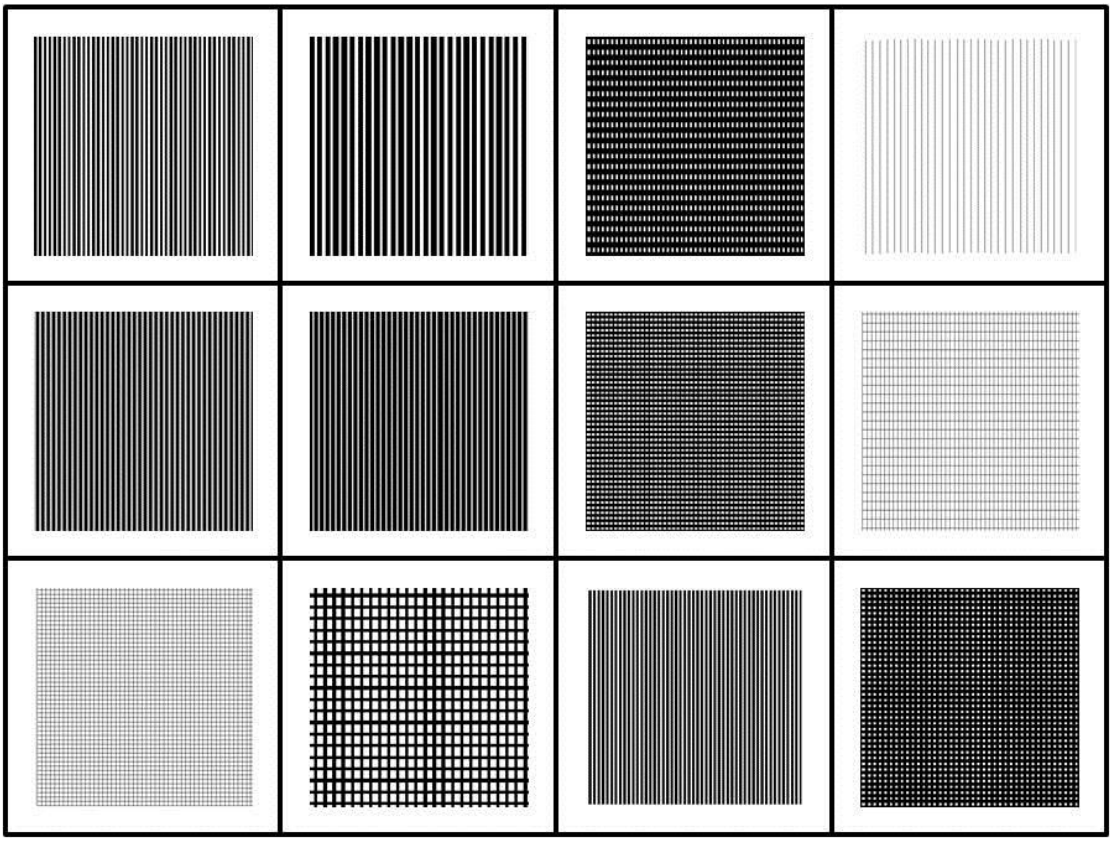

Figure 3-2: Typical diffractions gratings designed in CAD software

3.2.2 Fresnel Zone plates design

Fresnel zone plates eliminate the need for finding transparent, refractive, easy-to-manufacture materials for every region of the spectrum. The same zone plate will focus light of many wavelengths to different foci, which means they can also be used to filter out unwanted wavelengths while focusing the light of interest. Thus, in order to design Fresnel lenses, a calculation of the radius of each zone had to be initially performed. Supposing that the point source has been moved so far from the observation screen that the incoming light can be regarded as a plane wave, an expression can be derived for the radius R_m of the m_{th} zone, shown in equation 3-1 [1]:

$$\begin{aligned} {R_m}^2 &= m \cdot r_o \cdot \lambda + \frac{m^2 \cdot \lambda^2}{4} \Rightarrow \\ R_m &= \sqrt{m \cdot r_o \cdot \lambda + \frac{m^2 \cdot \lambda^2}{4}} \end{aligned} \qquad \text{[Eq. 3.1]}$$

Where

r_o: the distance of the center of the zone plate to the focus.

m: an integer

λ: wavelength

R_m: the radius of the m^{th} zone

By applying that equation, the radius of each zone was calculated as shown in table 3-1.

No of zone m	r_o (m)	wavelength λ (m)	$m \cdot r_o \cdot \lambda$	$m^2 \cdot \lambda^2/4$	$m \cdot r_o \cdot \lambda+(m^2 \cdot \lambda^2)/4$	R_m (meters)
1	0,02	0,000000633	1,266E-08	1,00172E-13	1,26601E-08	0,00011252
2	0,02	0,000000633	2,532E-08	4,00689E-13	2,53204E-08	0,00015912
3	0,02	0,000000633	3,798E-08	9,0155E-13	3,79809E-08	0,00019489
4	0,02	0,000000633	5,064E-08	1,60276E-12	5,06416E-08	0,00022504
5	0,02	0,000000633	6,33E-08	2,50431E-12	6,33025E-08	0,0002516
6	0,02	0,000000633	7,596E-08	3,6062E-12	7,59636E-08	0,00027561
7	0,02	0,000000633	8,862E-08	4,90844E-12	8,86249E-08	0,0002977
8	0,02	0,000000633	1,0128E-07	6,41102E-12	1,01286E-07	0,00031826
9	0,02	0,000000633	1,1394E-07	8,11395E-12	1,13948E-07	0,00033756
10	0,02	0,000000633	1,266E-07	1,00172E-11	1,2661E-07	0,00035582
11	0,02	0,000000633	1,3926E-07	1,21208E-11	1,39272E-07	0,00037319
12	0,02	0,000000633	1,5192E-07	1,44248E-11	1,51934E-07	0,00038979
13	0,02	0,000000633	1,6458E-07	1,69291E-11	1,64597E-07	0,00040571
14	0,02	0,000000633	1,7724E-07	1,96338E-11	1,7726E-07	0,00042102
15	0,02	0,000000633	1,899E-07	2,25388E-11	1,89923E-07	0,0004358
16	0,02	0,000000633	2,0256E-07	2,56441E-11	2,02586E-07	0,0004501
17	0,02	0,000000633	2,1522E-07	2,89498E-11	2,15249E-07	0,00046395
18	0,02	0,000000633	2,2788E-07	3,24558E-11	2,27912E-07	0,0004774
19	0,02	0,000000633	2,4054E-07	3,61622E-11	2,40576E-07	0,00049049
20	0,02	0,000000633	2,532E-07	4,00689E-11	2,5324E-07	0,00050323

Table 3-1: Numerical calculation of the radii of zone plates

After calculating the respective radii, the results were inserted in CAD software. A snapshot of a typical design process is shown in figure 3-3:

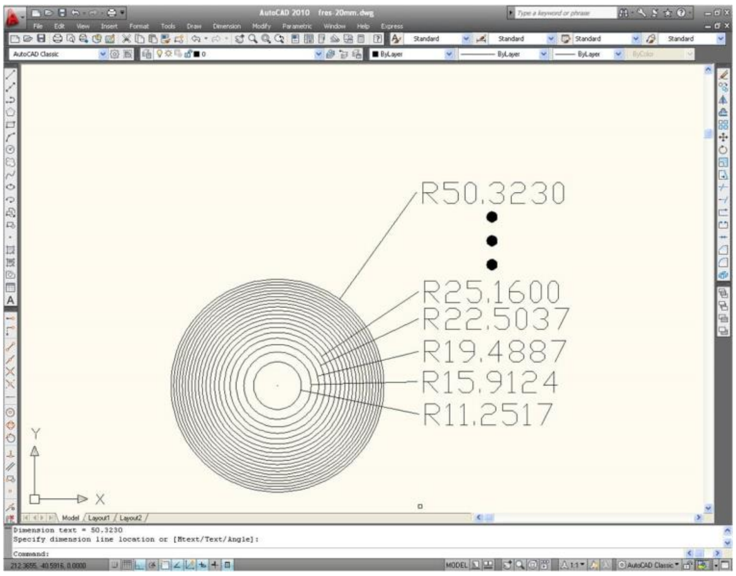

```
Dimension text = 50.3230
Specify dimension line location or [Mtext/Text/Angle]:
Command:
```

Figure 3-3: Screenshot of a Fresnel zone plate designed with the above technique

With a view to obtain a design that is appropriate as the input for the fabrication techniques, the following procedure had to be followed, as shown in figure 3-4a. In addition, two typical designs are shown in figure 3-4b.

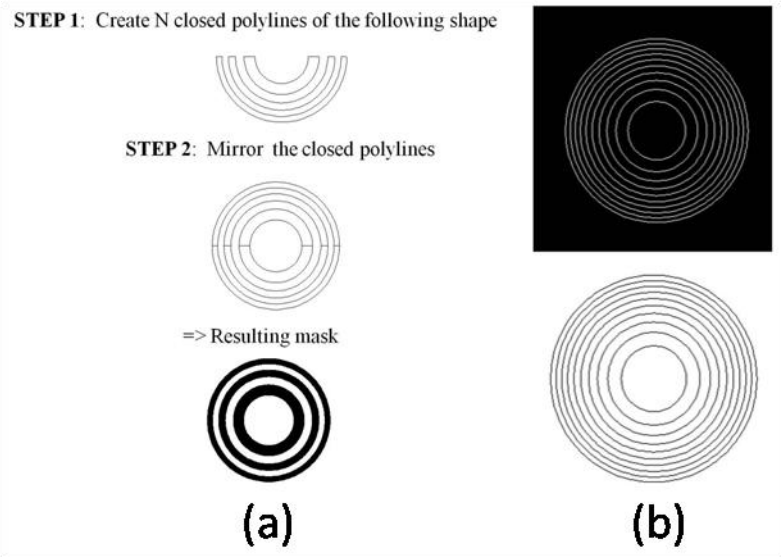
STEP 1: Create N closed polylines of the following shape

STEP 2: Mirror the closed polylines

=> Resulting mask

Figure 3-4: (a) protocol for Fresnel mask design. (b) Typical Fresnel zone plates designs

Two typical Fresnel lenses are shown in figures 3-5a&b.

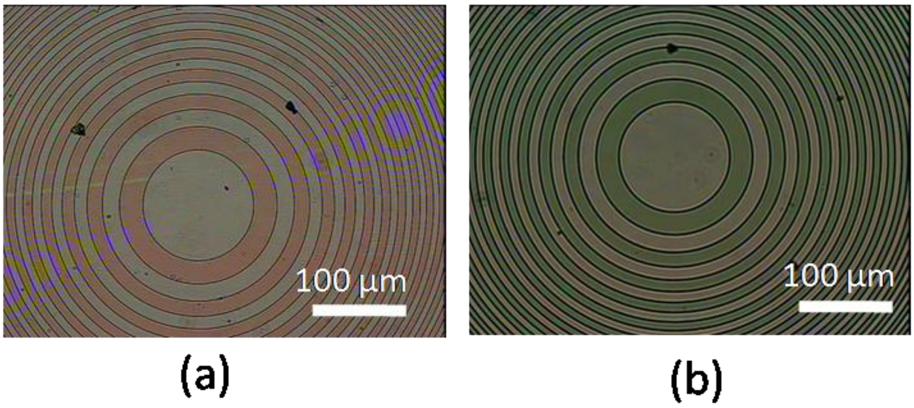

Figure 3-5: (a) & (b) Optical microscope images of fabricated Fresnel lenses.

The Fresnel lenses of figures 3-5a &b were created by DC sputtering on metallic target, and following deposition, the structures were patterned by using the aforementioned designs with photolithographic techniques[1].

3.2.3. Holographic mask design with Computer Generated Holograms software

Holography is an optical imaging method used for studying processes and events in different disciplines, in practice and also to prepare art works and protect objects against counterfeiting. The principle of holography was laid down by Gabor [2] and attained practical importance due to the invention of laser in 1960. **Computer Generated Holography (CGH)** is an emerging technology, made possible by increasingly powerful computers that avoid the interferometric recording step in conventional hologram formation. Compared to conventional holographic approaches, CGHs do not employ specialized holographic recording materials and, what is more, they can synthesize optical wavefronts without having to record a physical manifestation of them. CGHs provide flexible control of light and may be

---

[1] The structures were fabricated by Dr. Anya Piotrowska and Dr. Eliana Kaminska in IET, Warsaw, Poland whose work is acknowledged

successfully used in many applications, including optical surface testing [3] and security systems [4].

A schematic is shown in figure 3-6:

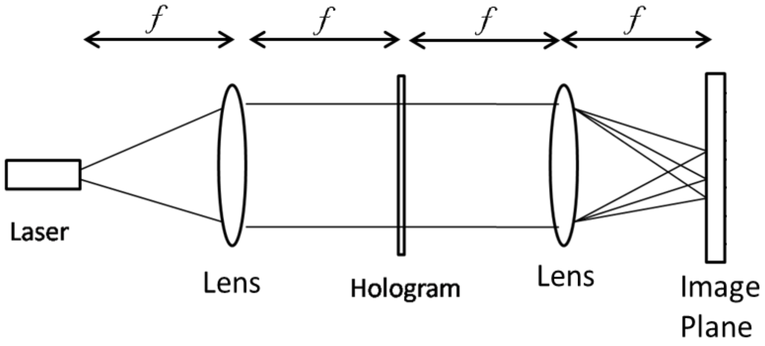

Figure 3-6: Schematic of laser illumination of holographic mask in a 4f system, where f is the focal length of each lens

CGHs can produce wavefronts with any prescribed amplitude and phase. The production of such holograms involves two steps. The first step is to calculate the complex amplitude of the object wave at the hologram plane. This is usually taken to be the discrete Fourier transform of the complex amplitude at a set of NxN points in the object plane. The second step involves using the NxN computed values of the discrete Fourier transform to produce a transparency (the hologram) which reconstructs the object wave when it is suitably illuminated. There are two basic types of CGHs: amplitude holograms and phase holograms. An amplitude hologram stores both the phase and the amplitude information of the incident wavefront, while a phase hologram assumes constant amplitude for the object wavefront and operates only on the phase function of the reconstructing wavefront. CGHs may be produced using different forms of wavefront encoding methods.

In order to acquire masks mainly for beam splitting applications, special software for CGHs was used (Holomaster®). The protocol used was as follows:

The target output is initially designed via an image editing software, e.g. Microsoft Office PowerPoint, having a white background. The colors are then inverted in special software (e.g. windows paint). The dimensions must be 50X50 pixels, due to

Holomaster® edition restraints (free version). The colors, once inverted, should be in the form of black background and white details. The image is then copied and pasted in Holomaster®. In case the image is not of the right dimensions, an error message appears. Then the four-phase mode is applied, randomized and then started. The best mask should be picked and updated on demand. A snapshot of the software used while designing a typical mask is shown below in figure 3-7:

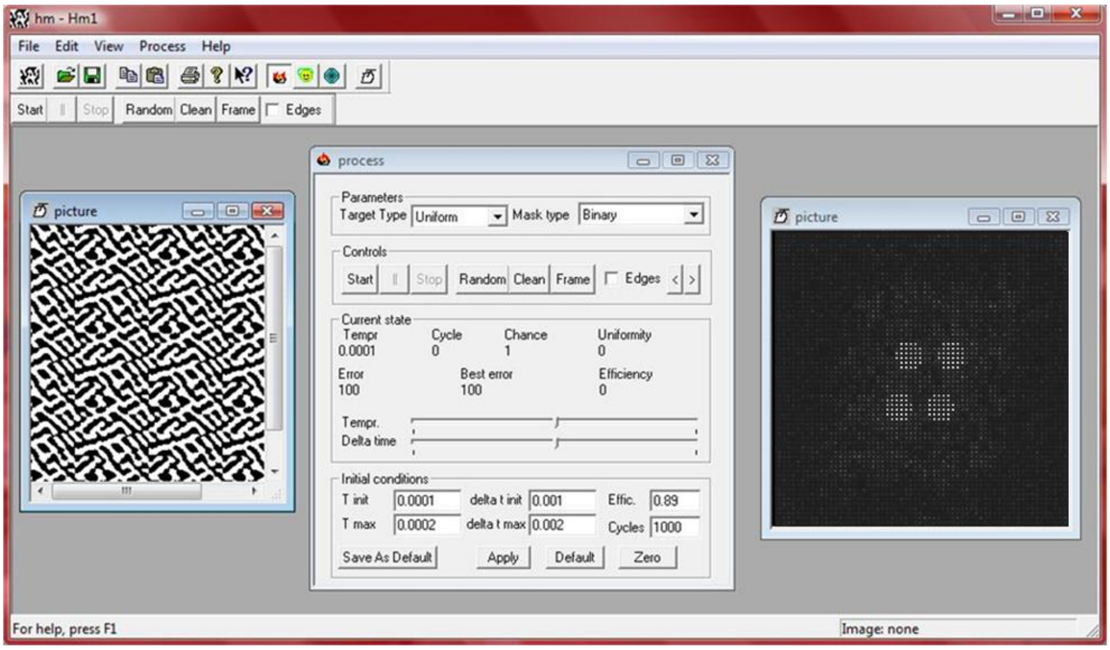

Target Type: Uniform
Mask type: Binary

Tempr 0.0001
Cycle 0
Chance 1
Uniformity 0
Error 100
Best error 100
Efficiency 0

T init 0.0001
delta t init 0.001
Effic. 0.89
T max 0.0002
delta t max 0.002
Cycles 1000

For help, press F1
Image: none

Figure 3-7: Screenshot of the software used for Computer Generated Holograms.

By changing the target output to meet our needs and applying the aforementioned protocol, several designs were generated, depending on the application. A schematic is shown in figure 3-8.

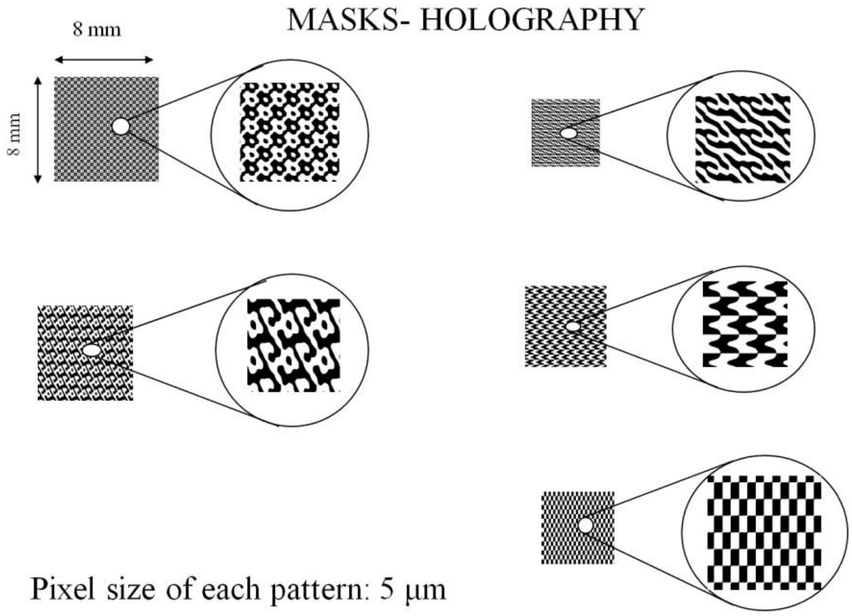

Figure 3-8: Several CGH masks, as designed in special software

Each mask was then inserted in CAD software (e.g. AUTOCAD®) for replication in order to achieve an overall mask of desired dimensions without reducing the resolution needed for our applications. The final mask designs are transferred on glass substrate with metal oxides, by using Reactive Ion Etching (RIE) technique at the Institute of Electron Technology (IET), Warsaw, Poland[2]. The final designs were then tested in order to check their quality, as shown in figure 3-9.

---

[2] The contribution of Dr. Eliana Kaminska and Dr. Anya Piotrowska is highly acknowledged

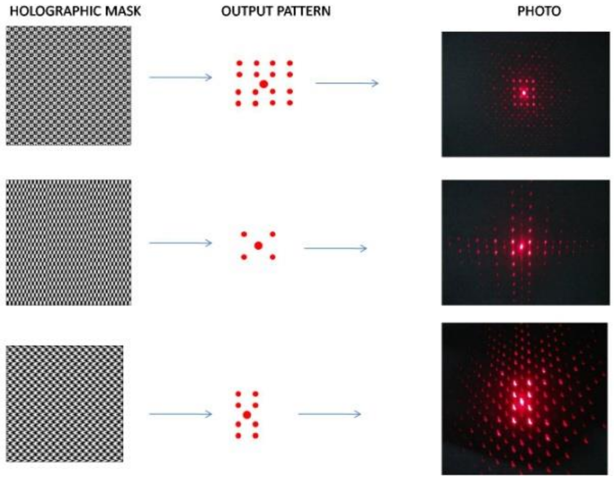

Figure 3-9: typical holographic masks (left) with their respective output (center) and real images of their fanouts (right). The zero and first orders appear brighter, as expected.

Close-ups of some typical holographic masks can be found in figure 3-10.

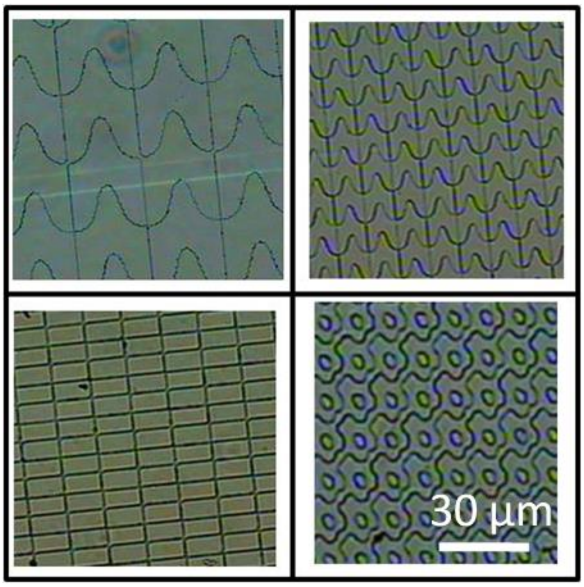

Figure 3-10: Close –ups of holographic masks (optical microscope)

As previously mentioned, by inserting the desired target, the holographic mask design could be calculated and then replicated. Thus, targets of various shapes were loaded and the resulting fanouts can be found in figure 3-11.

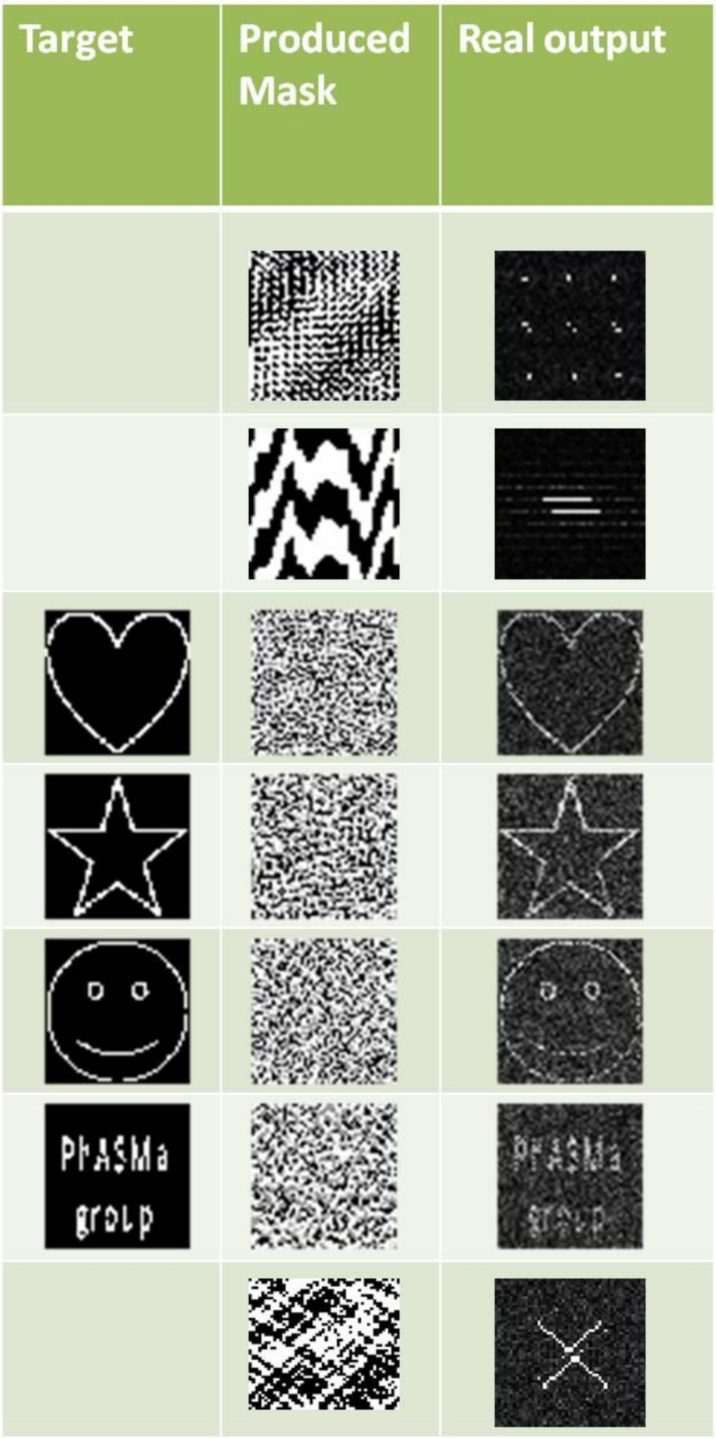

Figure 3-11: Target designs (left) with the respective holographic masks (center) and the resulting fanouts (right). By loading the suitable target, almost every image can be successfully transferred via holographic mask.

3.3 Conventional optical and laser Lithography/ Photolithography for grating fabrication

Photolithography is a process where a pattern can be transferred onto a thin film of photoresist substrate. Photolithographic techniques are capable of mass-producing patterned structures in thin films of photoresists with feature sizes as small as 250 nm [5]. However, due to its inability to achieve features of smaller sizes, advanced lithographic techniques have to be performed which include extreme UV lithography, soft X-ray lithography, e-beam writing, focused ion beam writing, and proximal-probe lithography [6, 7, 8]. These techniques have the capability to generate features in the nanoscale, but their employment in mass-production manufacturing is economically prohibitive.

Thus, alternative non-photolithographic microfabrication methods have been developed, under the generic term of soft lithography [9, 10], which involves a patterned elastomer being used as the stamp, mold, or mask to generate micropatterns and microstructures. Soft lithographic techniques are low cost, straightforward and accessible to a wide range of users.

Soft lithography utilizes cast molded stamps made from flexible materials. The process begins with the creation of a master. The master is made by etching a blank – normally a silicon wafer – with a negative photoresist. This gives a raised pattern of nanometer sized features on the silicon wafer that corresponds to the required channels in the polymer stamp. A liquid polymer is then poured on top of the silicon wafer mold. The polymer is commonly a resin like PDMS (poly(dimethylsiloxane)). The polymer is heat cured and peeled off the mold. The mold can now be used in a number of ways. The various alterations to the process determine the sub type of soft lithography.

At the next step of experimental work, several structures were fabricated using lithographic techniques.

Two categories of polymers, poly(ethylene oxide) (PEO), and poly(methacrylic acid-co-*tert* butyl methacrylate) (MAcoBMA) were synthesized and mixed with cobalt chloride in a common solvent at various concentrations to produce hybrid composites in order to be utilized as potential relative humidity (RH) photonic sensors based on hybrid polymer/inorganic materials operating by means of optical diffraction. The solutions were spin coated or cast on prefabricated grating structures. These planar linear grating structures exhibit a nearly square profile with linewidth of 50–100 μm. They were fabricated by negative photolithography and the use of commercial photo resist. They were coated or cast with the functional hybrid layer thus forming a complex system comprising a modulated effective index of refraction and a modified surface grating profile.

In order to fabricate the grating structures, negative photolithographic techniques were used. For that reason, the following steps were followed:

After both UV lamp and hot plate, which are necessary for the process, are switched on to warm up, the preparation of the developer solution requires mixing four parts of deionized water with one part developer (KOH, in our case). In order to deposit the photoresist on the glass substrate the spin coater operates at 6000 rpm. The photoresist is put on the glass substrate, formerly put on the spin coater, and it is allowed to spin for 30 seconds. Afterwards, the sample is put on the hot plate for 1 minute, and then it is cooled down. The exposure follows by turning upside down in the center of the mask in the UV lamp for about 20 seconds. Then, the sample is taken out and put in the developer for about 90 seconds. Finally the sample is thoroughly checked. If it is not in the optimum condition, it remains in the developer for 30 more seconds.

All samples were left in the clean room environment in order to dry. The final grating structures were examined for their quality and the following conclusions were derived, as summarized in figure 3-12:

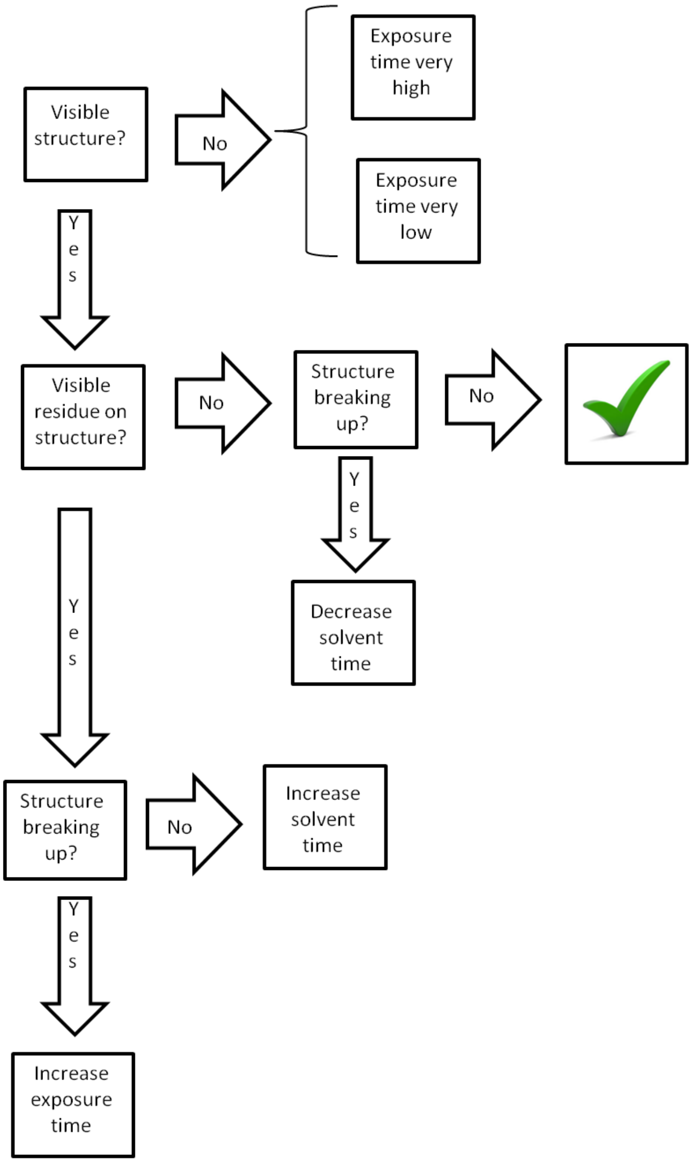

Figure 3-12: Flow diagram for photolithography steps

After the exposure process, the structures are placed on the hot plate at 110 ^{o}C for 3 minutes (thermal annealing).

After performing the following recipes, shown in table 3-2, the best recipe was found.

Sample No	spin coater speed	hot plate	UV lamp	Developer	Comments
N5	380	1 min @ 95' C	20 sec	5 min. 1/4 Developer	**X**
N6	380	1 min @ 95' C	30 sec	1:30 min. 1/4 Developer	**X (start breaking up)**
N7	380	1 min @ 95' C	30 sec	1 min. 1/4 Developer	
N8	380	1 min @ 95' C	30 sec	1:10 min. 1/4 Developer	
N9	380	1 min @ 95' C	30 sec	1 min. 1/4 Developer	
N10	380	1 min @ 95' C	35 sec	1 min. 1/4 Developer	
N11	380	1 min @ 95' C	40 sec	1 min. 1/4 Developer	
N12	380	1 min @ 95' C	40 sec	1:05 min. 1/4 Developer	**BEST**

Table 3-2: By applying different time periods in UV lamp and developer, the best recipe was obtained, giving an optimized grating structure

In order to deposit PEO (PolyEthylene Oxide) material on a prefabricated grating structure substrate, the following recipe was followed:

The substrate is initially placed on the spin coater. Then, 4 drops of material are placed on the substrate and after 45 seconds spinning at 6000 rpm for 30 seconds. Then, left for 10 minutes and repeat the process in order to deposit multiple layers on the same substrate.

3.4 Fabrication of diffraction gratings with soft lithographic techniques for ammonia sensing

A straightforward approach for the rapid prototyping and low cost development of diffraction gratings for remote chemical gas sensing was performed. Sol gel matrices incorporating various salts, as well as specially designed polymers were employed and tested as potential sensors for the detection of chemical agents under a remote point sensing scheme. The interaction between the hybrid materials and the measurands results in a reversible change of their optical characteristics that consequently modifies the gratings diffraction efficiency, resulting in an enhanced sensing ability and stable operation.

The production and replication of the diffraction grating sensors were achieved by using two soft lithographic techniques, namely solvent-assisted micro molding (SAMIM) and micro molding in capillaries (MIMIC) [11]. For the fabrication of the initial master masks the procedure followed consists of three straight-forward steps: first, the use of 193nm ArF excimer laser etching or UV masked photolithography setup for the creation of the master on a polystyrene thin film and photoresist respectively; second the fabrication of the stamp by the master and finally; the patterning of the sensing material. Here, a modified and simplified SAMIM technique (m-SAMIM) is used in order to reduce the time needed for prototyping. Typically in SAMIM the material to be replicated is spin-coated on a clean substrate and then it is softened by wetting the mold with the solvent in order to be formed by the mold. In the m-SAMIM approach, the material was simply applied on a microscope slide by a syringe in the form of a droplet and then the PDMS mold was firmly pressed against it without the additional use of solvent. The functional sensing materials used in this work are $NiCl_2$ and $CuCl_2$. The matrices for the aforementioned salts are tetramethoxyorthosilicate (TMOS) and tetraethyl orthosilicate (TEOS) mixed with deionized water, HCl 0.1 M, and isopropanol stoichiometric equivalents of $NiCl_2{\cdot}6H2O$ and $CuCl_2{\cdot}2H2O$ were added in order to obtain 5%, 10%, or 15% w/v solutions. In addition, a novel block copolymer (polystyrene sulfonate-b-*tert*-butylstyrene – SPS-b-PtBS) was used. More details on the synthesis and functional characterization of the copolymer in various gas measurands can be found elsewhere [12]. The experimental set up consisted of a He-Ne laser operating at 633 nm with 5 mW full power. A 50:50 beamsplitter was employed in order to divide the beam into the reference and the signal beam, of equal intensity. Two photodetectors were used to collect the signal and reference beams, respectively. The detectors were connected to a PC with customized software for real time data logging. The experimental setup is schematically shown in figure 3-13.

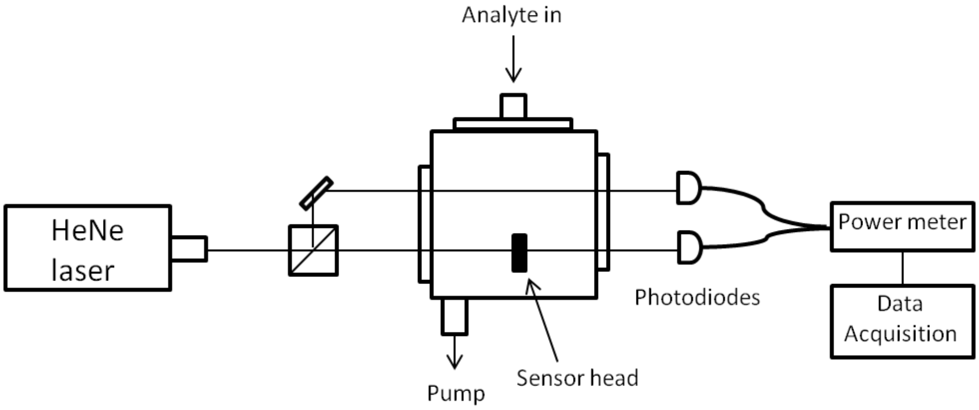

Figure 3-13: Experimental setup for sensors' characterization

The sensing head is placed inside the chamber and then, with the use of a microliter pipette (Eppendorf), small amounts of 1% aqueous solutions of ammonia are injected in the chamber and put on a peltier device. Ammonia is rapidly evaporated establishing the analyte's environment leading to reversible and measurable alterations of gratings' optical properties. In the current work, NH_3 concentrations ranging from 33 ppm to 165 ppm were measured by monitoring the zero and first diffraction orders. The functional performance characterization of the replicated gratings was performed for ammonia detection, using different salts, namely $CuCl_2$ and $NiCl_2$ in different matrices (TMOS, TEOS), in several combinations, and are shown in figure 3-14.

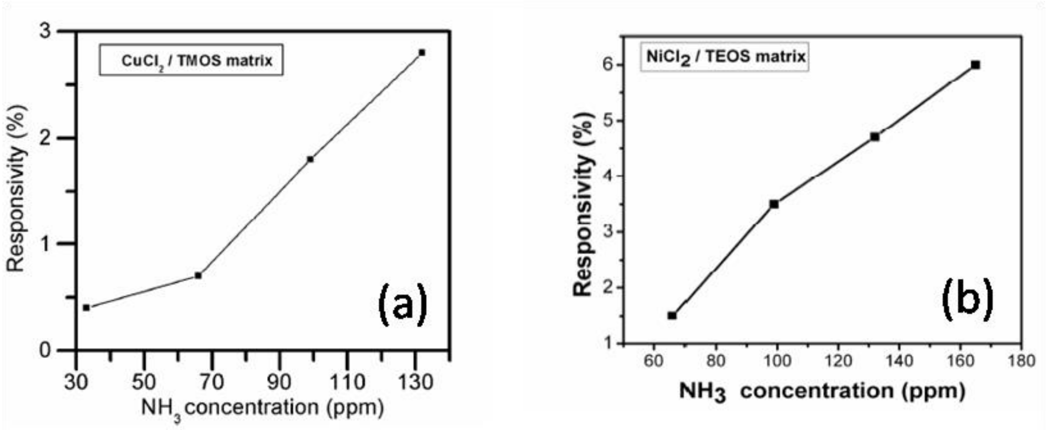

Figure 3-14: The responsivity of the grating based sensors with sensing materials $CuCl_2$, $NiCl_2$ for different matrices (TMOS,TEOS), versus the concentration of NH_3.

Additionally to the use of sol-gel materials, a novel block copolymer material was also tested and demonstrated a very low detection limit at about 30 ppm with a linear response, as shown in figure 3-15. The characteristics of this copolymer could be customized and optimized by changing the ratio of the two blocks and thus allow the detection of other gases like aromatic hydrocarbons [13].

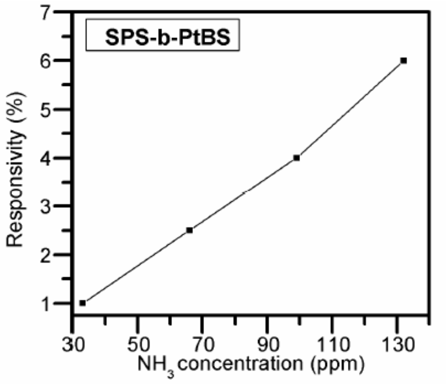

Figure 3-15: The responsivity of the grating based sensor, with block co-polymer SPS-b-PtBS, versus ammonia concentration.

The obtained results confirm the efficient and low cost implementation of point gas sensors for a variety of measurands. By further optimizing the fabrication technique of the gratings and the sensing platform and by employing also customizable sensitive materials this sensing approach could attract a lot of interest in various applications.

3.5 Fabrication/ Deposition of diffractive patterns on thin films by ink jet printer

The scope of this work was the design, implementation and analysis of diffractive patterns with both organic and inorganic materials on silica substrates by use of a materials printer for photonic sensing applications. The work was performed in the frame of a Short Term Scientific Mission (STSM) in Dublin Institute of Technology (DIT) and Facility for Optical Characterization and Spectroscopy (FOCAS Research Institute), Dublin, Ireland under the supervision of Prof. Vincent Toal[3].

3.5.1 Organic, Inorganic and hybrid materials deposited with inkjet printer

The materials used for this work are shown below in Table 3-3.

---

[3] The contribution and help of Prof. Toal group and Dr. Naydenova is highly acknowledged.

Table 3-3 : Solutions used in inkjet printer

No.	**Solute**	**Solvent**
1	tetramethyl orthosilicate (TMOS)- $NiCl_2$	Isopropanol
2	Poly (Isoprene-b-Acrylic Acid) with Au nanoparticles	THF
3	Poly (Styrene Poly-b-2-Vinyl Pyridine) with Au nanoparticles	Toluene
4	PolyEthylene Oxide (PEO) - $CoCl_2$	Water

Operation note

The printer used was a FUJIFILM DIMATIX (DMP-2800 series) inkjet printer (figure 3-16).

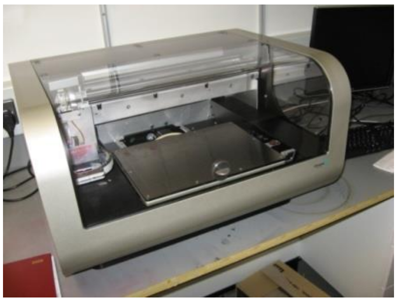

Figure 3-16: Image of the materials printer installed in FOCAS Institute, Dublin Institute of Technology (DIT), Dublin

The materials printer is able to jet a wide variety of aqueous and solvent-based fluid solutions. Limitations include viscosity of 10 cP and surface tension of 30 dynes/cm. The fluid is injected into the cartridge which is filled using a syringe and needle. In order to avoid clustering with a consequent inability of the solution to be ejected from the nozzles, a filter is used to assure that no aggregation takes place inside the cartridge. The solution is initially sonicated in an ultrasonic bath in order to agitate the particles and break any intermolecular interactions that form aggregates in solution. The ink jet head cartridge is heated up to 70 ^{o}C which is the critical value. Consequently, all solutions to be used should remain unaffected up to that temperature. The boiling point of solvents used should be far above that value in order for the solvent not to evaporate. In addition, the platen where the substrates are placed warms up to 60 ^{o}C.

The cartridge is available in two sizes, namely for 1 pl and 10 pl drop volumes. The 1 pl cartridge can deposit features as small as 20 μm. Unfortunately, that size was not available during the experiments. Using a 10 pL drop (cartridge) as applied in our case, a 40 μm spot could be produced. Thus, it is not possible to go below that value for a single spot. The orifice size of the nozzle is 21.5 μm.

The material printer software has some preloaded test patterns. In addition, a pattern generator can be used to create more patterns. Furthermore, patterns could be imported for printing in DXF (CAD) and bitmap format. Prior to the printing process, the solutions were left for sonication for about 1-2 hours and then were filtered through a 200 nm filter. Thus, all particles or clusters bigger than that size were trapped. The spacing between nozzles is 254 microns (100 dpi) for a single row.

Patterns to be jetted are resolved into 5 micron pixels. This restricts the smallest increment between adjacent drops at 5 microns which is equivalent to 5080 dpi. At this spacing it is possible to get drop overlap on the substrate because most spots will be at least 40 microns in diameter. The stages use 1μm encoders. In case of single spot action, it is possible to disable some or all of the nozzles.

The printer has a fiducial camera. This camera is mounted on the carriage of the printer. Once the first print of a series of prints (overprinting or printing a sequence of fluids) has been made, it is possible to create marks with the aid of the camera. When the cartridge or substrate has been replaced, the marks are manually located in the last position used. Software will compensate for any positional errors. Moreover, the fiducial camera can be used for real time monitoring of the printing process.

Another useful operation is the additional drop watcher camera (figure 3-17). This assures the right operation of all nozzles. If a nozzle is blocked due to a possible solution aggregate, it is shown in real time.

The nozzles are piezoelectrically operated, thus by adjusting the voltage, it is possible to allow more or less liquid to be ejected.

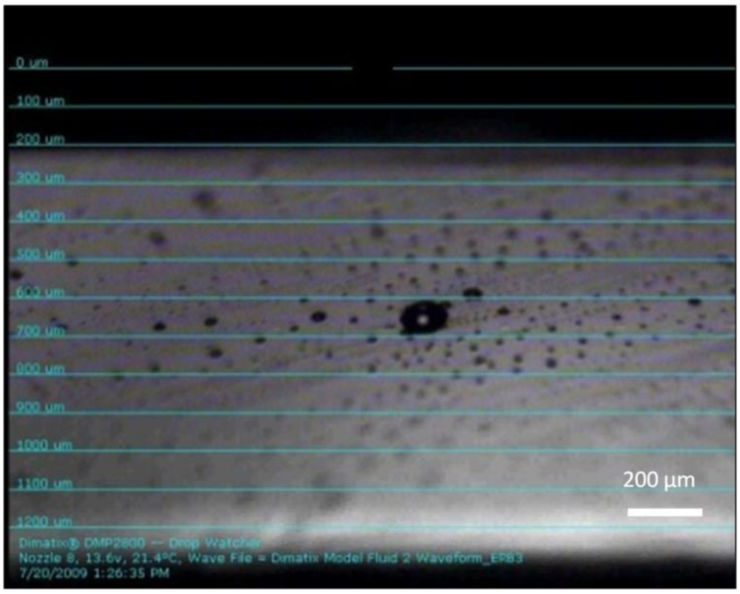

Figure 3-17: Drop watcher in action

During the process, several issues arose, related not only to the printer operation, but also to the solutions that were inserted in the cartridge. In particular:

- The viscosity of the solutions to be printed was found to be crucial. Thus, prior to printing, the viscosity had to be decreased by adding solvent.

- Experiments were performed during summer and solutions were sent by courier (it was not possible to carry them during travelling due to safety airport rules). This resulted in the TMOS-$NiCl_2$ solution deterioration (creation of aggregates).

- The TMOS-$NiCl_2$ solution due to its highly volatile solvent (isopropanol) was evaporated long before the experiment. Even after the addition of solvent at the time of the experiment aggregation of sol-gel material made the printing process impossible.

- Not all the nozzles operated at the same time. Blocking of nozzles was frequent. This resulted in a discontinuous printing.

- In the case of PEO-$COCl_2$ grating, although there was an overlap between drops, the edges were not smooth, thus scattering was apparent, upon testing it.

- It was observed that during the printing process, splashes of material were apparent on the glass substrate due to the very smooth surface (figure 3-18). In order to improve the resulting structures, glass substrates were left in THF for some minutes to increase the roughness.

- In many cases, the nozzles were initially working, but then they stopped due to clogging. Thus, the first line of the grating is good, but then it deteriorates (figure 3-18). Apparently, there was a blockage of the nozzles, due to a clustering of particulates of the solution used.

- Toluene, as a solvent used, was seen to react with the container material. Thus, it could not be used.

Results

After preparing the materials, several designs (gratings, crossed gratings and holographic masks) were imported in the printer software. Gratings were created at 10 lines/mm and crossed gratings were of 8 lines/mm spatial frequency.

In more detail, regarding the printing of each material:

TMOS-$NiCl_2$: Due to the high volatility of sol-gel solvent (i.e. isopropanol) and its low boiling point (82^oC), printing was not possible for TMOS-$NiCl_2$ solution. The absence of solvent created clusters and aggregation of material in the cartridge reservoir that blocked all of the 16 existing nozzles. Even by further diluting the solution, no successful printing could be performed. Furthermore, sol-gel material was found to be of low quality for the aforementioned reasons.

PIPAA- Au : The low boiling point of the solvent (66 °C), was far below the printer specifications that had to be met. Thus, printing with that material could not be performed.

PS-P2VP – Au : Upon testing the liquid in the drop watcher, it was noticed that none of the nozzles were operating. By further purging the solution in the cartridge reservoir, the situation was not improving, due to possible aggregation- clustering of the Au nanoparticles. The solution was filtered with a 200 nm grid filter, which was large compared to nanoparticles size and thus they could still pass through the filter and block the nozzles resulting in printing inability. Furthermore, it was noticed that in the cartridge reservoir there were small pieces of material, whereas they were not there at first. Since the solvent used in that case was toluene, it is highly possible that the toluene reacted with the reservoir plastic material.

PEO – $CoCl_2$: The PEO – $CoCl_2$ material gave promising results, although many printing parameters had to be optimized in order to have “clean” diffraction orders, without scattering. The solution had to be further diluted with water. Initial attempts showed many splashes on the substrate, stemming from the high velocity of droplets falling on the silica substrate (figure 3-18a). The resulting diffraction exhibits very low quality, as shown in figure 3-19a. By alternating the printing parameters several results were obtained (figures 3-18c and 3-18d).

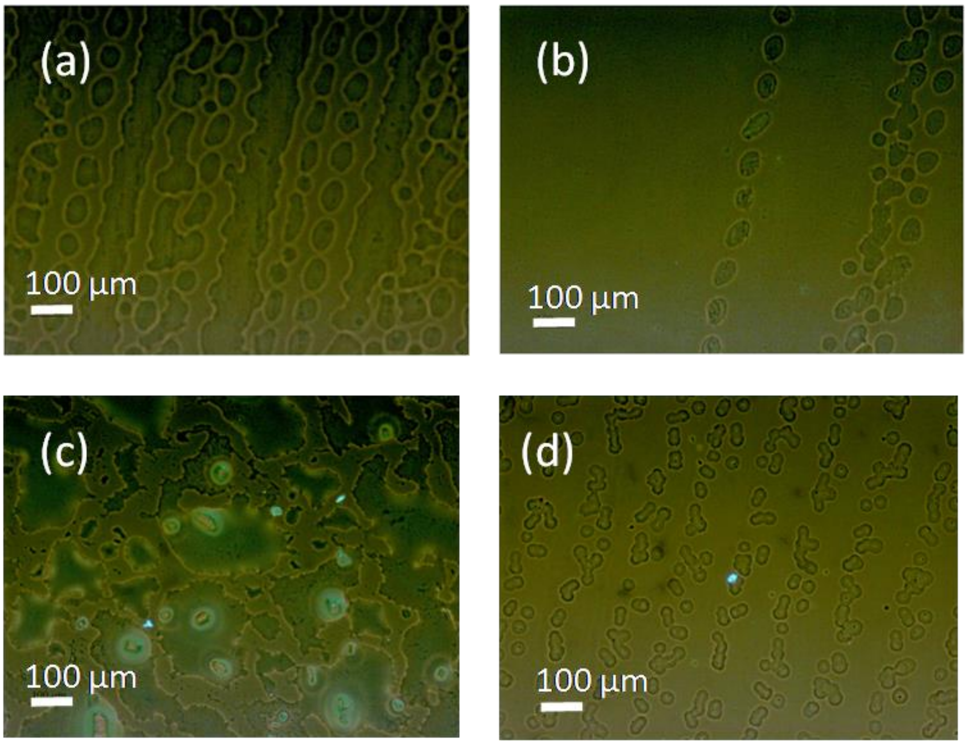

Fig. 3-18: (a) Microscope image of a grating. Many drops splashed between the grating lines are visible. (b) Much better result was obtained by reducing the droplet speed. (c) & (d) Several attempts were performed by alternating the printing conditions.

After compensating for that splashing effect by reducing the speed of droplets, the result was much better (fig. 3-18b), resulting in a grating with less scattering on the projection field (fig. 3-19b).

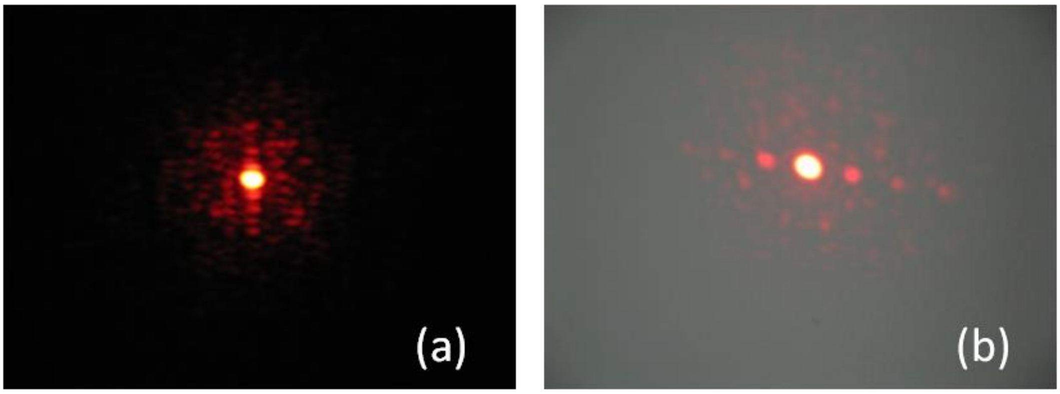

Figure 3-19: Diffraction with (a) much and (b) less scattering. The effect of droplet speed on substrate is important for the final structure.

The formed gratings were characterized with an interferometric microscope, producing 3-D representations of the surface morphology (fig. 3-20)

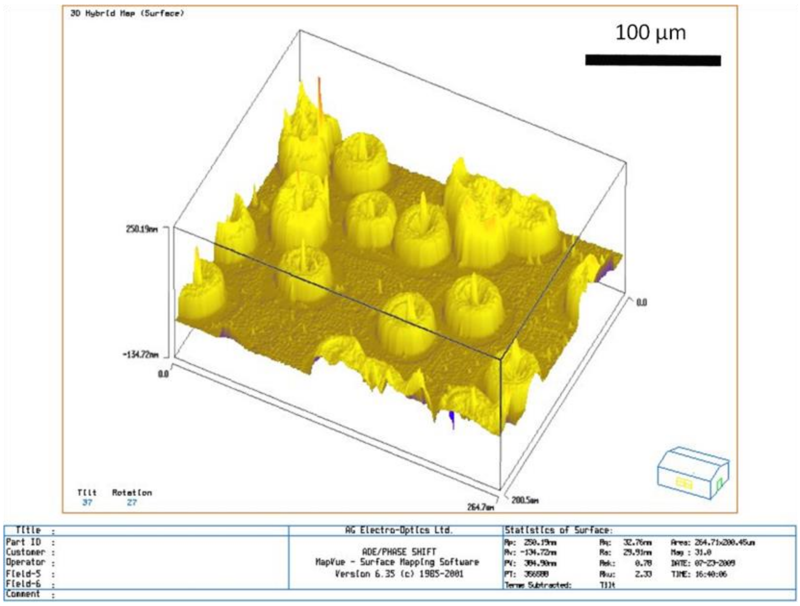

Title :	AG Electro-Optics Ltd.	Statistics of Surface:
Part ID : Customer : Operator : Field-5 : Field-6 :	ADE/PHASE SHIFT MapVue - Surface Mapping Software Version 6.35 (c) 1985-2001	Rp: 250.19nm Rq: 32.76nm Area: 264.71x200.45um Rv: -134.72nm Ra: 29.91nm Mag : 31.0 PV: 384.90nm Rsk: 0.78 DATE: 07-23-2009 PT: 356588 Rku: 2.33 TIME: 16:40:06 Terms Subtracted: Tilt
Comment :		

Fig. 3-20: Interferometric microscope 3-D representation of the surface morphology of a structure.

A close-up of a grating structure is shown in figure 3-21 where individual drops are visible

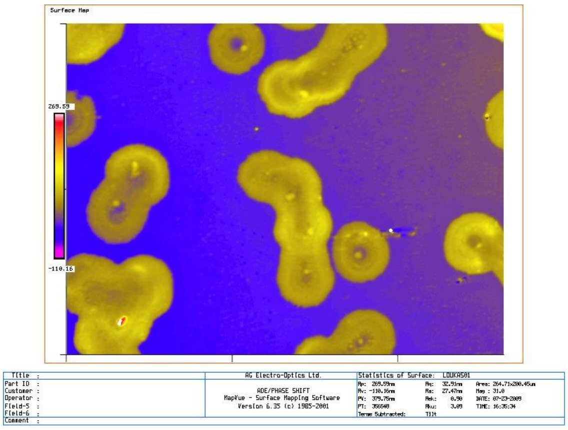

```
Title    :                     AG Electro-Optics Ltd.          Statistics of Surface:  LOUKAS01
Part ID  :                                                     Rp:  269.59nm     Rq:  32.91nm    Area: 264.71x200.45um
Customer :                     ADE/PHASE SHIFT                 Rv: -110.16nm     Ra:  27.47nm    Mag : 31.0
Operator :               MapVue - Surface Mapping Software     PV:  379.75nm     Rsk:   0.90     DATE: 07-23-2009
Field-5  :                Version 6.35 (c) 1985-2001           PT:  356548       Rku:   3.09     TIME: 16:35:34
Field-6  :                                                     Terms Subtracted:  Tilt
Comment  :
```

Figure 3-21: A close-up of a grating structure

Further optimization of the printing process parameters (use of suitable solutions and solvents, use of 1 pL cartridge) could result in the successful deposition of material and the creation of diffractive elements that could be used as potential photonic sensors.

3.5.2 Dye deposition lithography

In another attempt, several structures were printed with dye on photopolymer, previously spin-coated on a silica substrate. Patterns of gratings with different periods, crossed gratings, Fresnel zone plates and holographic designs were successfully printed. The structures were then exposed to UV irradiation in order photo polymerization to take effect.

The technique is based on patterned dye deposition on an unsensitized photopolymer layer and is based on the principle that the occurs only where the photosensitizer (dye) is present.

An acrylamide-based photopolymer was used in this study. Photopolymerization, after illumination with visible light, can be initiated in a photopolymer layer only if it consists of a monomer, a co-initiator and a photosensitizer. If the photosensitizer is absent from the photopolymer layer then it is impossible to trigger the polymerization process. Erythrosine B dye was utilised as a sensitizer at 532 nm. The dye was deposited on the unsensitized photopolymer layer to pattern the desired optical component by means of the materials deposition printer. The layer was then exposed to 532 nm single laser beam, required for completion of the device fabrication by polymerization confined to the dye-sensitized location leading to the refractive index modulation. The principle of the fabrication technique is shown in figure 3-22.

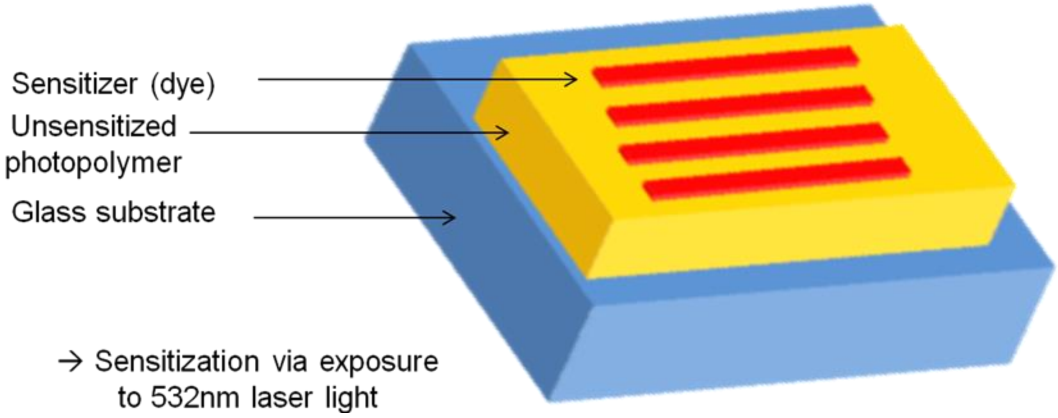

Figure 3-22: The principle of dye deposition lithography

Preparation of unsensitized photopolymer layers

All the components of the acrylamide-based photopolymer except the photosensitizer were thoroughly mixed using a magnetic stirrer. This solution was filtered through 0.20 µm filters before spreading on a glass plate. 0.30 ml of the unsensitized photopolymer was spread on a glass plate of 7.5 x 2.5 cm^2 in area and was allowed to dry for 24 to 36 hours. The thickness of the dry layers was 30 ± 3 µm.

The patterns generated by the software were printed on the unsensitized photopolymer layer using the materials printer. The size of the gratings and crossed gratings was approximately 1x1 cm^2 and that of the holographic pattern was 0.7x0.7 cm^2 . It was observed that in order to obtain a device of thickness around 25 µm, 1 hour delay time was required. After that the printed layers were exposed to 532 nm laser illumination. The exposure intensity was 7.5 mW/cm^2 for 150 s.

In order to study the diffraction patterns of the fabricated optical fan-out devices, a He-Ne laser (633nm) was used. The refractive index profile of the optical components was studied using phase contrast microscopy.

The diffraction pattern and the phase contrast image of the grating are shown in figure 3-23a and 3-23b, respectively. The diffraction efficiency of the two first orders of the grating was measured to be 16 %. Figures 3-24a and 3-24b show the diffraction pattern and phase contrast image of the printed crossed grating, respectively. It was observed (figure 3-24(b)) that during the printing process the horizontal lines were continuous while there was some discontinuity in the vertical lines, which can be attributed to possible overlap mismatch between the drops.

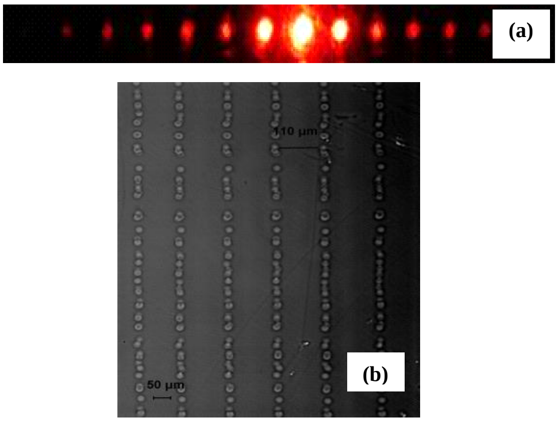

Figure 3-23: (a) Diffraction pattern of the grating and (b) phase contrast image of the grating.

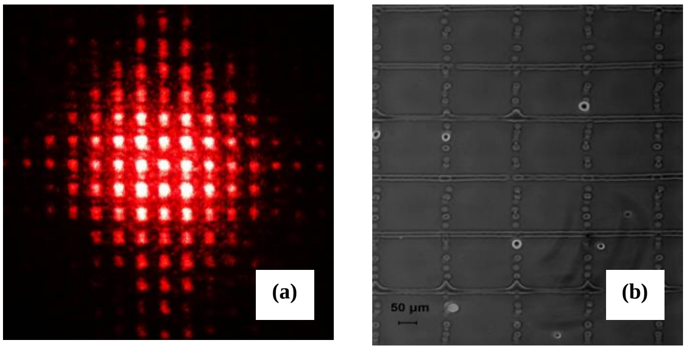

Figure 3-24: (a) Diffraction pattern of the crossed grating and (b) phase contrast image of the crossed grating.

The diffraction pattern and phase contrast image of a holographic pattern are shown in figure 3-25. Figure 3-25(b) presents the expected output diffraction pattern for a holographic pattern. Although the desired output was achieved, there was also significant background due to scattering. The phase contrast image of the pattern (figure 3-25c) shows that there are imperfections in the printed image and thus optimization on the deposition process is needed.

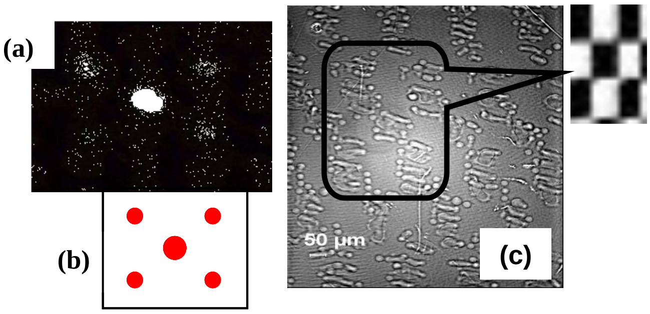

Figure 3-25: (a) Diffraction orders of the holographic pattern (b) expected output pattern and (c) phase contrast image of the holographic pattern.

The results were published in several conferences [14,15]

3.6 References

1. Hecht E., “Optics”, Addisson-Wesley(1974)

2. Gabor D., Nature, 161, 777(1948)

3. Shen H. et al., Chinese Optics Letters 11, 3, (2013)

4. Yoshikawa N., Itoh M. and Yatagai T., Optics Letters 23, 18, 1483(1998)

5. Levenson M.D., Solid State Technology 57, 14(1995)

6. Pease R., J. Vac. Sci. Technol. B10, 278(1992)

7. Cerrina F., Marrian C., Mater. Res. Soc. Bull. XXI, No. 12, 56(1996)

8. Burn J. L., C.R. Physique 7, 858(2006)

9. Xia Y., “Soft lithography: Micro and Nanofabrication based on Microcontact Printing and Replica Molding”, PhD thesis Harvard Univ., Cambridge (1996)

10. Zhao X. M., Xia Y., Whitesides G.M., J. Mater. Chem. 7, 1069(1997)

11. Xia Y. and Whitesides G. M., Annu. Rev. Mater. Sci 28, 153(1998)

12. Athanasekos L., Pispas S. and Riziotis C., Proc. SPIE 8426, 842615(2012)

13. Athanasekos L., El Sachat A., Pispas S. and Riziotis C., J. Polym. Sci. B Polym. Phys., 52, 46(2014)

14. Pavani K., Athanasekos L., Martin S., Vainos N. A., Toal V. and Naydenova I., Proceedings”Emerging trends “, Delphi, Greece, October (2009)

15. Clarke G., Pavani K., Athanasekos L., Martin S., Vainos N. A., Toal V., Naydenova I., ICO-22, 15-19 August, Puebla, Mexico(2011)

4. Photonic structures for sensor applications

4.1 Introduction

The emerging necessity for sensors dates many decades back. Thus, with the advent of the photonics era, photonic sensors were a “spin-off” from other technologies. Upon seeing the potentiality in sensing applications, it was developed as its own field. Optical sensor virtues (e.g. electromagnetic immunity and isolation, wide dynamic range, amenability to multiplexing and others) made them ideal for a wide variety of measurands such as temperature, pressure, displacement, vibration, humidity, Volatile Organic Compounds (VOCs), pH etc.

4.2 Laser microfabrication of diffractive gratings for ammonia sensing

Diffraction gratings were employed in the sensing field due to their versatility and ease of use and are now widely used as stand-alone devices upon deposition of a sensitive material on their surface or as embedded components in complex systems (e.g. fiber Bragg gratings). Earlier demonstrations of optical sensors have provided nanocomposite photonic materials incorporating nanoparticles in inorganic and organic matrices and enabled humidity, methanol, and ammonia sensing [1, 2]. Here, a novel scheme is approached enhancing the performance of a photonic sensor for the detection of ammonia by laser patterning surface relief diffractive elements on the environmentally-sensitive optical interface using an excimer ArF laser source.

The experimental setup, shown schematically in figure 4-1, comprises a visible laser beam that propagates in free space and interrogates the “sensor head” which in turn becomes modulated and produces the sensor signal. The sensor head is electrically passive, thus not electrically connected to any power or signal processing unit. The induced optical changes are translated to measureable alterations of the transmitted/reflected diffracted beams.

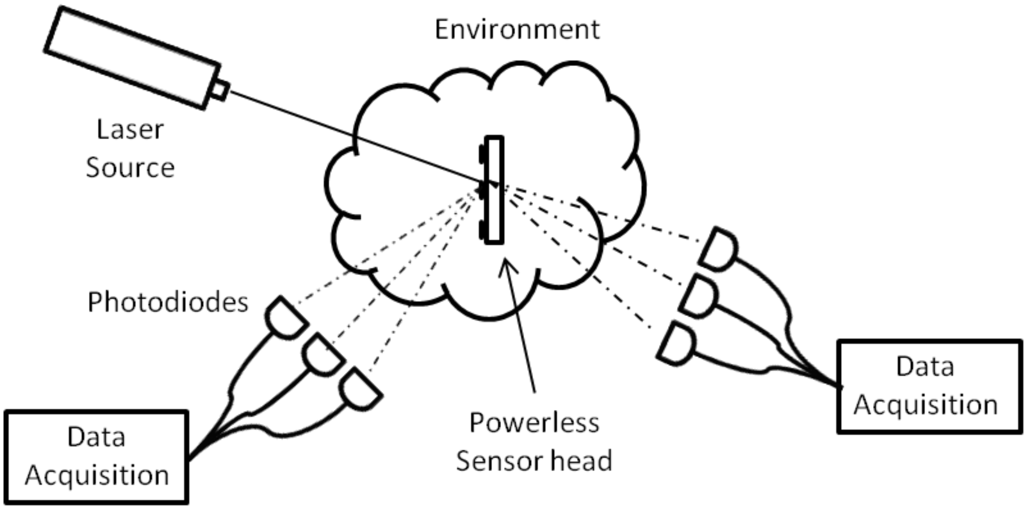

Figure 4-1: Optical remote-point scheme.

The sensitive material used in this work has been produced by sol-gel methods [3], using tetramethyl orthosilicate (TMOS). $NiCl_2$ nanoparticles were *in situ* synthesized in the silica matrix by adding $NiCl_26H_2O$ and stirring. The material was then spin coated on glass substrates to form thin film structures.[4] The thin film structures of about 1.4 μm thickness are then deposited on glass substrates. The presence of ammonia in the nickel salt clusters produces complexation and enables the exchange between captured water and diffused ammonia molecules.

Upon interaction of the sensitive material with the analyte, variations of the effective refractive index of the material occur [1], with the concurrent volume expansion that eventually change the geometry and results in the alteration of the relative optical paths in the diffractive element and respective variation of the diffraction efficiency.

Direct UV laser microetching methods have been implemented for patterning the desired structures [4]. Tailoring of the thin film surface morphology by other means (e.g. lithography) is not possible, due to the fragility of the material itself. Thus, an

---

[4] The material synthesis was performed by Dr. G.Mousdis group in TPCI, NHRF and is acknowledged.

ArF excimer laser (@ 193 nm) based microfabrication system allows irradiation of the surface by 5 mJ nanosecond pulses. The use of nanopositioning stages ensures accurate patterning of high-quality. What is more, minimum penetration depth and negligible thermal loading of the material is achieved by the use of the specific laser. Images of the micromachining station are shown in figures 4-2a and b.

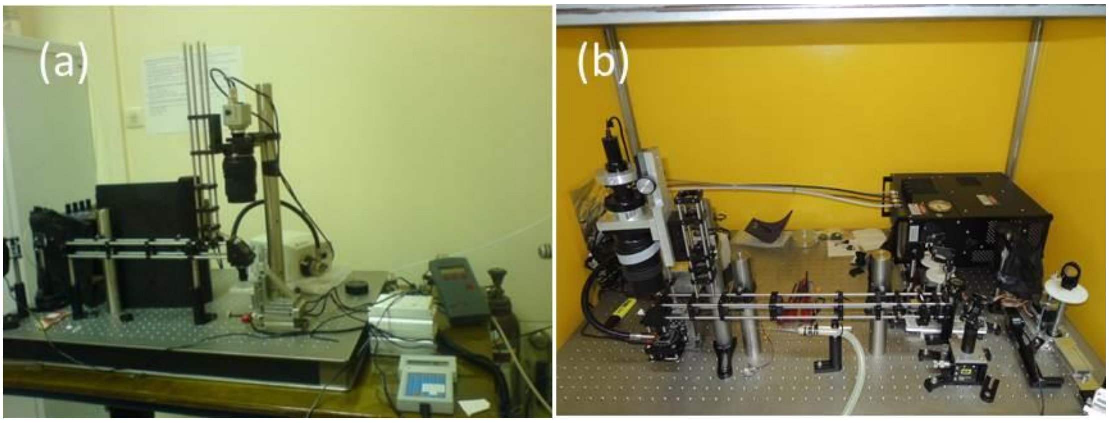

Figure 4-2: (a) First development of the excimer laser microprocessing station and (b) current version of the station.

Initial attempts revealed some defects on the final structure, as shown in figure 4-3a and b which were compensated by optimizing the process. High-quality ablative processing at 60 mJ/cm^2 pulse energy density results in diffraction gratings with spatial period in the range of Λ=10–100 μm fabricated on the sensitive surfaces. A scanning electron micrograph (JEOL 6300) and a surface profile (Tencor Alpha-Step 500IQ) of optimized structures are shown in figure 4-4. The nearly square profile of structures produces multiordered diffraction patterns upon laser illumination.

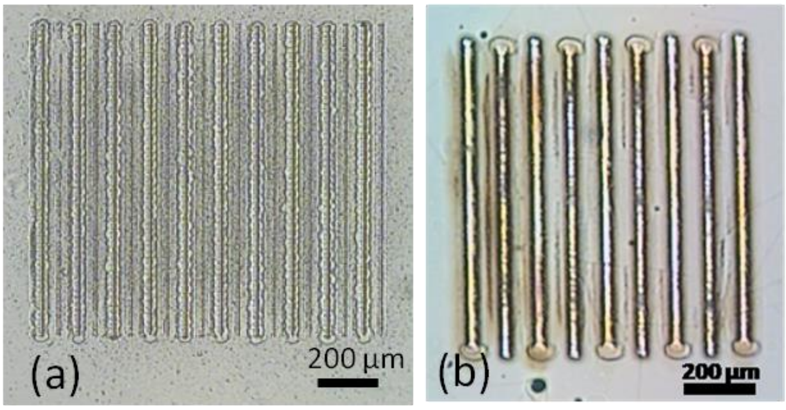

Figure 4-3: (a) and (b) :Optical microscope image of original first prototype grating structures developed by the use of microprocessing station. (b) Edge defects are visible due to multiple pulse irradiation.

After the optimization of the procedure, better results were obtained, as shown in figure 4-4a.

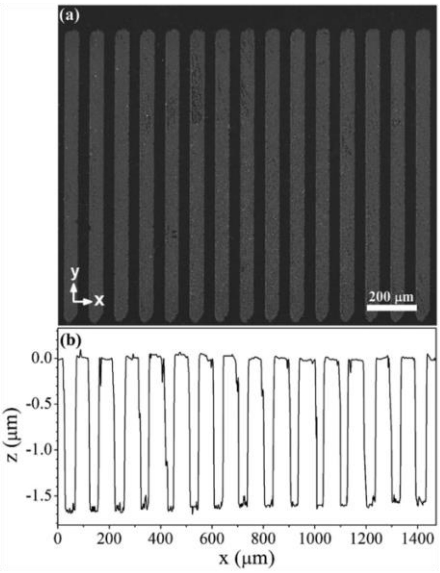

Figure 4-4: (a) Scanning electron microscope image of the laser microetched TMOS-NiCl$_2$ sensor grating (Λ=80 µm) and (b) the respective surface profile

4.2.1 Experimental sensor testing

The sensor structure was placed inside the testing chamber and was interrogated in the transmission mode using a 5 mW He–Ne laser beam emitting at λ =633 nm. A reference beam used provides balance to any laser power fluctuations. The −1, 0, and +1 diffraction orders, as well as the reference beam, were monitored. Ammonia environment is induced by injecting small (~ μl) volumes of ammonia in liquid solution followed by evaporation aided by a peltier device. In order to apply each new cycle, the original ambient environment is restored by evacuating the chamber. The photonic sensor head is positioned for interrogation at ~22° beam incidence to attain the experimentally determined maximum responsivity. This geometry, corresponding to the maximum slope of the diffraction efficiency curve, has been verified by a series of real-time recordings at varying incidence angles. The diffraction angle of the ±1 orders, measured with respect to the zero order, is found at 0.45°, while diffracted beams up to the 10th order were observable.

Typical real-time recordings of the transmitted signals are shown in figure 4-5. In the recordings, a 150 ppm ammonia environment is established and is consequently followed by the pure atmospheric ambient.

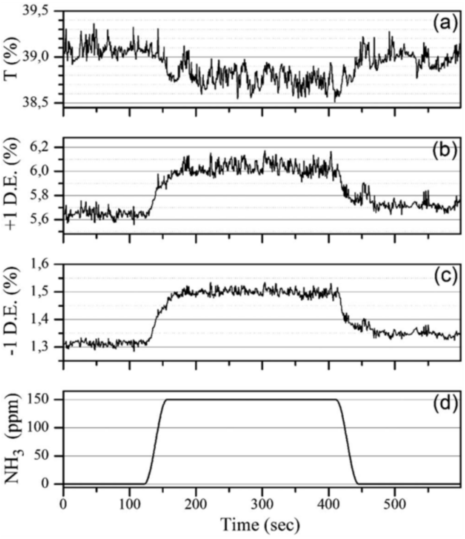

Figure 4-5: Temporal response of (a) zero order and (b)(c) ±1 order to 150 ppm of ammonia [shown in (d)].

It should be noted here that an equilibrium of the system is restored with the outdiffusion of ammonia at a longer time scale, of the order of 15–20 min.

The responsivity of the diffractive sensor is defined as shown in Eq. 4-1:

$$R_m=\Delta n_m/(n_{m,0}\ \delta C) \quad [4.1]$$

which is the normalized variation of the m_{th}-order diffraction efficiency n_m per unit analyte concentration change δC(ppm), where $n_{m,0}$ is the diffraction efficiency of the element at the absence of analyte. For a planar unprocessed sensor interface the normalized variation, $R_T=\Delta T/(T_0\delta C)$ of optical transmission, T may be equivalently defined. This definition is also valid and used here for the zero-order undiffracted beam, R_0.

In Figure 4-6, the response of the sensor for various ammonia concentrations for the zero and ±1 order diffraction beams is presented as a comparison. The response of the unprocessed planar thin film sensor is recorded by a laser beam incident on the same sample at the same angle of incidence. The measured zero-order responsivity values R_0~9.2X10^{-5} ppm^{-1} are found to be similar to those of the unprocessed planar interface, R_T. It is noted here that the expected value due to Fresnel reflection variation is ~10^{-6} ppm^{-1}, and that the observed value is a result of the etalon effect due to the overall film-substrate planar structure. A sixfold responsivity increase for the ±1-order beams is, however, found at R_{-1}~5.3X10^{-4} ppm^{-1} and R_{+1}~2.1X10^{-4} ppm^{-1}.

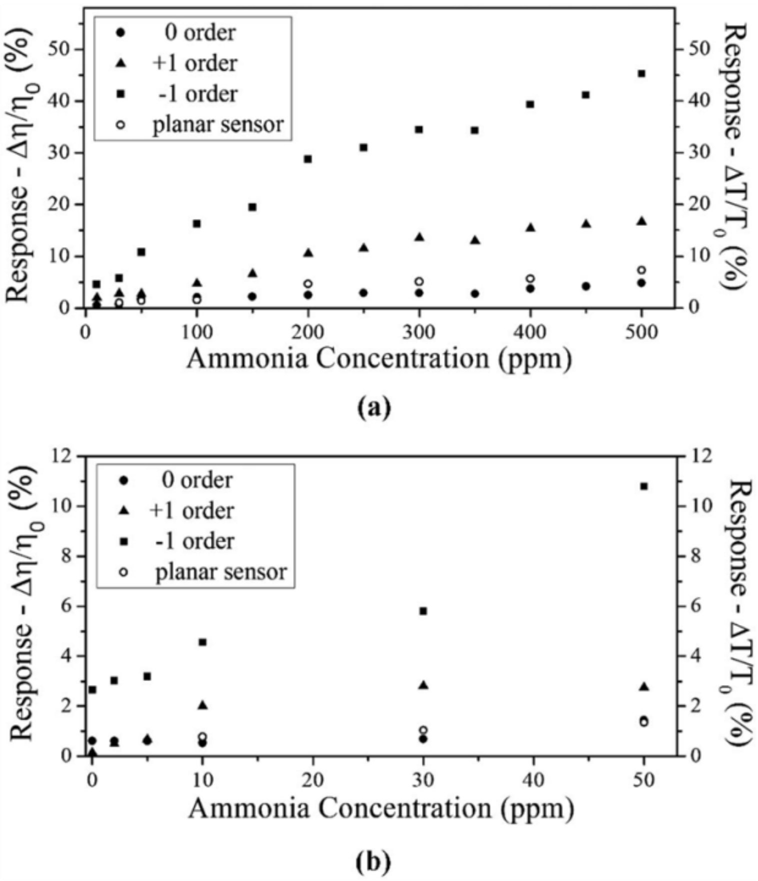

Figure 4-6: Response of the diffraction grating sensor to various ammonia concentrations of zero order and ±1 order. The response of the unprocessed planar sensor is shown in the same figure for comparison. (a) Overall response and (b) low ammonia level response is shown.

The difference between the +1 and −1 order responsivity is attributed to the exact geometry of the diffraction grating combined with the asymmetric readout. It should also be noted here that the ammonia sensor shows a small but traceable response to humidity (0 ppm of ammonia in Figure 4-6).

The sensor behavior has been verified by applying rigorous coupled-wave analysis using the typical characteristics of the diffractive element and the experimental geometry used. The analysis indicates that a composite refractive index value n~1.57 agrees well with the observed behavior and provides an estimate of refractive index change $\Delta n/\Delta C \sim 10^{-5}$ ppm^{-1}. The ±1 order response also exhibits a high signal-to-noise ratio (SNR), defined as the ratio of the diffraction efficiency change over the standard deviation of the signal. SNR for the +1 order is 18.6, as opposed to 3.5 found for the zero order. In Fig. 4-6(b) the low concentration section is presented. It clearly records the lowest detectable value at 2 ppm. It is important to underline here that this is a direct measurement process and does not involve any lock-in detection or other mathematical estimation methods.

4.3 Multilayer metal/metal-oxide diffraction gratings for photonic temperature sensing

In this work, multi-layered Pt/SnO_x diffractive structures have been designed by applying matrix methods and rigorous coupled wave analysis (RCWA)[5]. An optimum performance at λ=633nm is sought assuming nominal refractive index values. The tin oxide refractive index value was set as $n_{(SnOx)}$ ~2 and zero extinction was considered , while the complex refractive index values of Pt for wavelengths around 633 nm were taken from [5]. The primary assumptions ignore possible material modification by non-stoichiometric growth or metal in-diffusion at the metal-oxide interfaces that would lead to variable structural properties.

In the design, only variations in the real part of the refractive index, $n_{(SnOx)}$, of the tin oxide layers were considered. The most promising multilayer structure design outlined in figure 4-7 comprises a series of alternating metal and oxide layers grown on silica, denoted by: SiO_2/Pt/SnO_x/Pt/SnO_x/Pt corresponding to: semi-infinite silica/100nm/170nm/5nm/170nm/5nm. A schematic of the multilayer grating shape is shown in figure 4-8. The fabricated diffractive element has a period of 4μm. An interrogating laser beam is incident on the structure from the left and the relevant diffracted light beams are indicated by referring to R_m and T_m (m=0, ±1, ±2, ±3…) parameters denoting the m_{th}-diffraction order intensity reflection and transmission coefficients respectively.

---

[5] All theoretical calculations were performed by Prof. M. Sigalas, whose contribution is acknowledged.

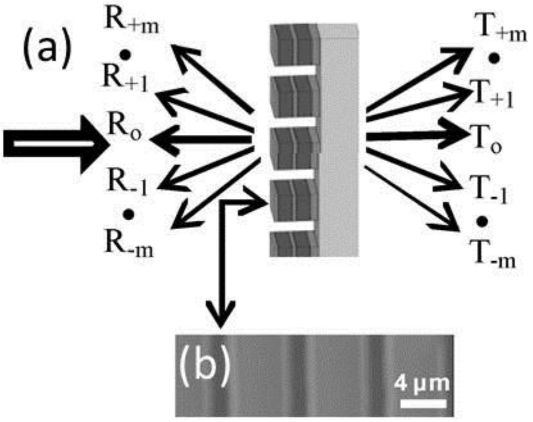

Figure 4-7: (a) Schematic outline of structure design and the interrogation concept. (b) Scanning electron micrograph of a segment of the multilayer diffractive element.

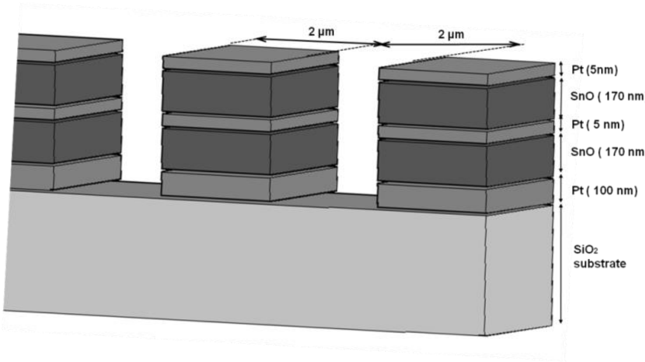

Figure 4-8: Schematic of the grating structure used in the current work

A typical grating profile is shown in figure 4-9, as measured with a Tencor profilemeter Alpha Step.

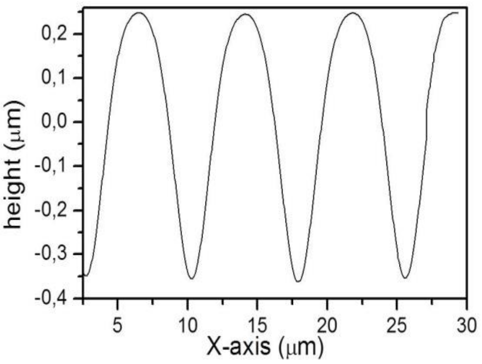

Figure 4-9: Typical grating profile of fabricated multilayer diffraction gratings. The Alphastep stylus dimensions are large compared to actual grating dimensions, thus the profile does not appear rectangular

Figure 4-10 depicts the calculated zero-order transmission (T_0) together with the zero (R_0) and first order (R_{+1}) reflection at 633nm as a function of the typically anticipated SnO_x refractive index. RCWA is applied for the actual experimental conditions. A nearly zero R_0 value is reached at $n_{(SnOx)}$ =2.2. Similarly the first order reflection, R_{+1}, attains also a minimum of ~0.3% at $n_{(SnOx)}$ =2.1. On the other hand T_0 increases with $n_{(SnOx)}$ from 12% to 20%. The present analysis shows that the nominal $n_{(SnOx)}$=2.0 offers a relatively large R and T sensitivity for refractive index variations and it was chosen for the calculations.

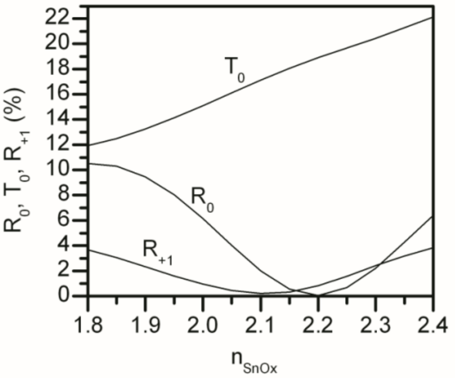

Figure 4-10: Theoretical behaviour of the T_0, R_0 and R_{+1} at 633 nm wavelength as a function of the refractive index, $n_{(SnOx)}$, of the non-stoichiometric tin oxide.

The concept of photonic temperature sensing by use of multilayer grating has been evolved and designed by our group, whereas the representative structure has been fabricated at the Institute of Electron Technology (IET) Warsaw, Poland, by growing the structure $SiO_2/Pt/SnO_x/Pt/SnO_x/Pt:SiO_2/100/170/5/170/5$ (all values in nm)[6]. Pt layers were deposited by DC sputtering using a metallic target. Tin oxide (SnO_x) layers were also grown by reactive DC sputtering from a solid Sn metal target in O_2/Ar plasma. Following multilayer deposition, the structures were patterned by photolithography and etched by inert Ar^+ ion etching to form a 4 μm period surface relief diffractive gratings. The deposition conditions have been tuned to achieve non-stoichiometric growth of the tin oxide in order to take advantage of the refractive index variability produced by structural imperfections. A series of previous experiments analysed conditions for growing non-stoichiometric mixed polycrystalline/amorphous structure. Oxygen partial pressure was kept at $\sim 2 \times 10^{-3}$ mbar, while sputtering power was at 75 W. Off-line ellipsometric measurements have been performed and used for process calibration. Optical lithography and inert argon sputter-etching has been applied to avoid any material contamination induced by reactive gas. The grating has been etched to the full structure depth with a good etch aspect ratio, to form the final device as depicted in the scanning electron micrograph of figure 4-7. A certain variation in the originally designed 50% duty cycle is apparent owing to the nature of the sputter-etching process.

4.3.1. Experimental Issues

The effects of the refractive index of the oxide structure have been explored by varying the temperature (Θ^oC) to alter the diffraction conditions. The refractive index variation is thus immediately translated to the optical R and T parametric changes observed by implementing the interrogation concept of figure 4-7. To evaluate the temperature sensitivity experimentally, the structure was placed in a thermoelectrically controlled miniature open cage. A type-K thermocouple was thermally coupled with the aid of thermal adhesive paste close to the grating structure

---

[6] The contribution of Dr. Anya Piotrowska and Dr. Eliana Kaminska in IET, Warsaw, Poland is highly acknowledged

and is used to reference the temperature. A systematic error of the measured temperature may be expected here due to heat conduction. A HeNe laser emitting 5mW at λ=633nm is used and various diffracted orders were monitored in parallel by using four power meter heads (Newport model 2832-C Dual Channel) connected to LabView® data acquisition system. The laser beam incidence angle was set at 19.4° to the normal in order to facilitate convenient positioning of the apparatus used. A reference beam was always simultaneously recorded to compensate for laser power variations. A systematic deviation is arising, however, due to temporal lag of the thermocouple response in continuous recordings.

The experimental setup is shown in figure 4-11.

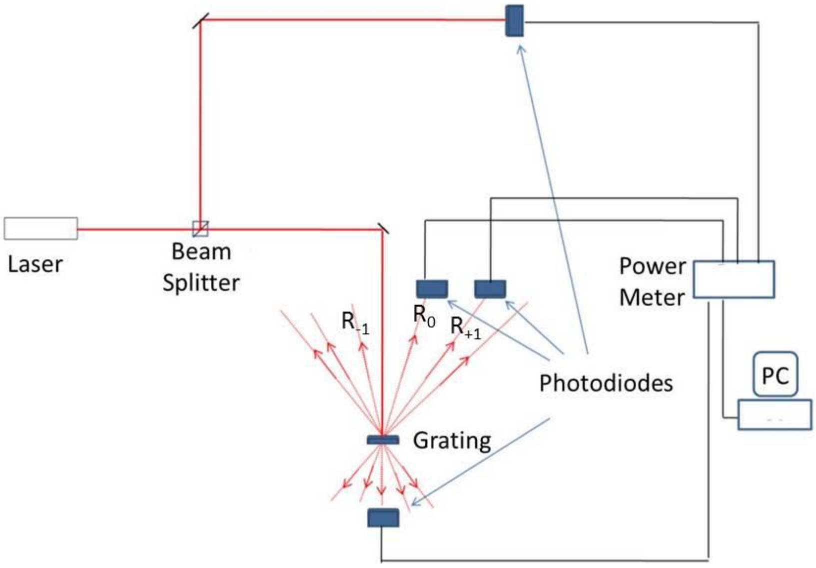

Figure 4-11: Experimental setup for the concurrent measurement of the diffracted power in several different orders. All measurements are automatically edited by PC software.

Simultaneous real time monitoring was performed for R_0, T_0 and R_{+1} for ascending and descending temperature cycles between 20°C and 60°C, as depicted in figure 4-12.

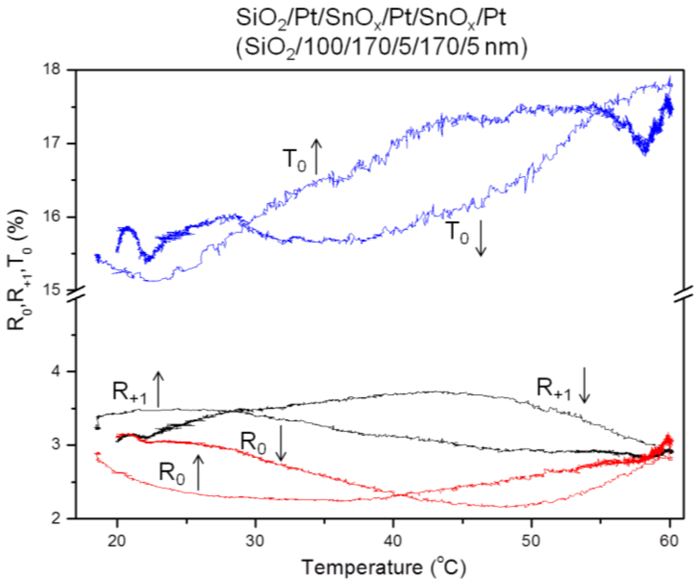

Figure 4-12: Experimental behavior of three important parameters R_0, T_0 and R_{+1} for ascending (↑) and descending (↓) temperatures Θ°C. The overall behavior shows a good agreement with theory, although it does not match exactly.

A considerable dependence of R_0, T_0 and R_{+1} on temperature is recorded, while a similar behaviour was also observed for the higher diffraction orders both in transmission and reflection. While the design refractive index of n_{SnOx}=2.0 is used for maximum reflection sensitivity, temperature cycling provides a real estimate of T_0, R_0, and R_{+1} by comparing theory (Figure 4-10) and experiments (Figure 4-12). A best fit is thus obtained for $n_{(SnOx)}$ between 2.10 and 2.35, proved by the existence of reflectance minima in the temperature range of 40°C-50°C and the appearance of two nodes between the R_0 and R_{+1}, in full agreement with the theoretical prediction. By comparison with theory, these latter nodes correspond to the values n_{SnOx}~2.17 and n_{SnOx}~2.32 attained respectively at Θ~23°C and Θ~60°C. A certain hysteresis in the response is observed leading to an open loop in the ascending trace, which may be justified by a certain lag of the reference thermocouple recording and heat diffusion through the metal cage. The transmission T_0 values and time recordings also agree very well with the theoretical prediction at a less than 10% difference. In fact, optical monitoring shall be considered here to provide absolute measurements with the observed difference being an erroneous effect due to the thermocouple probe physical contact. In all cases the behaviour reflects the considerable temperature sensitivity of the diffractive device. The refractive index $n_{(SnOx)}$ of the grown oxide is found considerably higher that the nominal crystalline value. This is justified by material imperfection and possible metal in-diffusion affecting nanocomposition, and thus some effects of absorption cannot be excluded.

Considering the temperature variation, $\Delta\Theta^{o}C$, the sensitivity, S, of the potential reflective sensor device may be defined as the variation of the diffraction efficiency per ^{o}C(Eq. 4-2)

$S_{R+1}=\Delta R_{+1}/(\Delta\Theta\cdot R_{+1})$ [4.2]

Fitting the linear sections of the recording curves, provides an estimate of $S\sim(0.0262\pm2.96\times10^{-4})^{o}C^{-1}$ or ~2.62%/°C. A zero-order reflected beam is found for R_0: $S_{R0}\sim(0.02587\pm3.81\times10^{-4})\ ^{o}C^{-1}$. This reflectance sensitivity is a x 4.5 improvement as compared to the zinc-based etalon scheme [6]. Furthermore, the zero-order transmitted beam T_0 gives: $S_{T0}\sim(0.1\pm1.6\times10^{-3})\ ^{o}C^{-1}$ thus indicating that the transmission mode may be preferable in our case. This latter preference for transmission monitoring is solely due to our original assumption. The use of the estimated values of $n_{(SnOx)}=2.10–2.32$ for the range $\Theta\sim20^{o}C-60^{o}C$ will lead to an optimal device. It is emphasized here that the experimentally observed and theoretically analysed behaviour is solely attributed to the thermally induced refractive, and possibly additional absorptive changes, rather than thermal expansion effects which have a negligible impact.

In addition to the sample used before, many other samples were tested for their performance as potential temperature sensors. A concise table of all samples tested as well as their sensing performance can be found in the APPENDIX 2.

4.4 Laser-structured POF in photonic sensing of ammonia and water vapors

The performance of structured POF as photonic sensor devices was also demonstrated. Three processed POF exhibiting losses of 0.92 dB, 1.64 dB and 4.7 dB respectively, were coated with polystyrene sulfonate-b-*tert*-butylstyrene diblock copolymer sensitive to NH_3 vapor and were tested under controlled conditions. Details on the material synthesis, characterization and its sensing capabilities have been published elsewhere [7, 8]. The sensing material filled the structured cavities. Upon exposure to ammonia the effect on refractive index is translated into alteration of propagation loss which is detected. The sensor test results are shown graphically in figure 4-13. The sample with the highest losses sample A at 4.7 dB (red line) proved to be more sensitive, exhibiting higher sensing response by a factor of eight as compared with the samples of lower loss i.e. sample B at 1.64 dB-black line and C at 0.92 dB-blue line).

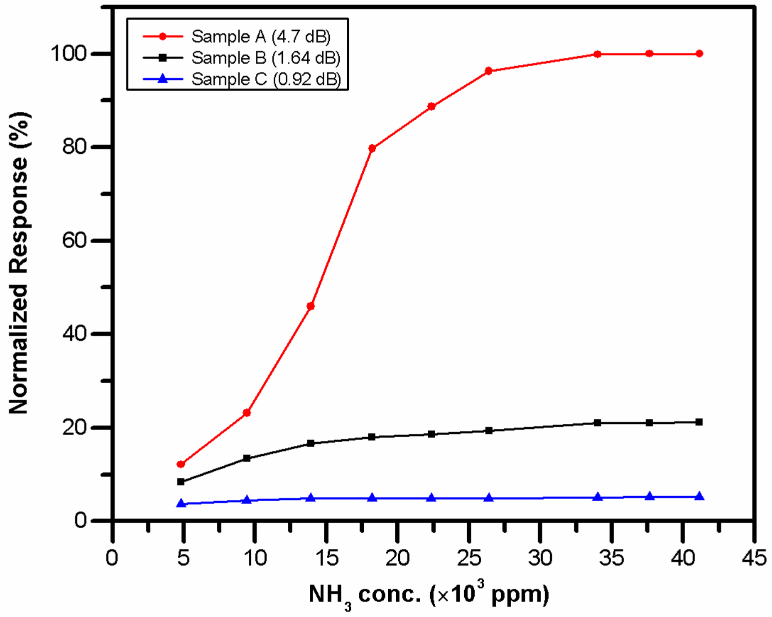

Figure 4-13: Three fibers of various losses and their performance as ammonia sensors.

In order to evaluate POF samples as potential humidity sensors a humidity sensing material based on Cobalt Chloride ($CoCl_2$) / tetramethoxyorthosilicate (TMOS) composite was employed. It was prepared with deionized water, HCl and isopropanol in order to obtain a 15% w/v solution to coat the structured fibers. The created microcavities were filled with the sensitive material and humidity absorption resulted in refractive index alterations causing propagation loss changes, which are detected. For the purposes of the present study transverse and longitudinal structures were created on the fiber surface, as shown in the inset of figure 4-14. The response can be defined as shown in Eq. 4-3:

$$\text{Response} = \frac{I_{SIG} - I_0}{I_o} \times 100\% \quad [4.3]$$

where I_{SIG} is the intensity measured in the presence of humidity and I_0 is the optical intensity measured in the absence of humidity, i.e. after applying nitrogen in the sample.

The sample having a longer transverse groove (shown in black) performs better as compared to the shorter one (shown in red) for the same humidity values. This can be attributed to the higher number of propagation modes that are affected. The same behavior is followed in the case of longitudinal groove samples (shown in green and blue, respectively).

Moreover, on comparing samples of almost the same ablation length for transverse and longitudinal section regimes (black and blue lines, respectively), it appears that the transverse section has a significant effect on sample sensitivity. This can be attributed to the fact that the propagation modes that carry more energy interact with the sensitive material in the POF – material interface.

The observed response for various fiber structures is depicted in figure 4-14.

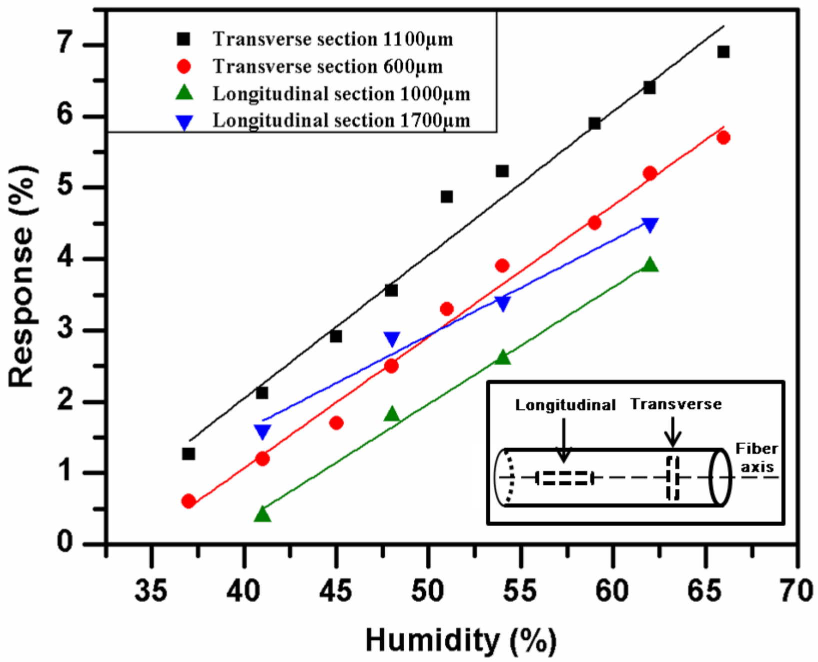

Figure 4-14: Effect of cross and longitudinal sections of POF samples regarding their sensing performance upon humidity exposure, and the illustrative schematic of longitudinal and transverse grooves on POF surface (inset).

Even though no measurements were taken for humidity values below 37% , it should be noted that the response could be even negative for those humidity values. This can be explained because I_0 is taken as reference value for typical room humidity (about 35%). Thus for values below that, the response can be negative.

4.5 Concluding remarks

Diffractive $NiCl_2$ /SiO_2 nanocomposite photonic sensors for ammonia have been demonstrated. The device has been fabricated on a thin-film structure using direct UV laser microetching techniques. The diffractive optic sensor has been tested. The first-order diffracted beams are found to provide an appreciable sensor response which allowed the detection of quite low, 2 ppm, ammonia levels. In addition, a novel layered nanocomposite diffractive device was designed, fabricated and studied. Its temperature sensitive behavior was found to be in excellent agreement with its theoretical performance estimated by rigorous coupled wave analysis. The produced device functions with a high temperature sensitivity of ~10% per ^{o}C.

A detailed study on POF material interaction with ArF excimer laser was performed which revealed interesting results. Laser parameters, such as fluence, power, and repetition rate were evaluated for their effect on ablation characteristics. The difference in fluorinated polymer, i.e. cladding material, and pure PMMA, i.e. the core material, upon laser illumination was investigated and commented. A plethora of images revealed the threshold where the cladding is ejected from the core. All results will be further evaluated in order to optimize the ablation process in POF. The final objective is the use of optimized laser modified POF tips as potential photonic sensors with the aid of organic, inorganic or hybrid material sensitive to various agents.

4.6 References

1. Meristoudi A. et al, J. Opt. A: Pure Appl. Opt. 11, 034005 (2009)

2. Tsigara A.et al, Sensors and Actuators B, 120, 481 (2007)

3. Lukowiak A. and Strek W., J. Sol-Gel Sci. Technol. 50, 201 (2009)

4. Vainos N. A., Mailis S., Pissadakis S., Boutsikaris L., Parmiter P. J. M., Dainty P. and Hall T. J., Appl. Opt. 35, 6304 (1996)

5. Palik E. D., "Handbook of optical constants of solids", Academic Press, San Diego(1998)

6. Vainos N. A., Tsigara A., Manasis J., Giannoudakos A., Mousdis G., Vakakis N., Kompitsas M., Klini A., and Roubani-Kalantzopoulou F., Appl. Phys A 79, 1395 (2004)

7. Athanasekos L., Pispas S. and Riziotis C., Proc. SPIE 8426, 842615(2012)

8. Athanasekos L., El Sachat A., Pispas S., and Riziotis C., J. Polym. Sci. B Polym. Phys. 52,46,(2014)

5. Microfabrication and material manipulation by laser radiation forces

5.1 Introduction

The creation of polymer condensates and micro-/nanostructures implemented in various forms is discussed, including formations in bulk solution, thin films, free space and finally the drawing of fibers, each requiring experimental procedures and results in structures of different shapes and characteristics.

Laser radiation forces applied in fully transparent, highly-entangled semi-dilute polymer solutions generate free-standing, three dimensional, micro- and, potentially, nano-solids. The underlying phenomena are attributed to a synergy of effects involving the radiation forces exerted by milliwatt laser beams on polymer chains and the entanglement of macromolecules. Most importantly, since the primary stages of formation, the incident optical field is structured and guided by the induced microstructures. This self-confinement enhances the effect and results in great compression of the material, osmotic solvent extraction and, eventually, materials solidification in free space. Structural reversibility verifies the absence of any chemical modification of the material. These innovative concepts result in the fabrication of microstructures, including among others plasmonic and fluorescent semiconductor quantum–dot hybrid structures, as well as polymer fibres also drawn by laser radiation forces.

Optical radiation exerts forces on matter and leads to the remarkable effects of optical trapping and organization pointing to applications in materials, information technology and biomedical sciences. Originating from the concept of optical trapping on the microscale, current advances in assembly by laser induced soft- matter organization are highlighted. These emerging concepts provide alternative tools for micro and potentially nano-fabrication and offer a new platform for fundamental investigations and new applications in photonics. Earlier investigations in this field [1, 2] had shown outstanding results concerning the organization of entangled soft matter upon illumination by a laser beam. These effects in liquid phase could not be fully explained at that stage. In detail, the phenomenon could not be attributed to photothermal effects, because the flow direction of the solute is governed by the thermodiffusion coefficient sign, to wit, in our case (PI) is positive, resulting in the motion of the solute to colder regions, thus not along the beam axis. This is in contrast to the observed phenomenon. What is more, neither chemical modification was apparent, upon measuring the molecular weight distribution of the created structures. By applying shorter wavelength irradiation, near UV, the effect was found to be weaker, despite the strong absorption of the polymers used in that region. Thus, the phenomenon excludes also multiphoton absorption effects.

Initial studies revealed interesting results, upon focusing visible laser irradiation on polymer solutions, as shown in figure 5-1, where the polymer fiber-like structures are visible.

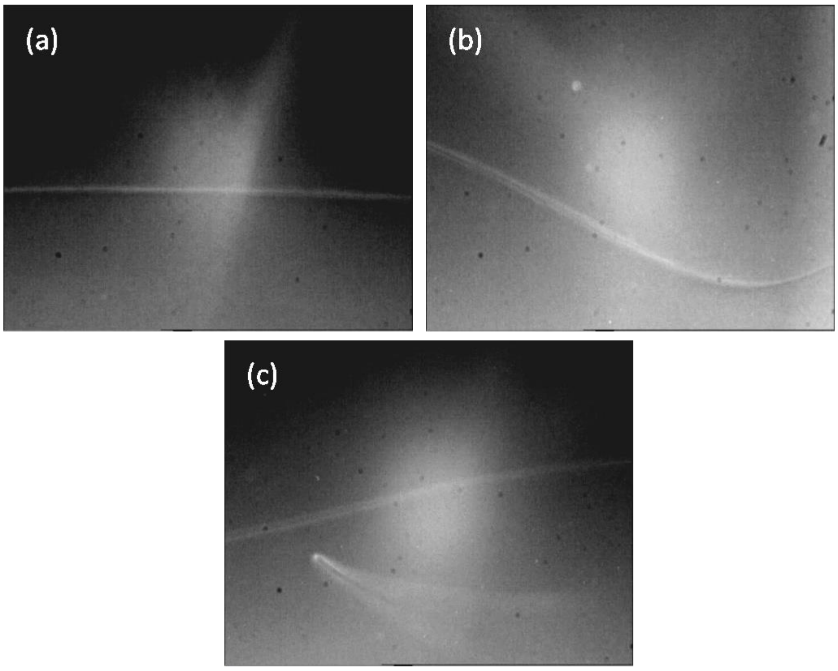

Figure 5-1: Initial stage results of phenomenon. Fiber-like structures are visible in polymer solution after illumination with a focused laser source.

Later attempts investigated the formation of optical spatial solitons [3] and the effect of prolonged irradiation in the structure formation in polydiene solutions [4].

5.2 Theoretical background and calculations

5.2.1 The origin of radiation forces

Although radiation pressure forces stem directly from Maxwell's equation solutions for electric field [5], it was many years later when a targeted attempt to handle and apply those forces on matter was reported by Ashkin [6]. In particular, the manipulation and trapping of particles by light radiation forces was first proposed by Ashkin [6]. Since then, a significant work on the field has been done, evolving the concept of matter organization with the aid of optical tools [7, 8, 9].

Once the beam propagating in a transparent medium faces an "obstacle", e.g. a polymer micelle or a metal nanoparticle in a solution, it is scattered and changes direction (Figure 5-2). Such a change gives rise to a momentum transfer from the beam to the obstacle. Considering the photon approximation for the light beam, it is obvious that the momentum of each photon is transferred to the object. According to Newton's second law, we get:

$$F = \frac{\Delta p}{\Delta t} \qquad [5.1]$$

that is the rate of momentum change, associated with a change in momentum flux of the beam. It is understood, however, that if the particle is not on the beam propagation axis, i.e. it is convergent or divergent, the momentum flux will be decreased.

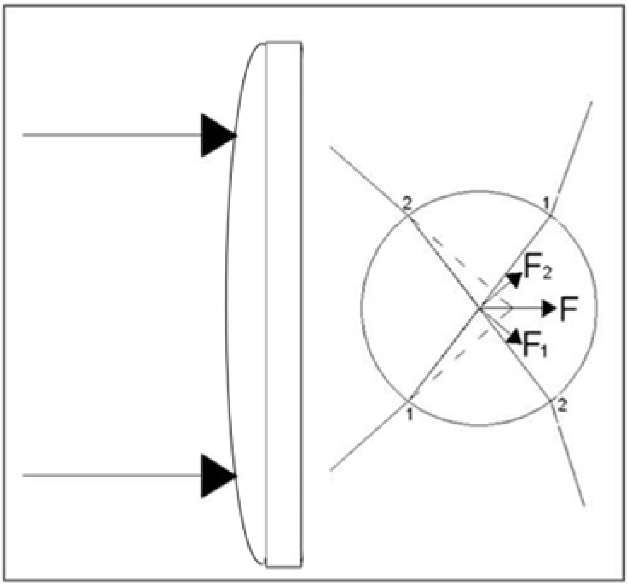

Figure 5-2: Schematic representation of optical forces applied in a transparent medium due to refraction

Depending on the relative size of the particle as compared to the interacting wavelength this light-matter interaction can be approached in two regimes. First, in the Rayleigh regime particle size is much smaller than the wavelength of incident light. In that case, the particle acts as a simple point dipole and the radiation force can be divided in two components: (a) the *scattering force*, associated with the momentum change of the electromagnetic wave due to the scattering by the dipole and (b) the *gradient force* associated with the Lorentz force acting on the dipole. Second, the Lorentz- Mie regime where the size of the particle far exceeds the laser wavelength [10].

Let us consider a particle in a solution that lies in the Rayleigh regime. In this approximation, the scattering and gradient force components are readily separated. As the electric field oscillates harmonically, so does the electric dipole, radiating secondary waves in all directions. Thus, energy flows and the induced scattering force is applied on the dipole, along the light propagation axis. The resulting scattering force holds as [11, 12]:

$$F_{sc} \approx a|E|^2 \quad [5.2]$$

with α being the polarizability of the particle.

In order to evaluate both the scattering and the gradient forces, the polarizability of the dielectric particle needs to be determined. The polarisability can be defined as the ratio of the dipole moment to the applied field. In the case of dielectric particles the local polarizability originates mainly from bound electrons. Through the Clausius-Mossotti procedure, it can be shown [11] that:

$$a = \frac{8\pi n_{sol} k^4 r_{sph}{}^6}{c}\left(\frac{m^2-1}{m^2+2}\right) \quad [5.3]$$

where n_{sol} is solution/medium refractive index, r_{sph} is the microsphere radius, m is the relative refractive index $m = \frac{n_{sph}}{n_{sol}}$ and n_{sph} is the microsphere refractive index,.

The gradient force stems from the electromagnetic field Lorentz force acting on the dipole. It causes the particle to be attracted by high intensity parts of the field, i.e. in the focal region, depends on the gradient of intensity of the incident beam and acts in the direction of the field spatial gradient. The gradient force, being proportional to particle polarizability and the optical intensity gradient, can be expressed [11, 12] as:

$$F_{grad} \sim a \cdot \nabla |E|^2 \quad [5.4]$$

In an attempt to investigate the radiation pressure effects on a particle surrounded by a solution, thermal forces have to be taken into account. The irradiating beam causes a temperature gradient in the medium surrounding the particle, due to absorption. This, in turn, results in a thermal force and motion of the particle, called photophoresis [13]. In order to minimize or even eliminate such effects, both medium and particles should be transparent to the incident light. Such is the case using transparent polymer solutions.

In practice, however, the particles move freely in a random manner inside the solution, due to thermal fluctuations and Brownian motion. The thermal energy is given by $k_B T$. The gradient force is the gradient of the so-called trapping potential, which is given by [12]:

$$U \approx -a \cdot |E|^2 \qquad [5.5]$$

If the trapping potential exceeds the thermal kinetic energy, the particles are governed solely by the gradient force. Under these circumstances, the radiation force of the laser beam affects the motion of the particles pulling them into the higher intensity region of the beam, while scattering forces are pushing them along the beam propagation direction.

In the case of irradiating a relatively large sphere having radius of the order of microns, its optical behavior becomes more complex and it can no longer be described by a simple dipole model, but it requires generalization which includes multipole effects. This is achieved within the Lorentz-Mie scattering theory [14] applied appropriately in order to obtain more accurate and generically valid results.

5.2.2 Polymer solution dynamics

In a real polymer network of long linear chains, there are a number of topological constraints imposed, due to their inability to cross through one another, commonly known as entanglements. Assume a polymer solution in a good solvent. At low concentrations, the polymer can be considered as isolated coils dynamically positioned very far from each other. As the concentration increases, it reaches a special concentration value, called overlap concentration c*, that equals the concentration inside the coil. Above the overlap concentration, the chains interpenetrate and the solution enters the so-called semidilute regime. In this regime and at small distances, each monomer is surrounded mostly by solvent and the distance between two monomers is quite large (figure 5-3).

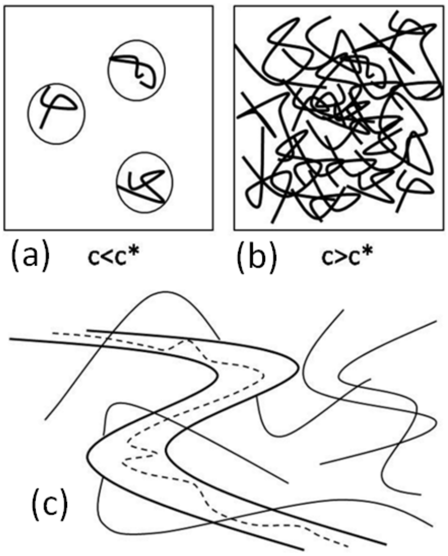

Figure 5-3: Schematic of dilute (a) and semidilute (b) solution regimes. (c) Each polymer is constrained to move within a topological tube due to the presence of the confining surrounding polymers. Within this tube the polymer performs a snake-like motion in the polymer melt.

Here we can introduce the correlation length ξ being the average distance between segments on neighboring chains and is independent of the degree of polymerization.

In general, the Edwards tube concept of macromolecular motion is considered to be a rather difficult many-body problem [15]. Pierre-Gilles de Gennes succeeded in reducing this many-body problem to the motion of a single chain as it is confined in a tube formed by the surrounding chains (figure 5-4).

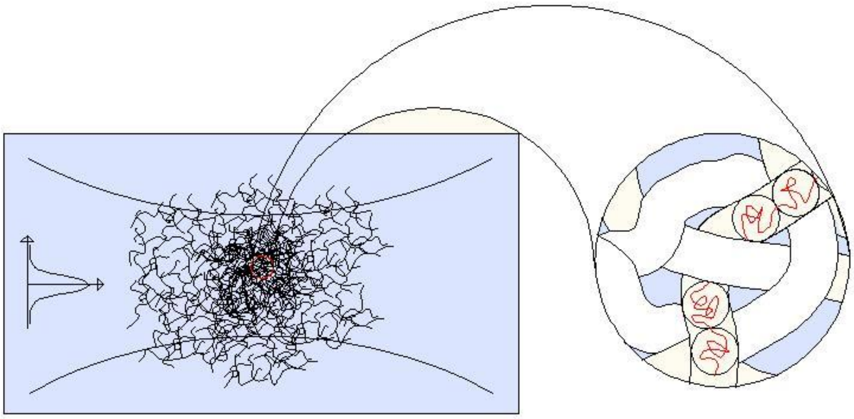

Figure 5-4: conceptual view of polymer mesh in the focal point of laser (left) and “blobs” forming entangled “tube” in solution (right)

The simplest tube model was proposed by de Gennes [16] for the motion of linear entangled polymers, called the reptation model. That model was introduced to explain the dependence of the mobility of a macromolecule on its length. According to the model, the polymer chains are reptating through tubes whose formation and shape is dictated by the neighboring chains and their entanglement points.

5.2.3 Estimations of radiation forces

In order to ensure that radiation forces are capable of organizing the polymer chains to create structures, a feasibility study is necessary. Let us consider a semidilute polyisoprene solution of molecular weight M_w=1.500 Kg/mol in n-heptane at 40%wt which exhibits concentration of c=0.3 gr/cm^3 which is much greater than the overlap concentration c*~0.008 gr/cm^3, indicating a semidilute solution at a high degree of entanglement. In that case, the refractive index of the pure polymer (n_{pol}= 1.52) is higher than the refractive index of the solvent (n_{solv}=1.388). As a laser beam of relatively large numerical aperture and intensity is incident on a polymer solution, two types of forces act concurrently, namely the scattering and the gradient force, defined previously, giving the resultant optical force that interacts with the semidilute polymer solution. Given M_e the length of macromolecule between adjacent entanglements, a number of $z = \frac{M_w}{M_e}$ of about 259 tangles per polymer chain are expected with $N_e = \frac{M_e}{m_{mono}} \simeq 85$ monomers per entanglement. We may thus define here a parameter describing the chain segment between adjacent nodes as a "suprablob". The suprablob can be heuristically considered as a spherical nanoparticle composed of a chain section between tangles. It is surrounded by solvent and has a density and refractive index which ranges in between the values of melt and solution average. In analogy to the blob parameter, a diameter of $D \sim (2N_e/c)^{1/3}$ ~7 nm, with c being the concentration may be estimated for the given concentration (figure 5-4). The resultant polarizability is thus estimated in the range of $\alpha = 6 \cdot 10^{-37}$ $F \cdot m^2$ and thus, the gradient force F_{gr} can be estimated at about: $F_{gr} \sim$ 2-3 $\cdot 10^{-18}$ N on each suprablob particle. We note, though, that due to the strong connectivity and high degree of entanglement, the forces are summed as depicted in figure 5-5, giving a total force acting on the polymer mesh. This total gradient force far exceeds the Brownian motion force ($F_B \sim 10^{-29}$ N), and thus leads to the evolution of the phenomenon.

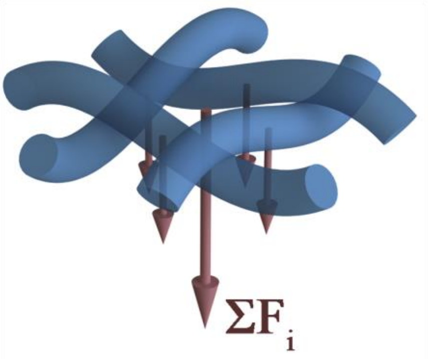

Figure 5-5: radiation forces applied on tube segments leading to local resultant forces ΣF_i

As previously mentioned, the gradient forces compel the particles to reconfigure their spatial distribution leading to an organized spatial variation of a refractive index in the solution. This effect is greatly assisted here by the connectivity. By these means, the first condensate is created at the focal point of the objective. Due to its transparency and slightly different refractive index from the surrounding medium it produces Mie scattering. Several Mie scattering configurations are simulated in figure 5-6 to strengthen this perspective[7]. It becomes apparent that since the initial stages of formation strong forward and backward field is produced which enhances further the applied forces and leads to attraction of soft matter.

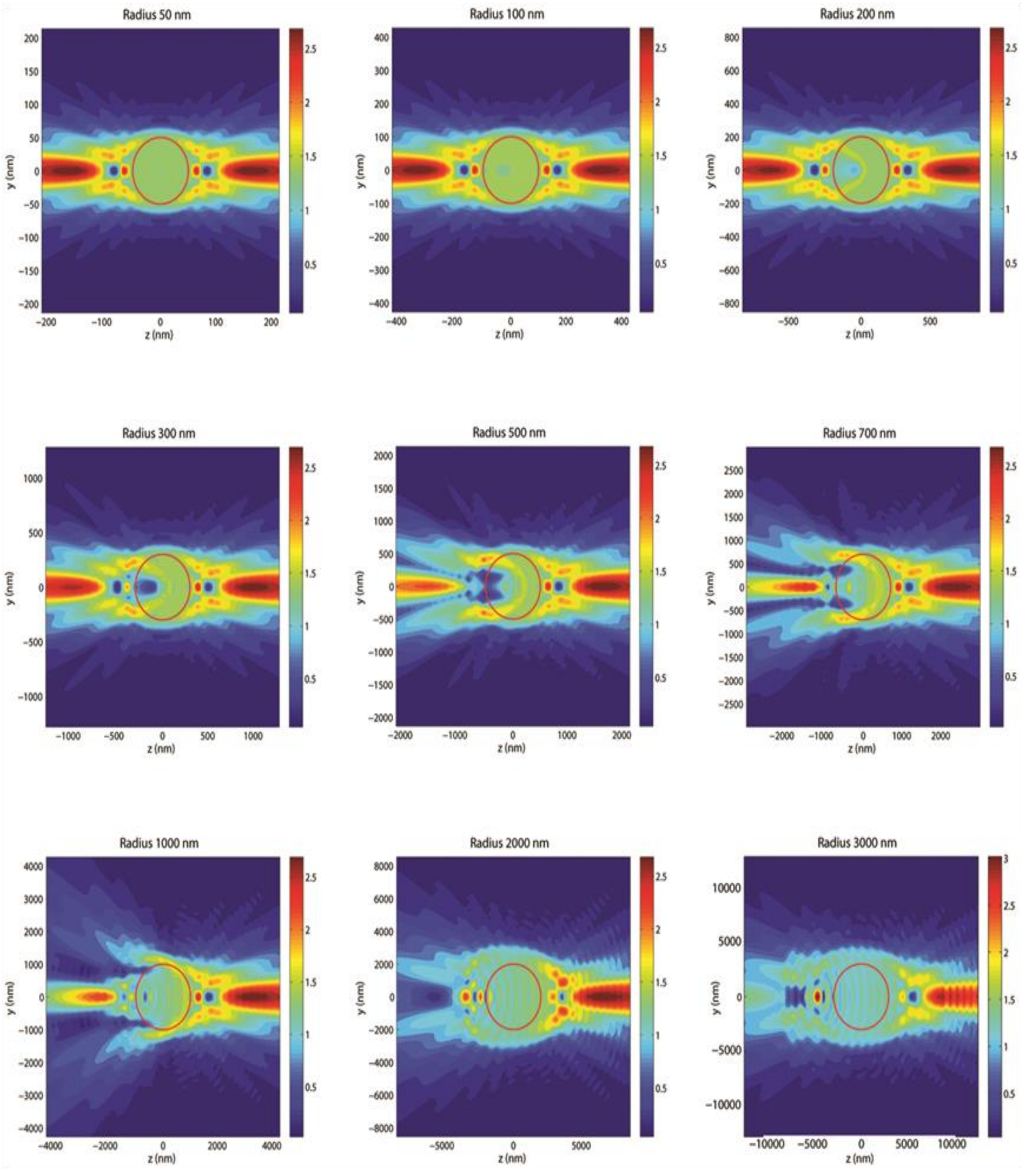

Figure 5-6: Simulation of Mie scattering (by uniform spherical polymeric condensates). Light intensity {I(r)} distribution of field scattered by spheres of various radii. The incident plane wave has I=1, is right circularly polarized at wavelength λ=671nm and propagates from the left to right towards the +z-direction. The pseudochrome scale is absolute with respect to unity. Simulation by electromagnetic Mie Scattering methods.

---

[7] Mie scattering simulations were performed by Prof. Yiannopapas whose contribution is acknowledged

In weak focusing conditions an array of microspherical regions, condensates, is formed in the liquid phase since the induced microlens refocuses the incoming light in a neighboring region as depicted in figure 5-7 and observed experimentally [1].

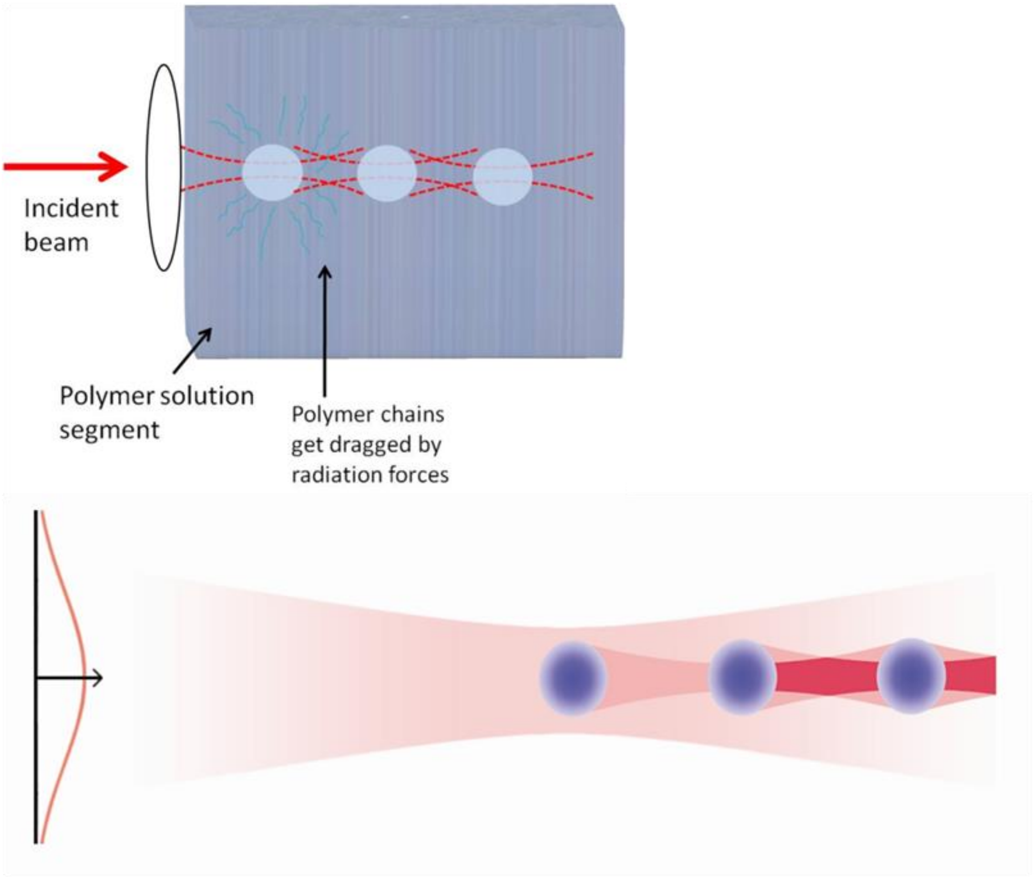

Figure 5-7: Schematic representation of the structure creation process in the polymer material

Each of the induced microlenses act to refocus the incident field at consecutive positions along the incident beam propagation direction, with a result of the simultaneous buildup of the array. Considering the gradient forces, the members of this array should be located at local minima of the trapping potential, or otherwise at the foci of the formed beam. Upon prolonged exposure this may result in the gradual buildup of the fiber-like microstructures. Furthermore under strong focusing conditions, the Mie scattered field and the consequent high field produces strong condensation at the focal point and a fast (in the order of seconds) attraction of matter to create microstructures as schematically shown in figures 5-8 & 5-9.

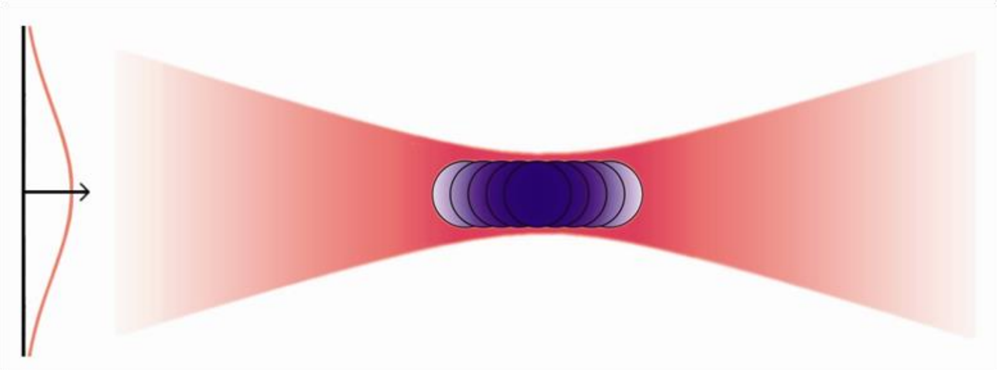

Figure 5-8: strongly focusing regime in which a continuous solid structure is produced commencing from forward and backward scattering fields in the nanoscale

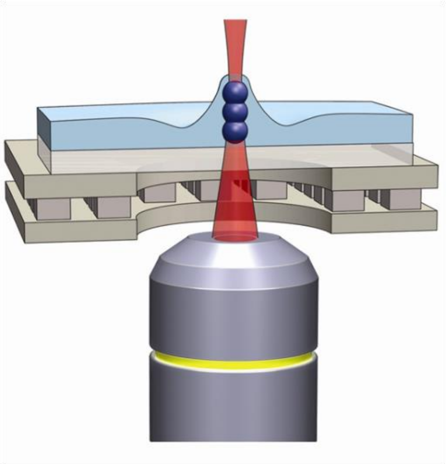

Figure 5-9: Schematic detail of the experimental configuration illustrating the creation of a solid microstructure emerging from films of semidilute polymer deposited on glass. Material is pulled from the vicinity leaving behind a visible recess

5.3 Experimental results

5.3.1 Material densification in bulk solutions

A focused Gaussian beam of 671nm wavelength is propagating in a semidilute polymer solution as depicted in the experimental configuration of figure 5-10. In the experimental arrangement, the cuvette containing the semidilute polymer solution is placed on a translation stage to facilitate positioning. The process is monitored in real time by a CCD camera and the profile of the laser beam is monitored on a screen. An image of the real experimental setup is shown in figure 5-11.

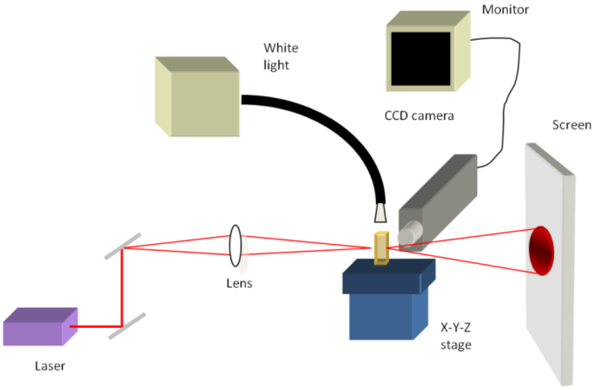

Figure 5-10: Experimental setup for structure creation in cuvette. The beam profile is projected on a screen.

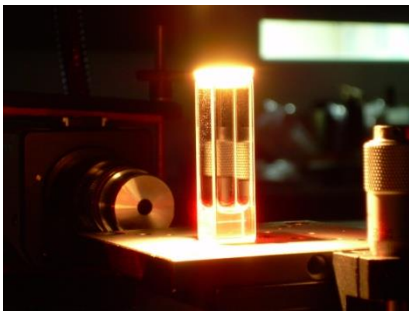

Figure 5-11: The experimental setup comprised a cuvette where the laser beam is passing through the solution and a CCD camera is attached perpendicular for real time monitoring.

The laser beam was allowed to pass through the PI polymer solution (figure 5-12a) and recorded by the CCD camera. After a few seconds, a scattering effect was noticed, evidencing the presence of a created structure along the beam (figure 5-12b).

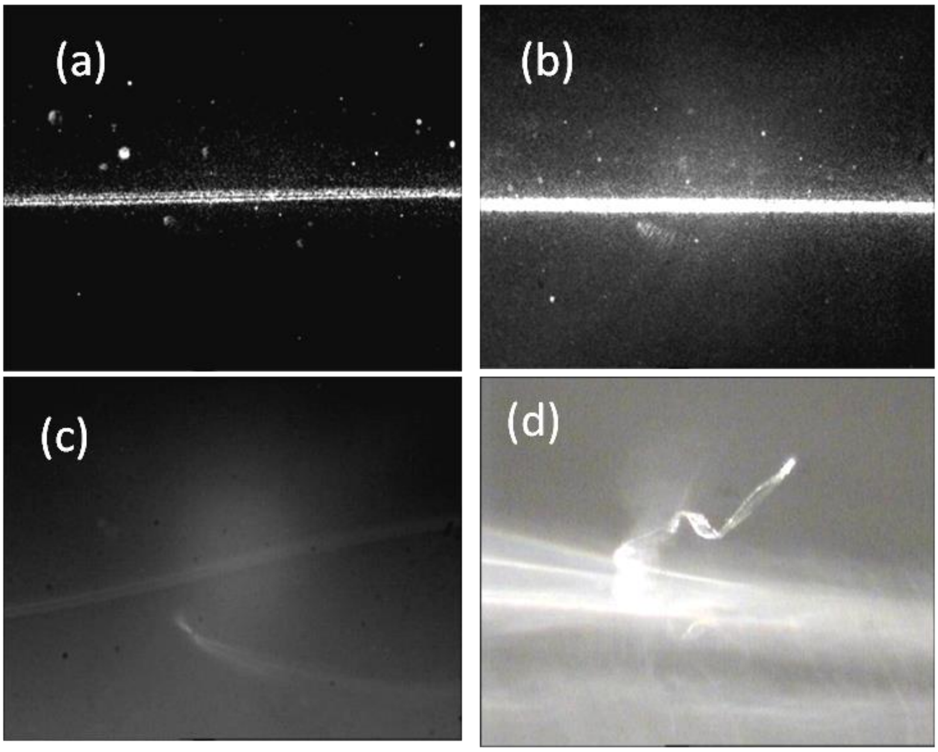

Figure 5-12: (a) the laser beam passes through the polymer solution. (b) The laser beam is waveguided by the formatted structure. (c) Two structures written on the same solution at perpendicular directions. (d) floating-like microstructure as shown in a CCD camera image

The writing was performed in a cuvette which contained the polymer solution. After the first writing attempt was finalized, the cuvette was turned at 90 degrees and a second writing was attempted. This resulted in two perpendicular structures as shown in figure 5-12c. The first is shown along the image and the second has its tip, where the light is escaping. In another attempt, a structure was created in the solution, as shown in figure 5-12d. The structure is “floating” in the solution. Due to gravity forces, after some time, the structure is overlaid on the cuvette bottom.

The actual beam profile observed on the screen is Gaussian with a smooth intensity distribution shown in figure 5-13a. After a short period, the creation of the condensate in the solution scatters the transmitted light as observed by a gradual change in the beam profile depicted in figures 5-13b, 5-13c & 5-13d. The CCD camera records an increase of intensity of the transversely scattered beam propagating in the condensate, as recorded in figure 5-12b, indicating lossy waveguiding through the formatted fiber string.

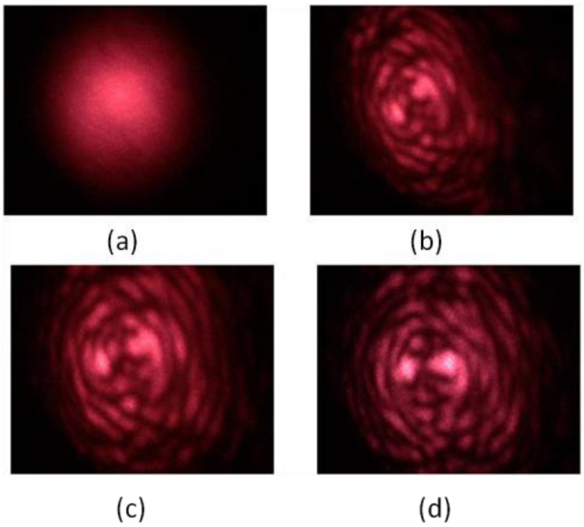

Figure 5-13: (a) laser beam profile upon laser illumination initiation

(b),(c),(d) gradual change of beam profile due to scattering from the created structure

This waveguiding phenomenon is induced due to the radial refractive index gradient in the newly formed fiber, owing to the refractive index difference between the pure polymer solute (n=1.51 for PI) and the solvent (n=1.37 for n-hexane). In effect, due to radiation forces, the solute polymer chains are dragged along the beam axis, forming a string-like structure along this axis. Concurrently the solvent is forced osmotically to move away and the solvent is replaced by the polymer chains along the beam axis.

To elucidate the process, let us consider the phenomenon through a more extensive perspective for condensate microstructure creation. The laser beam of 150 mW power is transmitted through a positive lens and is focused weakly (e.g by a f=150cm - 200cm lens) in the polymer solution producing some kW/cm^2 intensities at the focus. The laser radiation and gradient forces localized in the focal point of the lens tend to drag the polymer chains formerly dispersed in the solution in a random manner to form a polymer microsphere condensate. The latter acts in turn as a second focusing element that forms a third one, thus, consecutively creating a series of microspherical condensates. This array formation is a simultaneous process. In effect, as a consequence of the accumulation of the microspheres, a string-like almost macroscopic structure may be formed upon prolonged exposure, or a direct formation of a fiber string is realized under suitable conditions. The phenomenon is self-terminated, when no further polymer chains can join the micro-string, due to inability of radiation forces to efficiently drag more matter. Macroscopically, the termination of the process is signaled on the screen where the beam profile becomes stationary, but on the contrary, it appears frozen after a period of time when steady state of formation is reached.

The quality of the structures can be further improved by controlling several parameters, such as the laser intensity, the objective focal length, the exposure time, the solution characteristics (concentration, viscosity etc.) and others.

5.3.2 Microstructure creation in thin films & free-standing structures

Radiation forces can be employed as manipulation tool for polymer thin films. In the context of the aforementioned scheme, a polymer solution is deposited to form a thin film. In this form the material exhibits a smaller degree of freedom as compared to the bulk solution, owing to the smaller total volume of material available, the strong surface interactions and contact with the environment. The polymer chains are thus not fully free to move under the gradient force, but forces act to manipulate the surface by dragging the polymer and counteracting surface tension thus leading to the formation of elongated microstructures on the thin film surface. The created structures remain localized in a small volume region and remain a function of the radiation force field imposed.

Experimentally the deposition of the polymer solution on the glass substrates was facilitated using the doctor blade deposition method. The thickness of the polymer film was controlled by micropositioning the blade and parallel movement in order to produce a uniform spread. The distance between the razor and the substrate controls the thickness of the films. The thickness of the samples was in the order of several microns. In a complimentary way, thin films may be deposited via spin-coating where, depending on the viscosity, the solution needs to be in a rather fluid form.

A typical setup used to controllably organize the polymer material and create solid structures by manipulating the surface of thin films deposited on glass substrates is shown in figure 5-14. It consists of a cw laser diode source emitting in the visible, in our case at 671nm, a microscope objective lens, a series of beam aligning mirrors and a translation stage for micromotion control. A Peltier heater device is placed under the glass substrate for the fast vaporization of the solvent and the concurrent solidification of the solute.

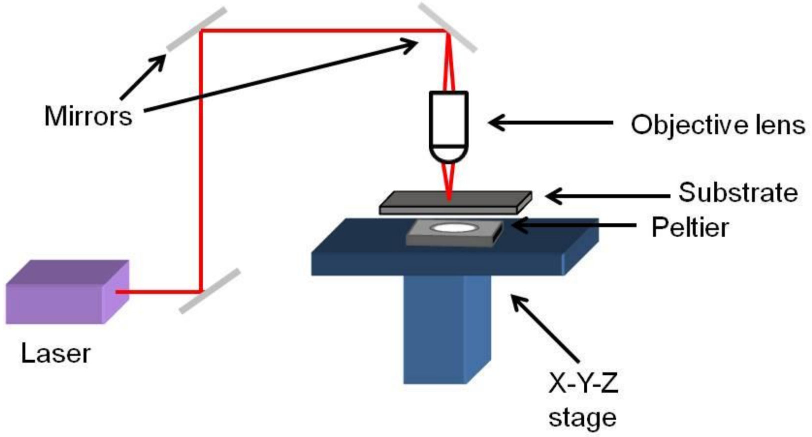

Figure 5-14: Experimental setup for the creation of structures in thin films

A center hole-Peltier module is preferable, so that the laser beam is allowed to pass through the hole and interact with the thin film, while concurrently the glass substrate is heated to the desired temperature, controlled by a power supply. The writing process is monitored in real time via a CCD camera system attached next to the film.

5.3.3 Surface patterning by radiation forces

By applying moderate laser powers in the order of some tens of mW, corresponding to a few ~KW/cm^2 at focus, and by a short illumination time duration ranging from a few seconds up to some minutes, a semitransparent microstructure is created at the focusing point of the objective lens, due to optical radiation forces. For a post-illumination treatment the sample is left on the Peltier device for about 1 hour at 60 ^oC and then carefully stored. Exposure duration is of the order of some tens of seconds depending on the concentration and viscosity of the polymer solution, for given laser parameters.

In an attempt to investigate the effect of the beam on the surface morphology two identical films comprising PI-PVP-Au nanoparticles were examined by AFM, one of them being irradiated with focused laser beam. The results are shown in figure 5-15.

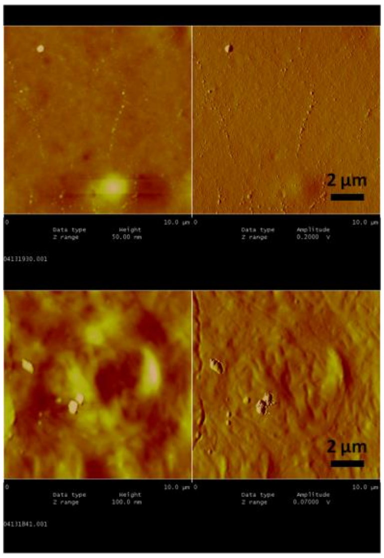

Figure 5-15: AFM image of a smooth (up) film surface and rough (down) film surface, indicative of a structure formation on it

The effect of the laser beam in the irradiated film becomes apparent, creating a visible recess in the surface of the film. Similar structures were further observed with atomic force microscope as depicted in figures 5-16a & 5-16b.

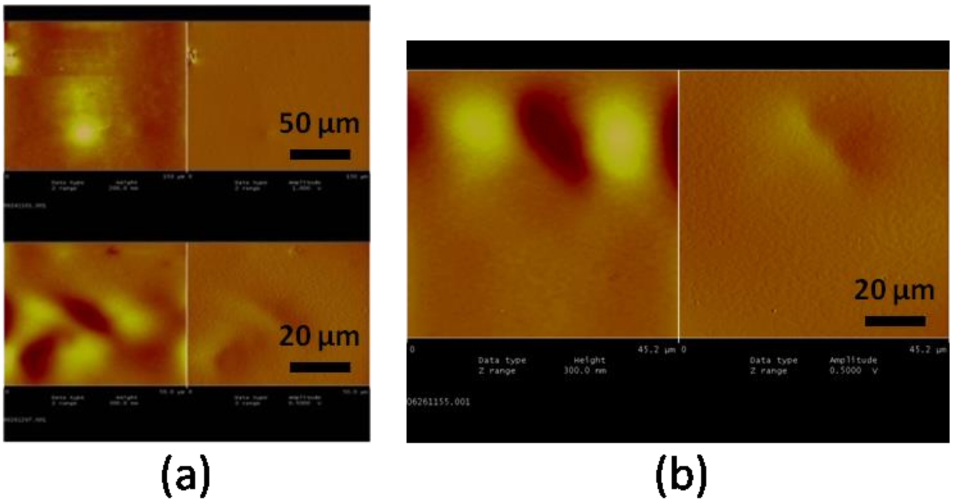

Figures 5-16: (a) & (b) AFM images of film surface showing bulges on top, indicative of structure formation on it.

In the AFM images, the structure edges are clearly shown as bulges on top of the film. Around the edges, shown in dark brown coloration, there are regions of lower height, shown in yellow coloration. The laser beam, due to radiation forces, accumulates material and deposits it on the focal point which is gathered from the adjacent regions, and thus appear as holes.

In order to examine the effect of focusing on the resultant structures, a number of objective lenses exhibiting different magnification powers (10× and 20×) were used. The resulting structures were found to be highly dependent on the magnification of the lenses, with the structure size being inversely proportional to the magnification power of the lens owing to the focusing strength, thus confirming the theoretical expectations. In particular, in the case of 20× objective lens, it was noticed that only one sphere of large diameter was created, despite the relevantly high writing duration and full power of laser irradiation. Given the depth of focus, Δf:

$$\Delta f = 2\lambda f_{num}^{2} \quad [5.6]$$

where: $f_{num} = \frac{1}{2NA}$, for both 10X (0.25 NA) and 20X (0.4 NA) objectives we have Δf~ 5μm and 2 μm, respectively. These numbers corroborate the creation of rod like structures by longer depth of focus imaging, whereas shorter depth of focus produces spherical micropatterns.

Experimentally it has been observed that integrated exposure is a main parameter in structure fabrication. In an attempt to investigate the effect of laser beam exposure in the creation of patterns, the power of the laser beam was changed from 150 mW to 70 mW, by using an optical attenuator, as measured with a power meter (Newport model 2832-C Dual Channel). It was found that in order to achieve a structure of the same dimensions, almost double the writing time was needed, i.e. by using a 10X objective in both cases, the exposure time was about 10-15 seconds at full power of ~150mW, and 30-40 seconds for the lowest attenuated beam of ~70mW. Thus, the resulting structure was created at longer writing times, indicating the inverse proportionality of the two parameters. A typical created structure is about 0.4mm in length and about 10μm in diameter. The dependence of the structure length on exposure time for given power is shown in figure 5-17 and appears almost linear.

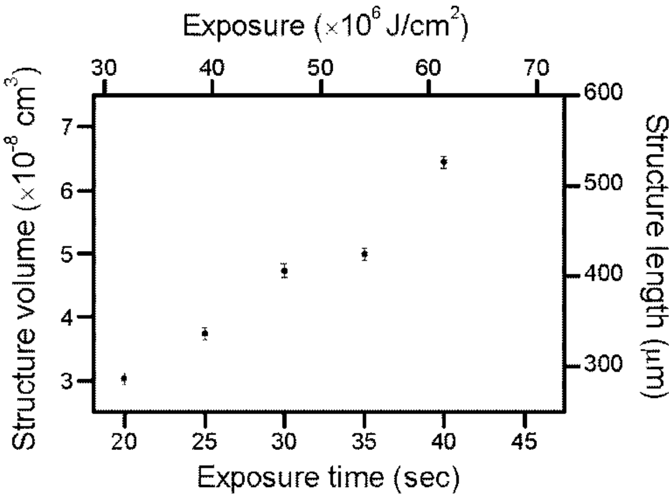

Figure 5-17: Structure length and volume v. exposure time.

5.3.4 Application of holographic optics for surface microstructuring

Surface microstructures by fanout irradiation were created in thin films of PB (Polybutadiene) under similar writing procedures[8]. The experimental arrangement of figure 5-18 was used where a holographic mask was inserted before the objective lens.

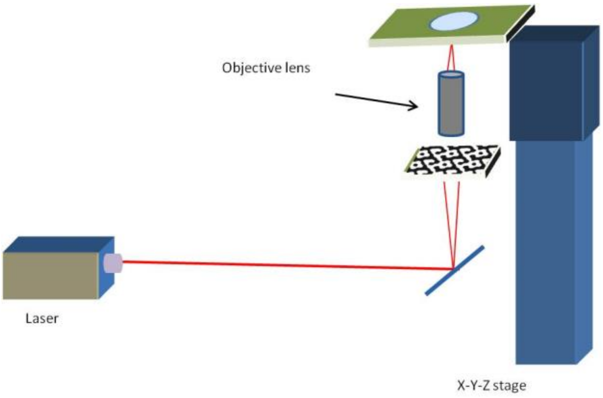

Figure 5-18: setup used for holography-assisted multiple spot patterning in a polymer thin film

Fanout patterns were transferred on the film and imaged by a microscope as shown in figures 5-19a - 5-19d, where the features correspond to surface modifications induced by transferring simultaneously all the fanout topology. The resultant structures have also been characterized by SEM and the diameter of spots was found to be in the range of 50-60 μm.

---

[8] PB material was provided by Dr. M.Anyfantakis, Prof. G.Fytas group, IESL, FORTH, Heraklion, Crete. Their contribution and help is highly acknowledged.

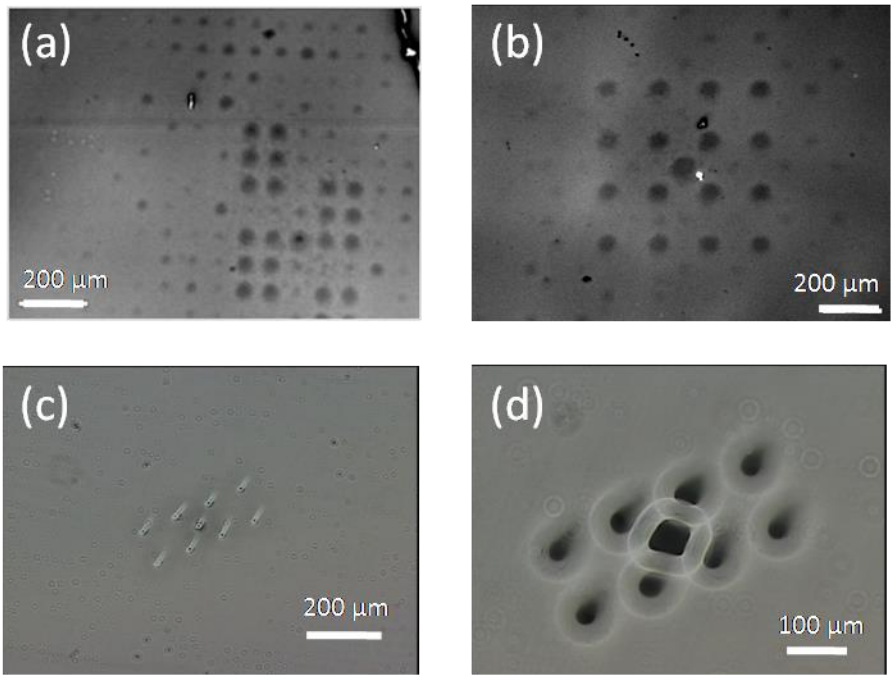

Figure 5-19: (a) & (b): scanning electron micrographs of the formation of multiple spots with the aid of holographic masks. (c) & (d): Optical microscope images of the created structures. The central spot appears bigger, due to the higher energy used for the zero order. The mask used was not optimized in order to give spots of equal intensities.

In the SEM images, it is clearly shown that the use of holographic masks has resulted in the creation of pillar-like structures on top of the thin film. Furthermore, the central spot which has been produced by applying higher power appears to be higher compared to the other spots. The latter can de deduced from figure 5-19d, where the shadow of the central spot appears bigger as projected which means that it is closer to the microscope illumination light as compared to the other spots.

5.4 Beyond thin films: structure creation in a variety of formations

5.4.1 Creation of free-standing structures

Interesting results were obtained by modifying the orientation of the thin film with reference to the beam normal. Parallel, perpendicular and slightly tilted configurations have been used to investigate the dependence of angle of incidence to the geometrical characteristics and uniformity of the structures. In a vertical direction, normal to the film, with the deposited material being under the glass surface, tiny columns of material of the film appear on the substrate surface, aided minimally by gravity forces. Typical three-dimensional cylinder rod-like microstructures formed on planar parent substrates are shown in figures 5-20a- 5-20e with structure diameter of the order of 5-10 μm.

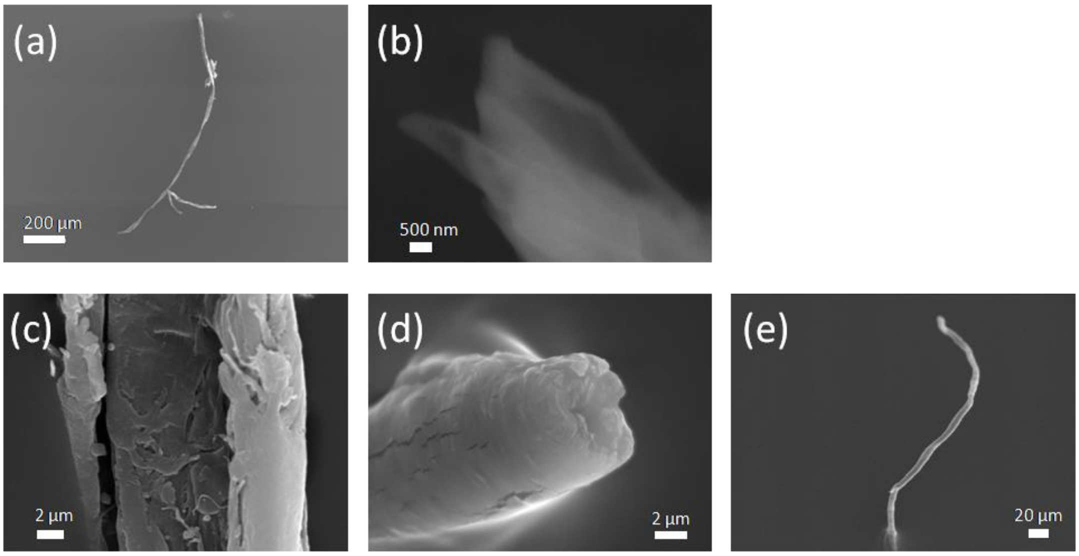

Figure 5-20: (a) SEM image of a created structure. (b) Detail of the end tip of the created structure. (c) Detail of a fracture and internal structure. (d) end tip of the structure. (e) Scanning electron micrograph of created solid polymer structure standing on a planar substrate having visible roots at the lower edge of the image.

Interesting results were obtained by ceasing the writing process, before a fully developed structure was developed. Under that regime, polymer microspheres connected to each other are visible, indicative of the process (figures 5-21a - 5-21d). According to that, each microsphere acts as a microlens allowing the further focusing of the laser beam and thus allowing the phenomenon to create an elongated structure.

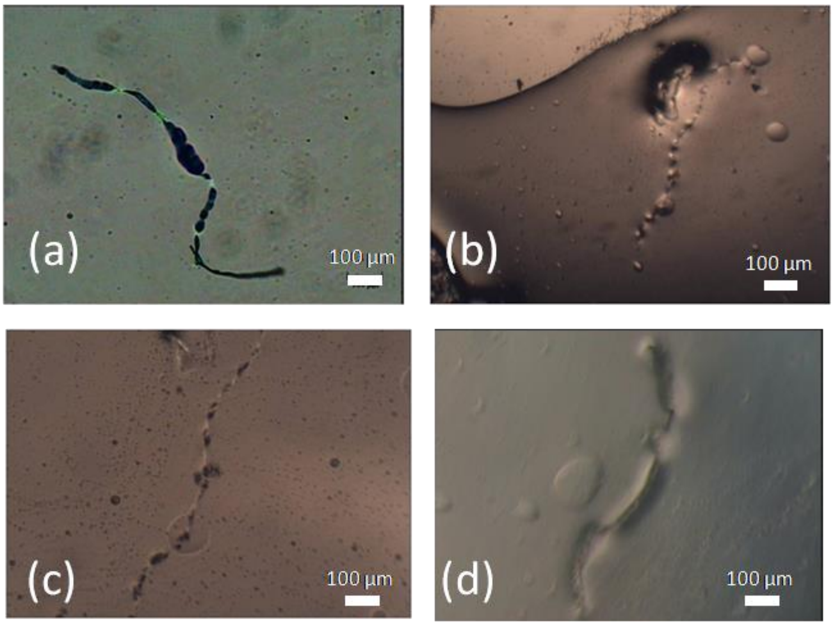

Figure 5-21 a-d: Typical optical microscope images of structures created on a thin film. Spheres of several sizes are visible, depending on the illumination conditions.

Several images of created structures were acquired both via optical microscopy and SEM, as shown below in figures 5-22 a-e.

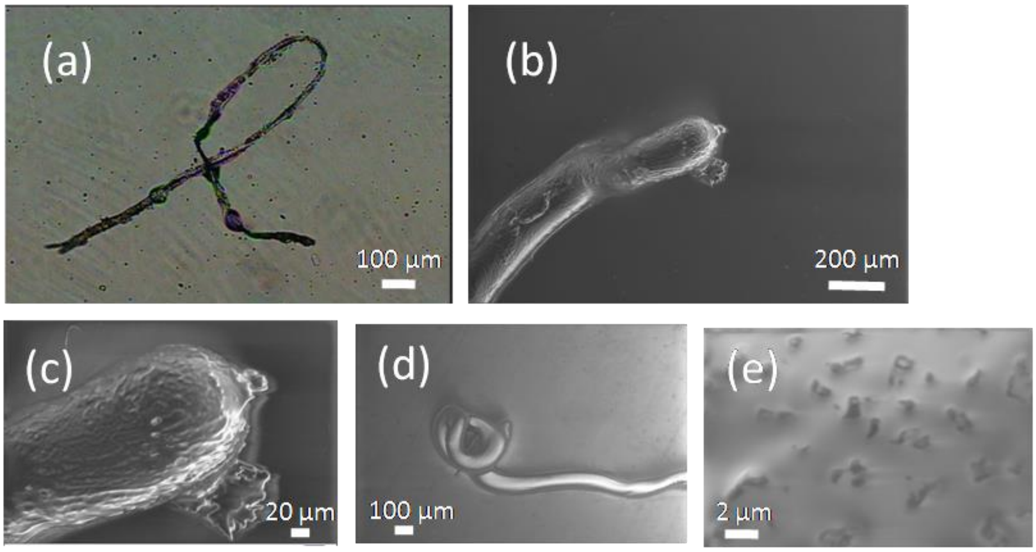

Figure 5-22: (a) Optical microscope image of a formed structure. (b) SEM image of the end tip of the structure. (c) Close-up scanning electron micrograph of the created tip. (d) Panoramic and (e) close-up high-pressure environmental mode scanning electron micrographs of hybrid fiber (uncoated as produced sample).

Upon illumination, the structures exhibit remarkable waveguiding properties, though lossy due to scattering effects. As outlined above, such properties are attributed to the refractive index gradient owing to the difference between the polymer solute (n_{PI}=1.51) and the solvent n-heptane (n_S=1.39). In the case of 1,4-polybutadiene the refractive index variation applies as n_{PB}= 1.51 and n_{decane}= 1.41.

The length of the structures was found to be in the range of 20-25 μm, the diameter about 3 μm, while the height above the substrate surface was about 300 nm, as shown in AFM figure 5-16b. It should be mentioned at this point that the created structures cannot be extracted from the film due to the strong adhesion forces evolved in the material.

As previously mentioned, the tiny columns resemble to rods. The rods could not be noticed by optical microscopy due to the orientation of the structures and only the edges were visible. They were short and rather thick in order to be self-standing, static and self-supported. Once the structures get quite long (of the order of mm), they appear to be curved due to gravity and the viscoelastic nature of the material.

The writing/creation of microstructures can be accomplished in almost any form of entangled polymer solution. The aforementioned setup was used for the writing of a structure in a polymer droplet that had just been ejected from a syringe tip, in free space. The resulted structure was then observed in a microscope, as shown in figure 5-23a & b.

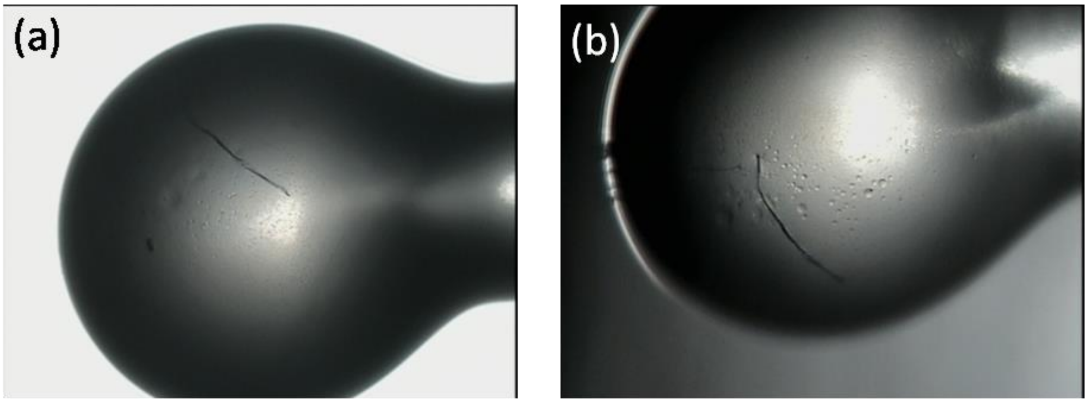

Figure 5-23: (a) & (b) Optical microscope images of a created string-like formation in free space polymer blob.

5.4.2 Plasmonic and fluorescent quantum dots hybrid structures

In a complementary effort, the polymer solution acts as a matrix element where several dopants can be added. Au nanoparticles can be successfully added in the polymer matrix by following the procedures outlined in the last part of the chapter. The structures to be created using this solution exhibit remarkable plasmonic characteristics. Furthermore, CdS quantum dots were added in the polymer solution in micellar form. The final solution has a yellowish appearance due to quantum dots. The solution was then deposited on a glass substrate following the same procedure for microfiber creation in the thin film, the created microstructures were observed under the microscope. Typical images are shown in figures 5-24a - 5-24f. The intense contrast between the polymer thin films and the created structures is apparent due to the fact that the quantum dots were dragged and accumulated at high concentrations during the formation process, being trapped in the net of entangled polymer chains under the exertion of optical forces.

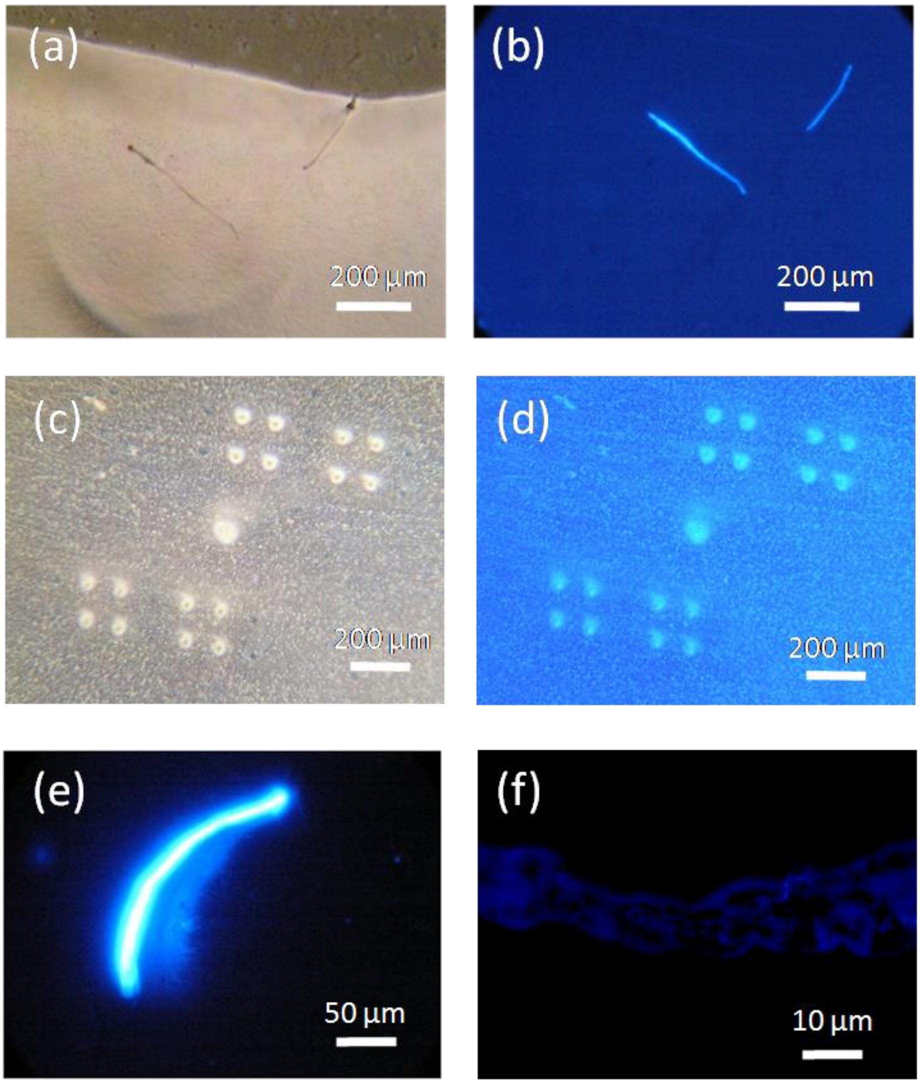

Figure 5-24: (a) Optical microscope and (b) Fluorescence microscope image of the same created structure in thin film. (c) Optical microscope and (d) Fluorescence microscope image of the same holographic structure. (e) Image of a fluorescent CdS quantum dots hybrid polymer structure emitting at 470nm. (f) Image of the glowing chain of a created CdS structure.

Some typical structures created in CdS doped polymer matrix are shown in figures 5-25 a&b.

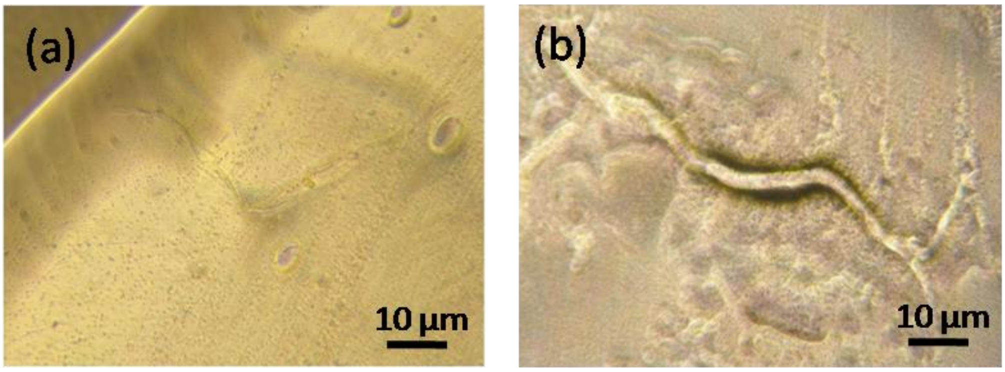

Figure 5-25: (a) & (b) Typical structures created in CdS doped polymer. The yellowish coloration is characteristic of the material.

5.4.3 Fiber drawing by laser radiation forces

The experimental setup was further changed in order to examine the feasibility of structure creation in open space. The setup consisted of a laser source, an objective lens and a syringe carrying the polymer solution. The lens used was 10×, the laser operated at full power (150 mW) and the writing process was monitored in real time using a CCD camera. The laser beam was focused in a droplet formed at the syringe tip as shown in figure 5-26.

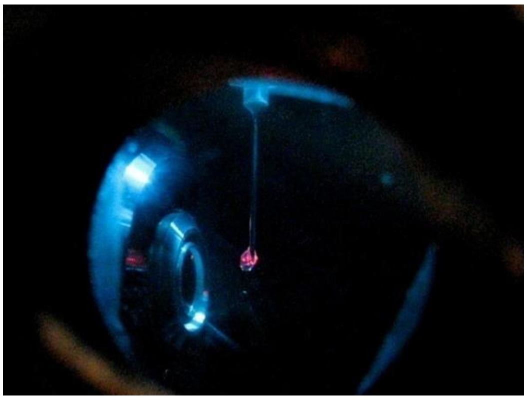

Figure 5-26: Real –time image of the fiber-drawing process

Radiation forces are applied and drag a polymer fiber by pulling and solidifying the entangled polymer in free space. This process is self-sustained as feeding comes naturally through the syringe. The phenomenon is thus self-conserved resulting in the creation of a flocculent and fully elastic rubbery PI fiber structure. The ring-like appearance shown in figures 5-27 a&b is due to self-winding. The total duration of the process is about 10-15 minutes. It should also be noted here that the whole process is driven by radiation forces and no further operation is needed to assist the fiber drawing process.

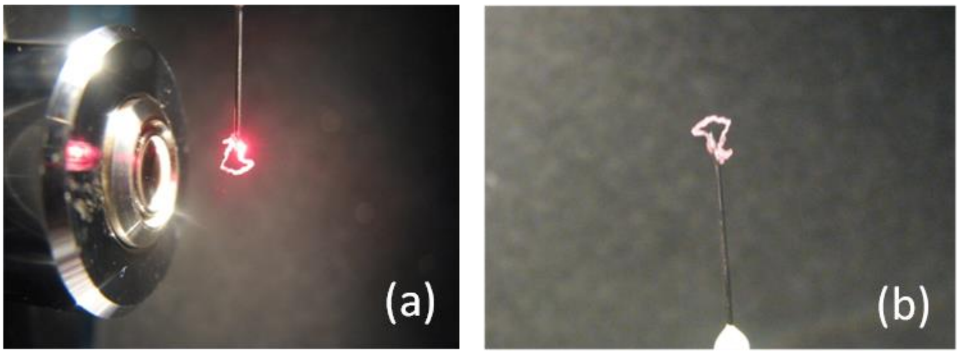

Figure 5-27: (a) Ring-like structure formation at the edge of a syringe needle during the writing process. (b) The ring-like structure after the completion of the writing process. The reddish coloration is characteristic of the Au nanoparticle containing polymer material.

An interesting phenomenon was observed while attempting the aforementioned process. At first, the blob had a typical spherical shape, as shown in figure 5-28a. After a few seconds the blob was deformed (figure 5-28b) resulting in a plano-convex shape (figure 5-28c). This can be attributed to the fact that the focal spot is at the front of the blob resulting in the solvent removal at that point.

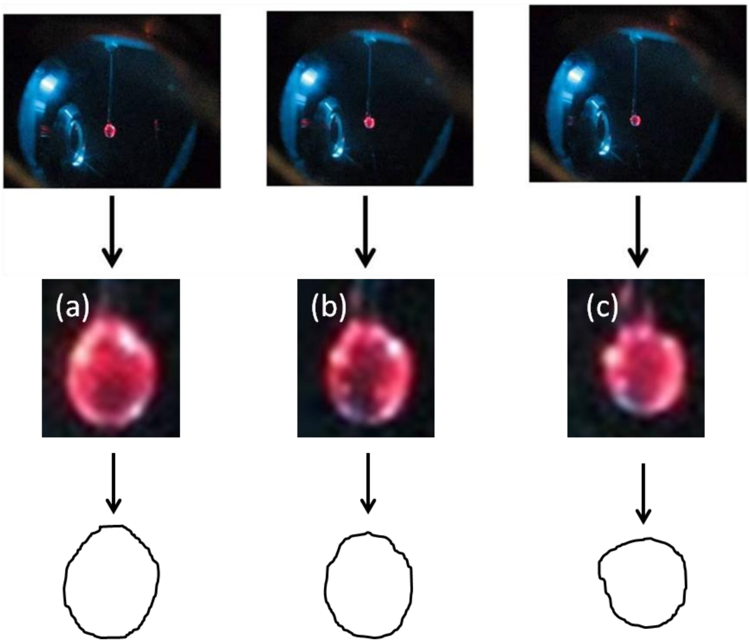

Figure 5-28: (a) The initial stage of the writing process where the blob appears spherical. (b) & (c) Gradual deformation of the spherical shape of the blob. The focused laser beam forces the solvent away resulting in a deflating-like phenomenon. The contour of the blobs is shown in the bottom of image.

Another interesting result is related to the elastic characteristic of the created string. The string is highly elastic acting as a spring with the typical structure shown in figures 5-29a&b exhibits a rubbery mechanical response, as expected for the PI material.

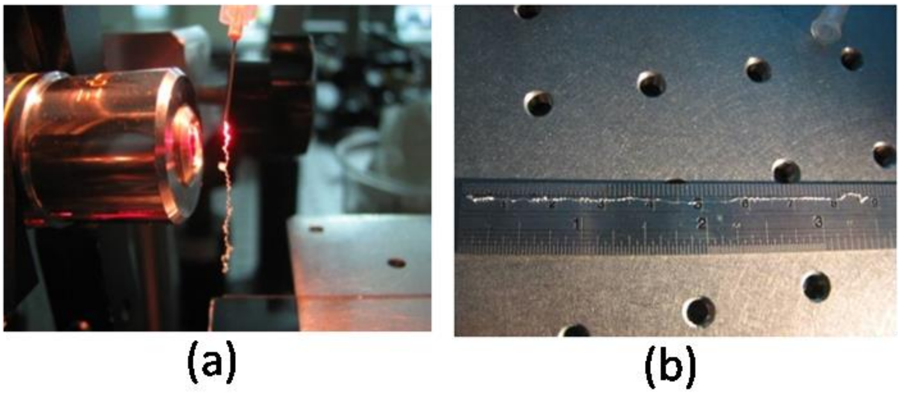

Figure 5-29: (a) String-like structure created in free space. (b)The structures can reach several centimeters in length.

In addition, the structures created by using that method develop strong electrostatic forces. By approaching a metal tip, the polymer string is strongly affected, moving towards the tip. The electrostatic characteristic of the created structure is shown below in figures 5-30a-f.

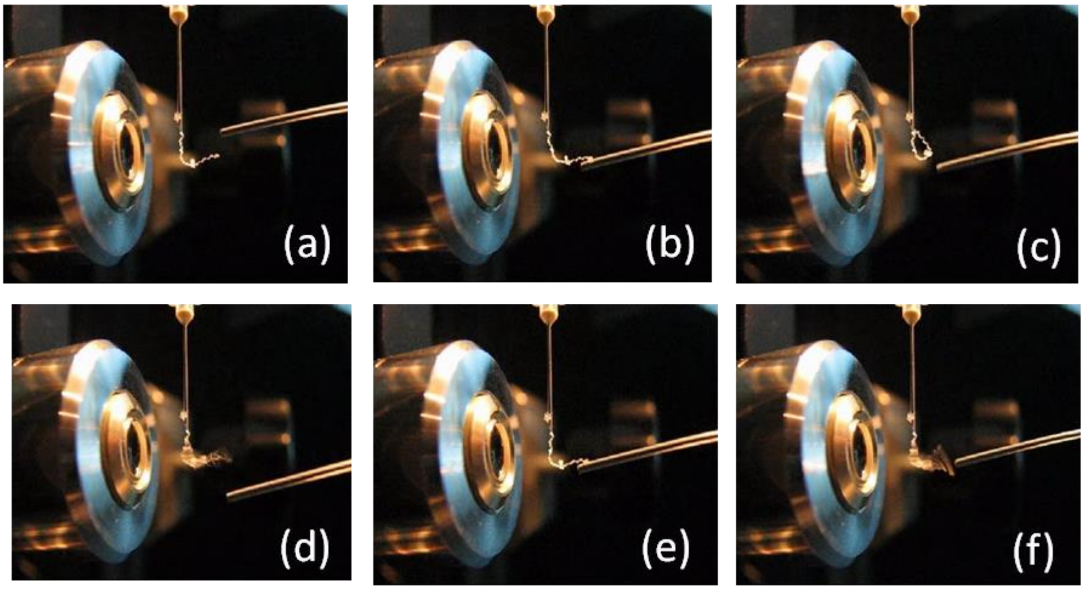

Figures 5-30: (a) – (f) Upon proximity to the metal tip, the created string-like structure reacts electrostatically by moving towards it.

Additionally, optical microscope close-ups of the formed helical structures are shown in figures 5-31a&b.

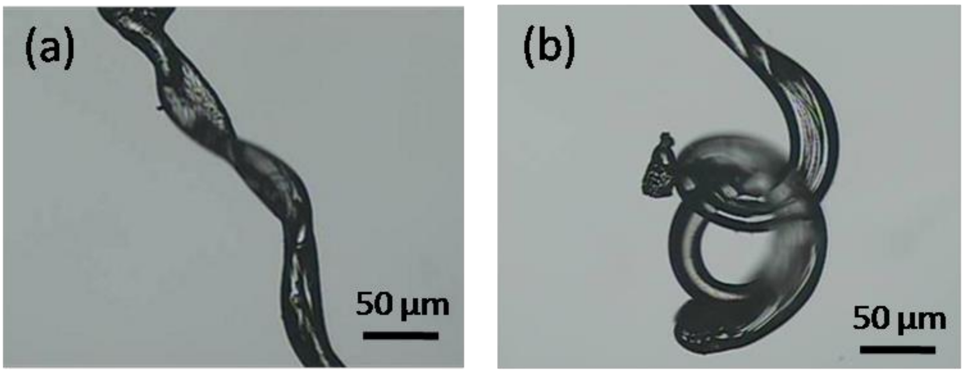

Figures 5-31: (a) & (b) Close-ups of helix-shaped structures created by fiber-drawing technique (optical microscope)

5.4.4 Torus-like structure formation and extruding microstructures

By suitably altering the experimental setup, a motorized rotating stage was used in order to keep the substrate in constant rotation around an axis, while in parallel the z-axis was moved in order to focus at different heights at given steps. The rotation speed was kept low in order for the writing process to take effect. The result was very interesting giving 3-D structures of torus-like shape, as shown in figures 5-32a-d.

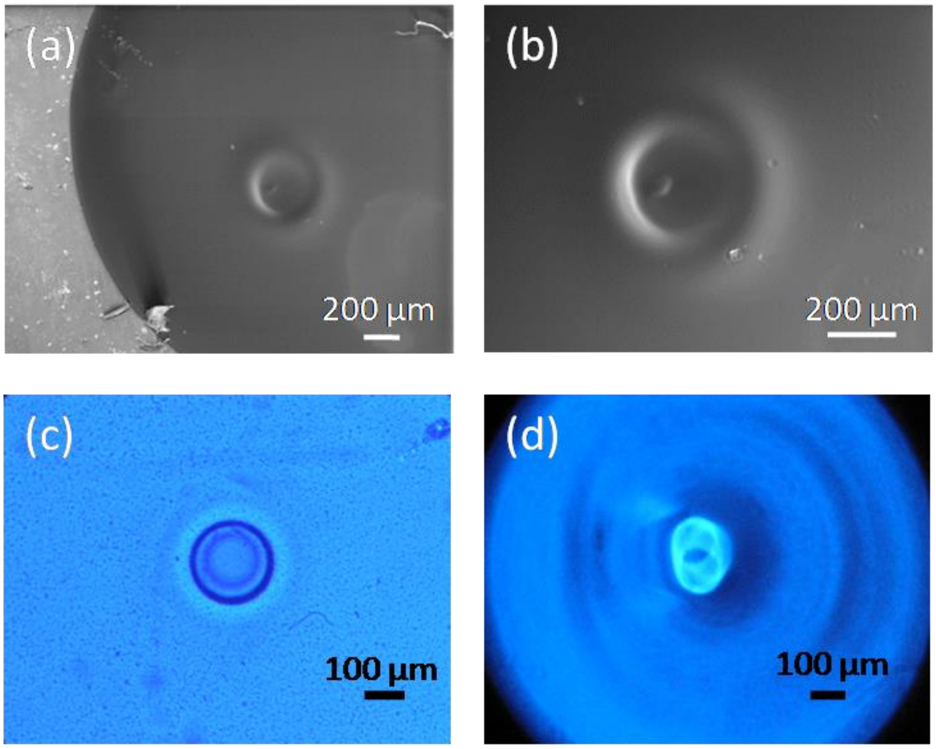

Figure 5-32: (a) SEM image and (b) close-up of a created torus-like structure. (c) The created structure in fluorescence microscope appears in dark blue due to the presence of CdS quantum dots. (d) Fluorescence microscope image of tilted film. The structure is shown in 3-D forming a cylinder.

Further alterations to the orientation of the setup resulted in 3-D of various shapes, as shown below in figures 5-33a&b. In all cases, the key point is the constant movement of the z-axis at the translation stage resulting in a sculpturing-like action.

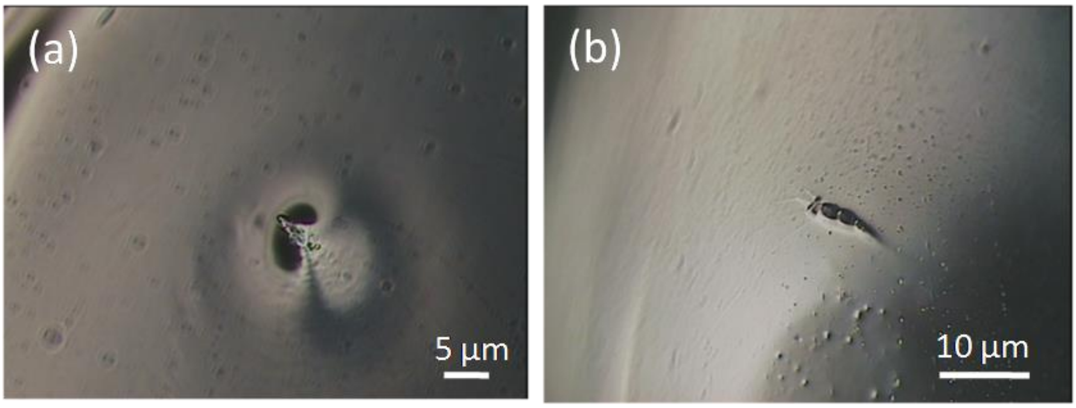

Figures 5-33: (a) & (b) Typical 3-D extruding microstructures as a result of the constant motion of the z-axis while attempting the writing process

5.5 Synthesis and characterization of polymer materials and hybrids

High cis 1,4 polybutadiene (PB) sample has been utilized, having a branched molecular architecture. High molecular weight polyisoprene (PI) homopolymer was prepared in-house by the use of anionic polymerization high vacuum techniques [17, 18] utilizing home-made glass reactors and break seal techniques[9]. s-BuLi was the initiator used in the non-polar solvent benzene. Polymerization reactions were carried out at room temperature. Under these conditions PI chains of low molecular weight distribution with controlled molecular weights and having high 1,4 microstructure are obtained, as evidenced by size exclusion chromatography determinations and ^{1}H-NMR spectroscopy measurements. The final PI homopolymer was isolated by precipitation in stabilized methanol and dried under vacuum for several days at room temperature. The polyisoprene-b-poly(2-vinyl pyridine) (PI-P2VP) block copolymer also employed as the polymeric functional material in these studies was obtained by an anionic polymerization scheme involving two steps. Isoprene monomer was

---

[9] Polymer solutions were synthesized and provided by Dr. S. Pispas and Dr. Ch. Mantzaridis. Their contribution is acknowledged.

polymerized first in benzene at room temperature, using s-BuLi as the initiator, according to previously described procedures. The living poly(isoprenyl lithium) solution was isolated in a glass ampoule, equipped with a break seal, and was subsequently utilized as the macroinitiator for the polymerization of 2-vinylpyridine. Polymerization of the second monomer was carried out in THF at -78°C. The small amount of benzene present from the preparation of the PI macroinitiator does not perturb the formation of the poly(2-vinyl pyridine block) (P2VP). After formation of the P2VP block, deactivation of the living chains was achieved by degassed methanol. The copolymer solution in THF was concentrated in a rotor evaporator (by distilling about 2/3 of the solvent) since direct precipitation of the copolymer from the THF-rich solution is not quantitative. The pure PI-P2VP diblock copolymer was then isolated in solid form by precipitation in stabilized cold methanol and dried in a vacuum oven at room temperature for several days.

Polymer samples were characterized in terms of molecular weight and molecular weight distribution by size exclusion chromatography (SEC), as well as in terms of PI microstructure and copolymer composition by ^{1}H-NMR spectroscopy. The detailed molecular characteristics of the samples utilized are shown in Table 5-1. No alteration of their chemistry has been observed by the formation operation

Sample	**Mw (x 10^{-3})**	**M_w/M_n**	**Microstructure (PB or PI)**	**%wt P2VP**
PB-390	390	2.5	High cis 1,4	
PI-4	1500	1.07	High cis 1,4	
PI-P2VP-2	55	1.05	High cis 1,4	9

Table 5-1. Molecular characteristics of the polymers utilized in this study

5.5.1 Preparation of PI-P2VP micelles containing Au or CdS nanoparticles

PI-P2VP micelles were prepared in n-heptane which is a selective solvent for the PI block. The solid polymer was directly dissolved in the solvent in a stopper vial in order to give a copolymer concentration $C_{PI\text{-}P2VP}$= 1% w/v. The solution was subsequently heated at 60^{o}C for 2h in order to facilitate complete dissolution of the copolymer and equilibration of the micelles. In this solvent the copolymer forms spherical micelles with P2VP cores and PI coronas. This is evidenced even by the naked eye due to the bluish tint developed in the solution. Quantitative dynamic light scattering measurements after 24h of solution preparation gave the mean hydrodynamic radius of the micelles (R_h=33.6 nm).

The PI-P2VP micelles were subsequently utilized as nanoreactors for the synthesis of Au and CdS nanoparticles. In the case of Au nanoparticle formation, auric acid (as ethanolic solution) was introduced in the PI-P2VP micellar solution in the predetermined stoichiometric amount to the pyridine units (N:Au = 4:1). This high N:Au ratio facilitates quantitative complexation of the gold ions with the nitrogen atoms of the pyridine rings of the copolymer. Complexation of the pyridine units of the P2VP block with the gold ions takes place in the micellar cores which act as nanoreactors for metal nanoparticle nucleation and growth. After allowing for equilibration for 24h, gold ions were reduced to gold by the use of hydrazine solution in ethanol (hydrazine:Au = 4:1). The nanoconfinement of the micellar cores led to the production of gold nanoparticles, as evidenced by UV-vis spectroscopy measurements [19]. Adsorption maximum for the surface plasmon resonance peak of the produced gold nanoparticles was observed at ca. 540 nm.

A similar preparation protocol was also followed in a second case. Cd^{2+} ions were loaded in the PI-P2VP micellar cores in the form of cadmium acetate ($N:Cd^{2+}$ = 4:1). The mixed solution was stirred for 24h hour. During this period cadmium acetate was completely dissolved, presumably within the micellar cores, due to the chemical affinity of the polar pyridine groups for the Cd^{2+} ions. In the next step, thioacetamide was introduced into the solution of loaded block copolymer micelles. Thioacetamide was utilized as the source for sulfur, through its decomposition at 80^{o}C (S/Cd ratio was kept at 2). The formation of CdS nanoparticles in PI-P2VP micelles was confirmed by UV-vis and fluorescence spectroscopy [20].

Inorganic nanoparticles-loaded block copolymer micelles were mixed with solutions of PB and PI homopolymers in n-hexane in order to produce hybrid non-covalent interacting homopolymer/micelles mixtures. The similar chemical composition of the micellar corona with the matrix homopolymer enhances such interactions and facilitates decoration of fibrilar polydiene structures, formed upon subsequent exposure of solutions to laser radiation. In this way hybrid nanostructures are produced solely by the laser action. Fluorescent hybrid CdS/PI-P2VP micelles may act also as markers/probes for direct visualization of homopolymer chain ordering.

A typical TEM image of a CdS encapsulated micelle is shown in figure 5-34.

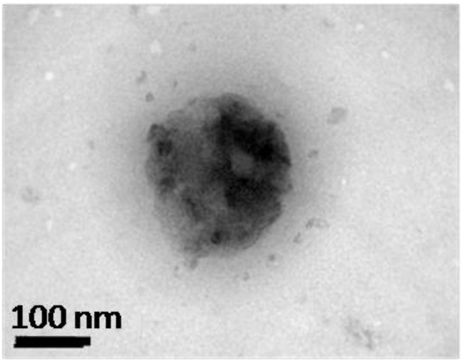

Figure 5-34: Transmission electron microscope image of a polymer micelle encapsulating CdS nanoparticles

The structures produced are found to be highly fluorescent as compared to the parent material owing to the strong densification and trapping of quantum dots. In the open space fiber drawing mode, very long strings (~ 10 cm) have been created. The fluorescent objects formed were observed under the fluorescent microscope and spectrally analyzed. A typical fluorescent emission spectrum recorded is shown in figure 5-35, with the peak at λ_{fluor}~470 nm indicating a maximum CdS quantum dot size of ~4 nm.

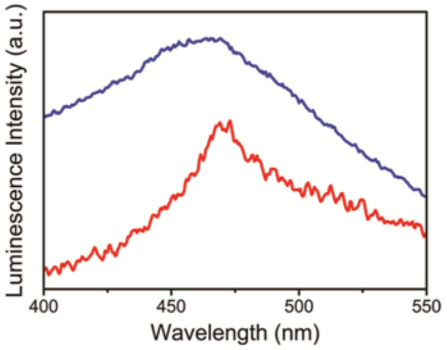

Figure 5-35: Fluorescent emission curve of a free standing polymer structure containing CdS quantum dots. The blue curve is the spectrum of the polymer solution.

In a similar operation, the plasmonic behaviour of Au-enriched material has been verified with typical absorption curves depicted in figure 5-36.

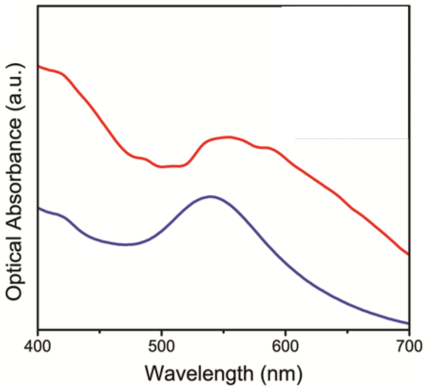

Figure 5-36: Plasmonic curve of a free standing polymer structure containing Au nanoparticles. The blue curve is the spectrum of the polymer solution.

A typical TEM image of the Au nanoparticle encapsulated micelles is shown in figure 5-37.

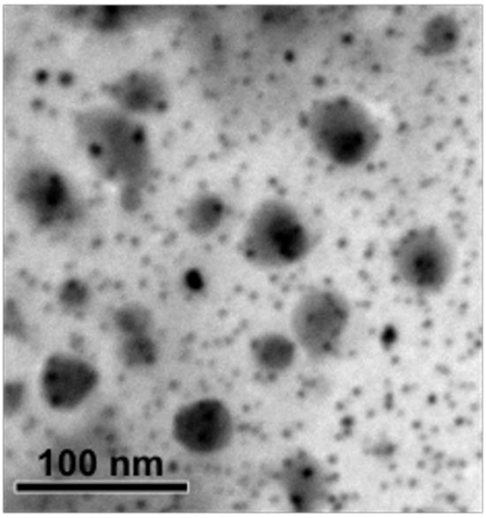

Figure 5-37: Transmission Electron Microscope image of polymer micelles encapsulating Au nanoparticles

In both cases identical responses with respect to the parent solutions depicted in blue lines in figures 5-35 and 5-36 have been observed with minimal shifts indicating the created denser ambient matrix environment for the nanoparticles and quantum dots. No detrimental effects such as metallization and fluorescence quenching have been observed, verifying that the formation process is dielectrically shielded ensuring absence of aggregation in the final solidified nanocomposites.

5.6 Concluding remarks

Significant efforts were devoted to establishing a picture regarding non reversible chemical processes which may take place during formation of the formed nanostructures, and may compromise reversibility of the formation process. One concern is the chemical stability of polydienes under prolonged and intense irradiation with a laser beam, due to the presence of C=C bonds. Careful Nuclear Magnetic Resonance (NMR) and Size Exclusion Chromatography (SEC) experiments on the polymeric materials isolated after sample irradiation, indicated no detectable changes in their chemical structure (i.e. absence of oxidation), as well as the absence of cross-linking or chain scission. The absence of appreciable cross linking was also verified by dynamic light scattering measurements in solutions of the irradiated material in THF. Reversibility testing of the created structures was performed. Solvent was added to a 3D structure and after stirring for some minutes, the structure disappeared, being transformed to the solution previously used. Such findings verifying reversibility in liquid condensates have also been reported by Sigel et al [1].

The composition of scattering and gradient radiation forces is now offering important tools for the manipulation of inorganic and biological matter by means of particle trapping using optical tweezers and structure actuation. Beyond these applications, the concept of light-induced forces exerted in soft matter at the mesoscale, opens up new horizons by allowing efficient density manipulation and the formation of solid objects. Microstructure creation is implemented solely by the above optical means in semidilute, entangled polymer solutions with remarkable results. Pointing to an emerging microfabrication technology, especially suitable for photonics applications, we demonstrated and discussed in this chapter several forms of structures in planar and three dimensional free-standing micro-objects, in addition to a unique polymer fiber drawing operation, by the sole use of radiation forces.

The observed intriguing phenomena are currently under further study and may be illustrated in terms of a synergy of radiation forces, chain entanglement and optical field structuring and waveguiding, as discussed in this work. The topic is opening up a large area for fundamental investigations in polymer science and photonics. Emerging concepts on materials microstructuring in three dimensions would take advantage of the chemically inert nature of the process to yield a rich palette of microfabrication tools. These will offer compatibility with both inorganic devices and biological material, leading the way to hybridization and novel lab-on-chip schemes. The ability to tailor surfaces in the nanoscale with reversibility may also offer new tools in optical memory and related applications, also prompting hybrid and unified approaches in photonics, information and biomedical technologies.

5.7 References

1. Sigel R., Fytas G., Vainos N., Pispas S. and Hadjichristidis N., Science 297, 67(2002)

2. Loppinet B., Somma E., Vainos N. and Fytas G., J. Am. Chem. Soc. 127, 9678(2005)

3. Anyfantakis M., Loppinet B., Fytas G., and Pispas S., Opt. Letters 23, 2839(2008)

4. Anyfantakis M., Loppinet B., Fytas G., Mantzaridis C., Pispas S. and Butt H. J., J. of Optics 12, 124013(2010)

5. Maxwell J. C., Oxford Clarendon Press(1873)

6. Ashkin A., Phys.Rev.Lett. 24,156(1970)

7. Ashkin A., Phys. Rev. Lett. 40, 729(1978)

8. Ashkin A., Dziedzic M., Bjorkholm J. E. and Chu S., Opt. Lett. 11, 288(1986)

9. Ashkin A., Biophys. J. 61, 569(1992)

10. Cizmar T, Davila Romero L. C., Dholakia K. and Andrews D. L., J. Phys. B: At. Mol. Opt. Phys. 43, 102001(2010)

11. Harada Y. and Asakura T., Optics Communications 124, 529(1996)

12. Nieminen T. A., Knoner G., Heckenberg N. R. and Rubinsztein-Dunlop H., Meth. in cell biology, 82, 207(2007)

13. Greene W.M., Spjut R. E., Bar-Ziv E., Sarofim A. F. and Longwell J. P., J. Opt. Soc. Am. B 2, 998(1985)

14. Metzger N. K., Wright E. M. and Dholakia K., New Jour. of Physics 8, 139(2006)

15. Edwards S. F., Proc. Soc. London, 92, 9 (1967)

16. De Gennes P. G., “Introduction to Polymer Dynamics”, Cambridge Univ. Press (1990)

17. Hadjichrisitidis N., Iatrou H., Pispas S., Pitsikalis M., J. Polym. Sci. Part A: Polym. Chem. 38, 3211(2000)

18. Uhrig D. and Mays J. W., J. Polym. Sci. Part A : Polym. Chem. 43, 6179(2005)

19. Meristoudi A., Pispas S. and Vainos N., J. Polym. Sci. Part B: Polym. Phys. 46, 1515(2008)

20. Gatsouli K., Pispas S. and Kamitsos E. I., J. Phys. Chem. C 111, 15201(2007)

6. Conclusions and outlook

This doctoral dissertation addresses the design, fabrication and study of microstructures by use of laser beams and is especially directed to photonic applications. The thesis embraced, developed and analyzed a number of microstructure fabrication techniques and blended them with new nanocomposite photonic materials for sensor applications. In addition, investigated novel effects relating to microstructuring of soft matter, pure or hybrid, by use of laser radiation forces and discussed a possible explanation of the complex but intriguing phenomena involved.

The behavior of several materials upon laser illumination was also studied with a view to reveal possible laser-material details. For that reason, sol-gel (TMOS) material was illuminated with two laser sources in the UV spectral region (Ar laser @ 193 nm and F_2 @157 nm). It was found that surface morphology was modified in a controllable way with physical and chemical properties strongly depending on the illumination conditions. Ablative ultraviolet laser surface processing is a generic single-step approach that can be applied successfully in composite materials.

The impact of 193 nm laser fluence and 157 nm number of pulses was studied, by monitoring the surface before and after laser exposure aiming to understand the influence of UV irradiation on the film structure and surface morphology, and optimize the processing of composite materials. Modification of surface roughness of the organic films is expected to enhance the sorption of various detectable chemical agents. In parallel the chemical modification of the surface at 157 nm enhances the target-probe binding strength and thus the detection sensitivity in sensing applications. Optimization of the excimer laser radiation process will result in the improvement of structure quality and resolution of the fabricated features towards obtaining nanoscale-level processing, thus opening new horizons in the fabrication of nanostructures in several application fields. The results can be used for the formation of micro/nanostructures in hybrid photonic and optoelectronic devices.

In addition to sol-gel material, Polydimethylsiloxane (PDMS) films were also studied upon illumination with 193 nm excimer laser. Samples were studied before and after exposure to 193 nm laser light to understand the influence of UV irradiation on the films' chemical structure and surface morphology. The irradiation caused photo-dissociation of bonds followed by the formation of new ones. The chemical changes were accompanied by surface morphology modification. The effect of excimer laser illumination on material properties was also studied in the case of polyisoprene-poly(acrylic acid) and hybrid inorganic-organic material, namely TEOS-MAA-PEG :Au where interesting results were obtained as for the softness/hardness of each material and thus their ablation thresholds.

The use of laser micromachining was further exploited for other materials and devices. A thorough study on POF surface modification by direct excimer laser etching was performed for sensing applications. The study comprised a set of experiments for the determination of ablation threshold for the PMMA (being the POF material) where an interesting phenomenon arose due to the different ablation thresholds of cladding and core material. Following laser microfabrication, emphasis was placed on rapid prototyping and replication of microstructures initially designed for specific photonic applications. The work comprised the design of diffraction gratings of various characteristics. For that reason, special CAD software was used. The grating designs were then used in order to fabricate the actual devices using Reactive Ion Etching (RIE) mainly for sensing purposes.

The work was expanded to the design of other optical elements, such as Fresnel lenses. In order to design Fresnel lenses, a calculation of the radius of each zone had to be performed, followed by the use of CAD software. The final designs were transferred to actual devices by use of RIE. Computer Generated Holography was employed in order to obtain designs of complex shape and functionalities. In order to acquire masks mainly for beam splitting applications, special software for CGHs was used. A plethora of designs was obtained, each one giving a different fanout, according to application needs. All designs were transferred to metal substrates and can be used in many photonic applications, demonstrating the versatility of such devices.

Moreover, soft lithography techniques were used in order to obtain microstructures (diffraction gratings) for sensing applications. Diffraction gratings were fabricated by negative photolithography and the use of commercial photo resist. Subsequently, they were coated with a functional hybrid layer thus forming a complex system comprising a modulated effective index of refraction and a modified surface grating profile. For that reason, two categories of polymers, namely poly(ethylene oxide) (PEO), and poly(methacrylic acid-co-*tert* butyl methacrylate) (MAcoBMA) were synthesized and mixed with cobalt chloride in a common solvent at various concentrations to produce hybrid composites in order to be utilized as potential relative humidity (RH) photonic sensors.

The capability of the rapid prototyping soft lithographic techniques for the efficient replication of gratings with efficient incorporations of various sensing materials was demonstrated and compared to classical prototyping photolithographic techniques. Furthermore, a modified SAMIM technique with fewer processing steps in the production of the grating was proposed. It was demonstrated that for the range of materials used, the fabricated gratings were of excellent quality. Specifically, a method for the development of ammonia sensors using sol-gel materials was employed. In addition, a novel block copolymer sensitive material was successfully used demonstrating the hosting versatility of the platform for diverse materials. The obtained results confirm the efficient and low cost implementation of point gas sensors for a variety of measurands. By further optimizing the fabrication technique of the gratings and the sensing platform and by employing also customizable sensitive materials this sensing approach could attract a lot of interest in various applications.

Diffractive structures were successfully created on thin films by the aid of a materials printer. The scope of this work was the design, implementation and analysis of diffractive patterns with both organic and inorganic materials on silica substrates. Several designs were used, comprising diffraction gratings, crossed gratings and holographic masks. The diffractive structures can be used for photonic sensing applications.

A study on the design and fabrication of diffraction gratings for sensing applications was performed where ammonia detection was a case study. That study can be successfully used in other cases, by employing a different sensitive material in order to react with analytes, such as humidity or hydrocarbons. Diffraction gratings were also designed, fabricated and studied for temperature sensing, as multilayer metal oxides present an interesting behavior upon heating. Their temperature-sensitive behavior was found to be in good agreement with their theoretical performance estimated by rigorous coupled wave analysis. Their temperature sensitivity reached about 10% per ^{o}C, and establishes new concepts for photonic remote point sensing and would lead to further applications in information optics and photonics. Following that study, an evaluation of fabricated POF sensors for humidity and ammonia sensing was performed. The results could be evaluated for potential sensor optimization.

The composition of scattering and gradient radiation forces is now offering important tools for the manipulation of inorganic and biological matter by means of particle trapping using optical tweezers and structure actuation. Beyond these applications, the concept of light induced forces exerted in soft matter at the mesoscale, opens up new horizons by allowing efficient density manipulation and the formation of solid objects. Microstructure creation is implemented solely by the above optical means in semidilute, entangled polymer solutions with remarkable results. Pointing to an emerging microfabrication technology, especially suitable for photonic applications, several forms of structures in planar and three dimensional free standing micro-objects were demonstrated and discussed, in addition to a unique polymer fiber drawing operation, by the sole use of radiation forces. The observed phenomena are under further study but may be illustrated in terms of the synergy of radiation forces, chain entanglement and optical field structuring and optical waveguiding, as discussed in this work. The topic is opening a new area for fundamental investigations in polymer science and photonics. Emerging concepts on materials microstructuring in three dimensions would take advantage of the chemically inert nature of the process to yield a rich palette of microfabrication tools. These will offer compatibility with both inorganic devices and biological material, leading the way to hybridization and novel lab-on-chip schemes. The ability to tailor surfaces on the nanoscale with reversibility may also offer new tools in optical memory and related applications, also prompting to hybrid and unified approaches in photonics, information and biomedical technologies.

The capacity of laser light to structure and manipulate the materials to enable new functional forms for photonics has been the main motive throughout this work. The use of destructive - ablative - methods are proved invaluable for tailoring interfaces of sensitive materials in order to enhance functionalities. In a complementary manner radiation forces represent some constructive alternatives complementing the topic and offering alternative approaches towards novel concepts, enhanced methods and innovation in photonics.

Συμπεράσματα- Προοπτικές

Η παρούσα διδακτορική διατριβή αποσκοπεί στην σχεδίαση, κατασκευή και μελέτη μικροδομών με χρήση δεσμών λέιζερ για εφαρμογές φωτονικής. Η διατριβή μελετά την ανάπτυξη και ανάλυση αρκετών τεχνικών κατασκευής μικροδομών με ταυτόχρονη ανάπτυξη νέων, νανοσύνθετων φωτονικών υλικών για εφαρμογές αισθητήρων. Επιπρόσθετα, μελετά καινοτόμα φαινόμενα που σχετίζονται με την μικροδόμηση μαλακής ύλης, αμιγούς ή υβριδικής, με τη χρήση δυνάμεων ακτινοβόλησης λέιζερ και προτείνει πιθανή εξήγηση των πολύπλοκων αλλά ενδιαφερόντων φαινομένων που εμπλέκονται.

Συγκεκριμένα, μελετήθηκε η συμπεριφορά διαφόρων υλικών κατά την ακτινοβόλησή τους με λέιζερ με σκοπό να αποκαλυφθούν πιθανές λεπτομέρειες αλληλεπίδρασης λέιζερ-ύλης. Για το λόγο αυτό, ένα sol-gel υλικό (TMOS) ακτινοβολήθηκε με δύο πηγές λέιζερ στην φασματική περιοχή του υπεριώδους (Ar laser @ 193 nm and F_2 @157 nm). Βρέθηκε ότι η μορφολογία της επιφάνειας μεταβλήθηκε με ελεγχόμενο τρόπο με τις φυσικές και χημικές ιδιότητες να εξαρτώνται έντονα από τις συνθήκες ακτινοβόλησης. Η επεξεργασία της επιφάνειας με λέιζερ υπεριώδους είναι μια γενική προσέγγιση ενός βήματος που μπορεί να εφαρμοστεί επιτυχώς σε σύνθετα υλικά.

Στη συνέχεια, μελετήθηκε η επίδραση παλμών 193nm και 157nm, παρακολουθώντας την επιφάνεια πριν και μετά την έκθεση στο λέιζερ στοχεύοντας στην κατανόηση της επίδρασης της UV ακτινοβολίας στην δομή του υμενίου, στην μορφολογία της επιφάνειας και στην βελτιστοποίηση της επεξεργασίας σύνθετων υλικών. Η τροποποίηση της επιφάνειας των οργανικών υμενίων αναμένεται να ενισχύσει την απορρόφηση διαφόρων ανιχνεύσιμων χημικών αναλυτών. Παράλληλα, η χημική τροποποίηση της επιφάνειας με παλμούς 157nm ενισχύει τη δύναμη δεσμού στόχου-αισθητήρα και ως εκ τούτου την ευαισθησία ανίχνευσης σε εφαρμογές αισθητήρων. Η βελτιστοποίηση της διαδικασίας ακτινοβόλησης με excimer λέιζερ θα έχει ως αποτέλεσμα την βελτίωση της ποιότητας των δομών και της ακρίβειας των χαρακτηριστικών που κατασκευάζονται ώστε να επιτευχθούν διαδικασίες σε κλίμακα νανομέτρων, ανοίγοντας νέους ορίζοντες στην ανάπτυξη νανοδομών σε διάφορα πεδία εφαρμογών. Τα αποτελέσματα μπορούν να χρησιμοποιηθούν για τον σχηματισμό μικρο/νανοδομών σε υβριδικές φωτονικές και οπτοηλεκτρονικές συσκευές.

Επιπρόσθετα, υμένια Polydimethylsiloxane (PDMS) μελετήθηκαν κατά την ακτινοβόλησή τους με excimer λέιζερ (193nm). Τα δείγματα μελετήθηκαν πριν και μετά την χρήση λέιζερ με σκοπό την κατανόηση της επίδρασης της ακτινοβολίας UV στην χημική δομή και μορφολογία επιφανείας των υμενίων. Η ακτινοβόληση προκάλεσε φωτοδιαχωρισμό δεσμών που ακολουθήθηκε από τη δημιουργία νέων. Οι χημικές αλλαγές συνοδεύτηκαν από τροποποίηση της μορφολογίας επιφανείας. Ακόμη, μελετήθηκε η επίδραση της ακτινοβολίας λέιζερ στις ιδιότητες του υλικού για ένα υβριδικό υλικό, το TEOS-MAA-PEG:Au όπου ελήφθησαν ενδιαφέροντα αποτελέσματα σχετικά με την σκληρότητα του υλικού και των συνθηκών κατωφλίου αποδόμησης.

Η αρχή της μικροδόμησης με λέιζερ μελετήθηκε περαιτέρω και για άλλα υλικά και συσκευές. Πραγματοποιήθηκε μια ενδελεχής μελέτη της τροποποίησης επιφανείας πολυμερικών οπτικών ινών με δέσμη excimer λέιζερ (193nm) για εφαρμογές αισθητήρων. Η μελέτη περιελάμβανε ένα σετ πειραμάτων για τον καθορισμό του κατωφλίου αποδόμησης του PMMA (υλικό κατασκευής της ίνας) όπου παρατηρήθηκε ένα ενδιαφέρον φαινόμενο λόγω των διαφορετικών κατωφλίων αποδόμησης του πυρήνα και του μανδύα. Στη συνέχεια, δόθηκε έμφαση στην ταχεία προτυποποίηση και αναπαραγωγή μικροδομών που είχαν αρχικά σχεδιαστεί για συγκεκριμένες εφαρμογές φωτονικής. Η εργασία περιελάμβανε την σχεδίαση φραγμάτων περίθλασης διαφόρων χαρακτηριστικών. Για το λόγο αυτό χρησιμοποιήθηκε ειδικό λογισμικό CAD. Τα φράγματα περίθλασης χρησιμοποιήθηκαν στη συνέχεια για την ανάπτυξη πραγματικών συσκευών με την τεχνική της χάραξης με ενεργά ιόντα (Reactive Ion Etching) κυρίως για εφαρμογές αισθητήρων.

Η εργασία επεκτάθηκε στην σχεδίαση και άλλων οπτικών στοιχείων, όπως φακών Fresnel. Προκειμένου να πραγματοποιηθεί η σχεδίαση των φακών αυτών, έπρεπε να προηγηθεί υπολογισμός των ακτίνων κάθε ζώνης, ο οποίος ακολουθήθηκε από τη χρήση λογισμικού CAD. Τα τελικά σχέδια μεταφέρθηκαν σε πραγματικές συσκευές με την τεχνική RIE. Επιπροσθέτως, χρησιμοποιήθηκε ολογραφία με χρήση υπολογιστή (Computer Generated Holography) και προέκυψαν μάσκες πολύπλοκων σχημάτων και λειτουργικοτήτων. Για τη δημιουργία μασκών κυρίως για εφαρμογές διαχωρισμού δέσμης έγινε χρήση ειδικού λογισμικού για CGHs. Δημιουργήθηκε πληθώρα σχεδίων κάθε ένα από τα οποία είχε διαφορετικό οπτικό αποτέλεσμα, ανάλογα με τις ανάγκες. Όλα τα σχέδια μεταφέρθηκαν σε μεταλλικά υποστρώματα και μπορούν να χρησιμοποιηθούν σε πολλές εφαρμογές, επιδεικνύοντας έτσι την πολλαπλότητα εφαρμογών αυτών των συσκευών.

Επιπλέον, χρησιμοποιήθηκαν τεχνικές μαλακής λιθογραφίας για τη δημιουργία μικροδομών (φραγμάτων περίθλασης) για εφαρμογές αισθητήρων. Τα φράγματα περίθλασης κατασκευάστηκαν με αρνητική φωτολιθογραφία και τη χρήση εμπορικά διαθέσιμου φωτοευαίσθητου υλικού. Στη συνέχεια έγινε επίστρωση με ένα λειτουργικό υβριδικό στρώμα ώστε να προκύψει ένα πολύπλοκο σύστημα με διαμορφωμένο ενεργό δείκτη διάθλασης και προφίλ φράγματος. Χρησιμοποιήθηκαν δύο υλικά, poly(ethylene oxide) (PEO), και poly(methacrylic acid-co-*tert* butyl methacrylate) (MAcoBMA) τα οποία συντέθηκαν και αναμείχθηκαν με χλωρίδιο κοβαλτίου σε συνήθη διαλύτη σε διάφορες συγκεντρώσεις για τη δημιουργία υβριδικών σύνθετων που μπορούν να χρησιμοποιηθούν ως πιθανοί αισθητήρες σχετικής υγρασίας.

Παρουσιάστηκε η ικανότητα ταχείας προτυποποίησης με τεχνικές μαλακής λιθογραφίας για την αποτελεσματική αναπαραγωγή φραγμάτων περίθλασης με τη χρήση διαφόρων ευαίσθητων υλικών και συγκρίθηκε με κλασσικές τεχνικές φωτολιθογραφίας. Επιπρόσθετα, προτάθηκε μια τροποποιημένη τεχνική SAMIM με λιγότερα βήματα για την παραγωγή φραγμάτων περίθλασης. Αποδείχθηκε ότι για το φάσμα των υλικών που χρησιμοποιήθηκαν, τα φράγματα περίθλασης ήταν εξαιρετικής ποιότητας. Συγκεκριμένα, αναπτύχθηκαν αισθητήρες αμμωνίας χρησιμοποιώντας υλικά sol-gel. Επιπλέον, χρησιμοποιήθηκε επιτυχώς ένα καινοτόμο συμπολυμερές επιδεικνύοντας τις πολλαπλές δυνατότητες της πλατφόρμας. Τα αποτελέσματα επιβεβαιώνουν την αποτελεσματική και χαμηλού κόστους υλοποίηση αισθητήρων αερίων για μια ποικιλία αναλυτών. Βελτιστοποιώντας την διαδικασία κατασκευής των φραγμάτων περίθλασης και της πλατφόρμας ανίχνευσης, αλλά και τα υλικά που χρησιμοποιούνται, η συγκεκριμένη προσέγγιση ανίχνευσης θα μπορούσε να προσελκύσει αρκετό ενδιαφέρον σε διάφορες εφαρμογές.

Επιπλέον, δημιουργήθηκαν περιθλαστικές δομές σε λεπτά υμένια με τη βοήθεια ενός εκτυπωτή υλικών (materials printer). Ο σκοπός αυτής της εργασίας ήταν η σχεδίαση, υλοποίηση και ανάλυση περιθλαστικών μοτίβων σε οργανικά και ανόργανα υλικά πάνω σε υποστρώματα πυριτίου. Χρησιμοποιήθηκαν διάφορα σχέδια, συμπεριλαμβανομένων φραγμάτων περίθλασης και ολογραφικών μασκών. Οι περιθλαστικές δομές μπορούν να χρησιμοποιηθούν σε εφαρμογές φωτονικών αισθητήρων.

Πραγματοποιήθηκε μελέτη και κατασκευή φραγμάτων περίθλασης για εφαρμογές αισθητήρων όπου η ανίχνευση αμμωνίας ήταν μια μελέτη περίπτωσης. Η μελέτη μπορεί να χρησιμοποιηθεί και σε άλλες περιπτώσεις με διαφορετικό ευαίσθητο υλικό ώστε να αλληλεπιδράσει με αναλύτες, όπως υγρασία ή υδρογονάνθρακες. Επιπρόσθετα, σχεδιάστηκαν, κατασκευάστηκαν και μελετήθηκαν φράγματα περίθλασης ως αισθητήρες θερμοκρασίας, καθώς τα φράγματα περίθλασης πολυστρωματικών οξειδίων μετάλλων παρουσιάζουν ενδιαφέρουσα συμπεριφορά κατά τη θέρμανση. Η συμπεριφορά τους βρέθηκε σε καλή συμφωνία με τη θεωρητική τους απόδοση, η οποία πραγματοποιήθηκε με την μέθοδο της ακριβούς ανάλυσης συζευγμένων κυμάτων (rigorous coupled wave analysis). Η ευαισθησία τους έφτασε περίπου το 10% / ^{o}C και δημιουργεί νέους δρόμους στην φωτονική ανίχνευση απομακρυσμένου σημείου, καθώς θα μπορούσε να χρησιμοποιηθεί σε εφαρμογές φωτονικής και οπτικής πληροφορίας. Ακολούθως, δοκιμάστηκαν αισθητήρες πολυμερικών οπτικών ινών για ανίχνευση υγρασίας και αμμωνίας. Τα αποτελέσματα μπορούν να αξιολογηθούν για την βελτιστοποίηση αισθητήρων.

Η σύνθεση των δυνάμεων σκέδασης και βαθμίδας ακτινοβόλησης προσφέρει σημαντικά εργαλεία για τον έλεγχο ανόργανης και βιολογικής ύλης με μέσο την παγίδευση σωματίων χρησιμοποιώντας οπτικές λαβίδες. Πέρα από τις εφαρμογές αυτές, η ιδέα των δυνάμεων που προκαλούνται από φως και ασκούνται σε μαλακή ύλη ανοίγει νέους ορίζοντες καθώς επιτρέπει τον αποτελεσματικό χειρισμό και σχηματισμό στερεών αντικειμένων. Η δημιουργία μικροδομών υλοποιείται με χρήση μόνο της παραπάνω ιδέας σε διαλύματα πολυμερών εναγκαλισμένων αλυσίδων με αξιοσημείωτα αποτελέσματα. Στοχεύοντας σε μια αναδυόμενη τεχνολογία μικροδόμησης, κατάλληλη για εφαρμογές φωτονικής, παρουσιάστηκαν και συζητήθηκαν διάφοροι σχηματισμοί δομών επίπεδων και τρισδιάστατων μικροαντικειμένων ελευθέρου χώρου, σε συνδυασμό με μια μοναδική τεχνική κατασκευής ινών (fiber drawing), με χρήση μόνο δυνάμεων ακτινοβόλησης. Τα παρατηρούμενα φαινόμενα βρίσκονται υπό μελέτη, αλλά εξηγούνται ως συνέργεια δυνάμεων ακτινοβόλησης, εναγκαλισμού αλυσίδων και διαμόρφωσης οπτικού πεδίου και οπτικής κυματοδήγησης, όπως μελετάται σε αυτή την εργασία. Το θέμα ανοίγει μια νέα περιοχή θεμελιωδών μελετών στην φυσική των πολυμερών και της φωτονικής. Τα αναδυόμενα θέματα της μικροδόμησης υλικού σε τρεις διαστάσεις μπορούν να ωφεληθούν από την χημικά αδρανή φύση της διαδικασίας με σκοπό την απόκτηση μιας πλούσιας παλέτας εργαλείων μικροδόμησης. Αυτά θα προσφέρουν συμβατότητα τόσο με ανόργανες όσο και με οργανικές συσκευές και βιολογικά υλικά, προωθώντας την ιδέα του υβριδισμού σε συστήματα lab-on-chip. Η δυνατότητα της σχεδίασης επιφανειών σε νανοκλίμακα με αντιστρεπτότητα ενδέχεται να προσφέρει νέα εργαλεία στην οπτική μνήμη και σχετιζόμενα πεδία, παρακινώντας υβριδικές και ενοποιημένες προσεγγίσεις στις τεχνολογίες φωτονικής, πληροφορίας και βιοϊατρικής.

Η δυναμική του φωτός λέιζερ να διαμορφώνει και να ελέγχει υλικά για την ενδυνάμωση νέων λειτουργικών σχηματισμών είναι το κύριο κίνητρο σε όλη την παρούσα εργασία. Η χρήση καταστρεπτικών-φωτοαποδομήσιμων μεθόδων αποδεικνύεται ανεκτίμητη για τη διαμόρφωση διεπιφανειών ευαίσθητων υλικών με σκοπό την ενίσχυση των λειτουργικοτήτων τους. Ως μια συμπληρωματική δράση, οι δυνάμεις ακτινοβόλησης αναπαριστούν κατασκευαστικές εναλλακτικές, προσφέροντας νέες ιδέες για μεθόδους και καινοτομικότητες στην φωτονική.

APPENDIX 1

Papers in peer-reviewed journals

1) Meristoudi A., Athanasekos L., Vasileiadis M., Pispas S., Mousdis G., Karoutsos E., Alexandropoulos D., Du H., Tsigara A., Kibasi K., Perrone A. and Vainos N. A., "Nanocomposite hybrid photonic media for remote point sensors", J. of Optics A: Pure and Applied Optics, 11 (2009)

2) Vasileiadis M., Athanasekos L., Meristoudi A., Alexandropoulos D., Mousdis G., Karoutsos E., Botsialas A., and Vainos N., "Diffractive Optic Sensor for Remote Point Detection of Ammonia", Optics Letters, 35, 9 (2010)

3) Athanasekos L., Kollia Z., Vasileiadis M., Aspiotis N., Alexandropoulos D., Meristoudi A., Karoutsos V. and Sarantopoulou E., "Effect of 193 nm and 157 nm laser light illumination on surface properties of TMOS-$NiCl_2$ sol-gel derived material", J. of Optics, 12 124015 (2010)

4) Athanasekos L., Vasileiadis M., Tsigara A., Kaminska E., Piontrowska A., Sigalas M., and Vainos N., "Multilayer metal/metal-oxide diffractive structure for photonic temperature sensing", Optics Letters, 35, 23 (2010)

5) Vasileiadis M., Alexandropoulos D., Athanasekos L., Karoutsos V., Sigalas M., and Vainos N., "Optimized design of remote point diffractive optical sensors", J. of Optics, 12 124016 (2010)

6) Athanasekos L., Vasileiadis M., Mantzaridis C., Karoutsos V. C., Koutselas I., Pispas S. and Vainos N. A., "Micro-fabrication by laser radiation forces: A direct route to reversible free-standing threedimensional structures", Optics Express 20, 22, 24735 (2012)

7) Aspiotis N., El Sachat A., Athanasekos L., Vasileiadis M., Mousdis G., Pispas S., Vainos N. and Riziotis C., "Diffractive Optical Ammonia Sensors Based on Sol-Gel Nanocomposites Materials", Sensor Letters 11, 1415 (2013)

8) Athanasekos L., El Sachat A., Pispas S. and Riziotis C., "Amphiphilic diblock copolymer-based multiagent photonic sensing scheme", J. Polym. Sci. B Polym. Phys., 52, 46 (2014)

Book Chapters

Athanasekos L., Pispas S. and Vainos N. A., “Laser-induced soft matter organization and microstructuring of photonic materials”, Chapter in book “Laser growth and processing of photonic devices”, Woodhead Publishing, ISBN 1 84569 936 X, ISBN-13: 978 1 84569 936 9, (2012)

Papers in Conference Proceedings

1) Madamopoulos N., Pispas S., Tsigara A., Athanasekos L., Mountrichas G., Gatsouli K., Kibasi K. and Vainos N., “Polymer based photonic sensors for physicochemical monitoring”, Proc. of SPIE Vol. 5993, 599308 (2005)

2) Tsigara A., Madamopoulos N., Hands M., Athanasekos L., Meristoudi A., Mousdis G., Manasis G., Koutselas I., Vainos N. A., “$NiCl_2/SiO_2$ Sol-gel Material for Ammonia Sensing”, Proc. of SPIE 6377 (2006)

3) Tsigara A., Athanasekos L., Meristoudi A., Manasis G., Hands M., Mousdis G., Pispas S., Vainos N. A., “Inorganic and hybrid polymer-inorganic nanostructured materials for optical physicochemical sensing applications”, Proc. of SPIE, 6785 (2007)

4) Athanasekos L., Dimas D., Katsikas S., Pispas S., Vainos N., Boucouvalas A.C. , and Riziotis C., “Laser microstructuring of polymer optical fibres for enhanced and autonomous sensor architectures”, Proc. Eurosensors XXV, September 4-7,Athens, Greece, in Procedia Engineering (2011)

5) Riziotis C., Athanasekos L., Vasileiadis M., Dimas D., Pispas S., and Vainos N., “Laser Microstructured Polymer Optical Fibres for Optimised Sensing Devices”, Proceedings of the 20th International Conference on Plastic Optical Fibers, September 14-16, Bilbao, Spain (2011)

6) Athanasekos L., Pispas S., Riziotis C., “Novel block copolymers for multi-agent detection using polymer optical fibers”, Proc. SPIE 8426, Microstructured and Specialty Optical Fibres, 842615, 1 June, (2012)

7) Aspiotis N., El Sachat A., Athanasekos L., Vasileiadis M., Mousdis G., Pispas S., Vainos N. and Riziotis C., “Ultra Low Cost Rapid Prototyping Of Diffraction Grating Remote Point Gas Sensors”, Key Engineering Materials 543, 377 (2013)

8) Athanasekos L., Aspiotis N., El Sachat A., Pispas S., and Riziotis C., “Novel Approach For Lysozyme Detection Employing Block Copolymer Overlayers on Plastic Optical Fibers”, Key Engineering Materials 543, 385 (2013)

Conferences

Madamopoulos N., Siganakis G., Tsigara A., Athanasekos L., Pispas S., Vainos N., Kaminska E., Piotrowska A., Perrone A., Kibasi K., “Diffractive optical elements for photonics gas sensors”, Optics East 23-25 October, Boston Massachussets, USA (2005)

Meristoudi A., Tsigara A., Athanasekos L., Hands M., Pispas S., Vainos N., and Du H.L., “Polymer/Ag, Au and sol-gel /Ag, Au, derived thin film photonic structures for sensing applications”, 8th ESG conference on Glass Science and Technology, 10-14 September, Sunderland, UK (2006)

Athanasekos L., Vasileiadis M., Meristoudi A., Pispas S., Mousdis G., Tsigara A., Karoutsos V., and Vainos N. A., “Diffractive Optic Nanocomposite Sensors”, 5th International Conference on Nanosciences & Nanotechnologies - NN08, 14-16 July, Thessaloniki, Greece (2008)

Vasileiadis M., Athanasekos L., Meristoudi A., Pispas S., Mousdis G., Tsigara A., Karoutsos V., and Vainos N. A., “Photonic Methods and Materials for remote point etching”, COST Training School (COST ACTION MP0604), 2-5 September, Ischia (Naples), Italy (2008)

Athanasekos L., Vasileiadis M., Meristoudi A., Pispas S., Mousdis G., Alexandropoulos D., Karoutsos V., and Vainos N. A., “Diffractive Optical Elements and Novel microstructures for photonic applications”, COST Training School (COST ACTION MP0604), 2-5 September, Ischia (Naples), Italy (2008)

Vasileiadis M., Athanasekos L., Meristoudi A., Pispas S., Mousdis G., Tsigara A., and Vainos N. A., “Hybrid materials photonic sensors”, XXIV Panhellenic Conference on Solid State Physics & Materials Science, September 21-24, Heraklion, Crete, Greece, (2008)

Athanasekos L., Alexandropoulos D., Vasileiadis M., Karoutsos E., Pispas S., Mousdis G., Meristoudi A., Botsialas A.and Vainos N. A., “Hybrid materials photonic structures microetching and applications”, XXIV Panhellenic Conference on Solid State Physics & Materials Science, September 21-24, Heraklion, Crete, Greece, (2008)

Vasileiadis M., Athanasekos L., Alexandropoulos D., Meristoudi A., Botsialas A., Mousdis G., and Vainos N.,“Optical Sensor Sensitivity Enhancement by Use of Diffraction Gratings”,ICO - Emerging Trends and Novel Materials in Photonics - October 7-9, , Delphi, Greece (2009)

Athanasekos L., Mantzaridis C., Pispas S.and Vainos N. A., “Novel micro-nanostructures of common polymers in thin films for photonic applications”, ICO - Emerging Trends and Novel Materials in Photonics - October 7-9, , Delphi, Greece (2009)

Pavani K., Athanasekos L., Martin S., Vainos N. A., Toal V., Naydenova I., “A new low cost manufacturing technique for optical elements”, ICO - Emerging Trends and Novel Materials in Photonics - October 7-9, Delphi, Greece (2009)

Athanasekos L., Vasileiadis M., Tsigara A., Sigalas M.M. and Vainos N.A., ”Multilayer oxide grating photonic temperature sensor”, 2nd Mediterranean Conference on NanoPhotonics, MEDINANO-2, 26-27 October, Athens, Greece (2009)

Vasileiadis M., Athanasekos L., Alexandropoulos D., Meristoudi A., Botsialas A., Mousdis G., Karoutsos V., and Vainos N.A , “Sensitivity Enhancement of Ammonia Photonic Sensor by Surface Relief Modulation”, 2nd Mediterranean Conference on NanoPhotonics, MEDINANO-2 , 26-27 October, Athens, Greece (2009)

Vainos N. A., Athanasekos L., Vasileiadis M., Meristoudi A., Mantzaridis Ch., Karoutsos V., Alexandropoulos D., Pispas S.and Sigalas M., “Photonic interfaces: Laser tailoring of nanocomposites for sensor and other applications”, 7th International Conference on Nanosciences & Nanotechnologies – NN10, 11-14 July, Ouranoupolis Halkidiki, Greece (2010)

Athanasekos L., Mantzaridis C., Karoutsos V., Pispas S. and Vainos N. A., “Micro-Nanopatterning of Common Polymers Thin Films and Sculpturing of Free Standing Structures by Direct Laser Writing for Photonic Applications”, XXVI Panhellenic conference in solid state physics and materials science, 26-29 September, Ioannina, Greece (2010)

Vainos N. A., Athanasekos L., Vasileiadis M., Alexandropoulos D., Karoutsos V., Sigalas M., “Photonic interfacing by laser light: structures and applications”, XXVI PanHellenic Conference on Solid State Physics and Materials Science, Ioannina, September 26-29 (2010)

Vasileiadis M., Athanasekos L., Alexandropoulos D., Meristoudi A., Karoutsos V., Sigalas M.and Vainos N., “Diffraction Grating Thin Film Sensors Operating Under The Remote Point Optical Sensing Scheme”XXVI PanHellenic Conference on Solid State Physics and Materials Science, Ioannina, September 26-29 (2010)

Athanasekos L., Mantzaridis C., Karoutsos V., Pispas S. and Vainos N. A., “Polymer Microstructure Formation by Direct Laser Patterning and Sculpturing for Photonic Applications”, COST Training School, Optical Micro-Manipulation by Nonlinear Nanophotonics, Visegrád, Hungary, October 5-8 (2010)

Vasileiadis M., Athanasekos L., Alexandropoulos D., Karoutsos V., Sigalas M., and Vainos N.,“Theoretical study and experimental demonstration of diffraction grating sensors sensitivity enhancement”COST Training School (COST ACTION MP0604), October 5-8, Visegrád, Hungary (2010)

Athanasekos L., Mantzaridis C., Alexandropoulos D., Karoutsos V., Pispas S. and Vainos N. A., “ Novel Polymer Microstructure Formation by Direct Laser Patterning and Sculpturing for Photonic Applications”, 2nd Mediterranean Photonics Conference, 29 November – 2 December, Eilat, Israel (2010)

Vainos N.A., Athanasekos L., Vasileiadis M., Mantzaridis Ch., Karoutsos V. C., Koutselas I., and Pispas S., “Microsolid formation by laser radiation forces”, 8th International Conference on Nanosciences & Nanotechnologies – NN11, 12-15 July, Thessaloniki, Greece (2011)

Vasileiadis M., Aspiotis N., Athanasekos L., Alexandropoulos D., Meristoudi A., Karoutsos V., Sigalas M. and Vainos N. A., “UV Laser Microetching and Soft Lithography for Diffractive Optic Sensors”, 8th International Conference on Nanosciences & Nanotechnologies – NN11, 12-15 July, Thessaloniki, Greece (2011)

Orphanos Y., Brezas S., Bakarezos M., Vasileiadis M., Alexandropoulos D., Athanasekos L., Tatarakis M., Vainos N.,. Papadogiannis N.A, “3D-detection of nanosecond laser generated high frequency micro-elastic waves in metal films”, 8th International Conference on Nanosciences & Nanotechnologies – NN11, 12-15 July, Thessaloniki, Greece (2011)

Clarke G., Pavani K., Athanasekos L., Martin S., Vainos N. A., Toal V., Naydenova I., “Dye deposition lithography – a versatile method for fabrication of optical fan-out devices”, International Commission of Optics conference, 15-19 August, Puebla, Mexico (2011)

Athanasekos L., Dimas D., Katsikas S., Pispas S., Vainos N., Boucouvalas A.C. and Riziotis C., “Laser microstructuring of polymer optical fibres for enhanced and autonomous sensor architectures”, Eurosensors XXV, September 4-7, Athens, Greece (2011)

Athanasekos L., Riziotis C., Vasileiadis M., Dimas D., Pispas S.and Vainos N., “ Laser Microstructured Polymer Optical Fibres for optimized sensing devices”, 20th International Conference on Plastic Optical Fibers – POF 2011, September 14-16, Bilbao, Spain (2011)

Athanasekos L., Pispas S.and Riziotis C., "Novel block copolymers for multi-agent detection using polymer optical fibers", SPIE Photonics Europe 2012, 16-19 April, Brussels, Belgium (2012)

Aspiotis N., Vasileiadis M., El Sahat A., Athanasekos L., Pispas S., Vainos N.A., Riziotis C, Ultra Low Cost Rapid Prototyping of Diffraction Grating Remote Point Sensors, nternational Conference on Materials and Applications for Sensors and Transducers, May 24-28, Budapest, Hungary (2012)

Athanasekos L., Aspiotis N, Pispas S, Riziotis C, Novel Approach For Lysozyme Detection Employing Block Copolymer Overlayers on Plastic Optical Fibers, International Conference on Materials and Applications for Sensors and Transducers, May 24-28, Budapest, Hungary (2012)

Vasileiadis M., Athanasekos L., Alexandropoulos D., Karoutsos V., Koutselas I., Pispas S., and Vainos N. A., “Advanced photonic structures via193 nm excimer laser microfabrication”, 10th International Conference on Nanosciences & Nanotechnologies – NN13, Porto Palace Conference Centre & Hotel, Thessaloniki, Greece, 9 - 12 July (2013)

Athanasekos L., Vasileiadis M., Pispas S., and Vainos N. A., “Radiation Forces as a Novel Micropatterning Tool”, 10th International Conference on Nanosciences & Nanotechnologies – NN13, Porto Palace Conference Centre & Hotel, Thessaloniki, Greece, 9 - 12 July (2013)

Athanasekos L., Vasileiadis M., El Sachat A., Riziotis C.and Vainos N. A., “Study on ArF excimer laser micromachining on Polymer Optical Fibers for photonic sensor applications”, 10th International Conference on Nanosciences & Nanotechnologies – NN13, Porto Palace Conference Centre & Hotel, Thessaloniki, Greece, 9 - 12 July (2013)

Vasileiadis M., Athanasekos L., Alexandropoulos D., Karoutsos V., Koutselas I., Pispas S., and Vainos N. A., “Design, synthesis and evaluation of polymer/quantum dot nanocomposites for integrated photonic circuits”, 10th International Conference on Nanosciences & Nanotechnologies – NN13, Porto Palace Conference Centre & Hotel, Thessaloniki, Greece, 9 - 12 July (2013)

APPENDIX 2

Multilayer metal/metal oxide diffraction gratings

Sample (numbers in nm)	**Code No**	**Comments**
Ru ...(illegible)	7 (red), 4 (black)	
$Pt/SnO_2/Pt/SnO_2/Pt/SnO_2/Pt$ (100/180/5/180/5/180/5)	5 (black)	4X4 μm
$Pt/SnO_2/Pt/SnO_2/Pt/SnO_2/Pt$ (20/200/2/200/2/200/2)	3 (red), 4 (black)	annealed
$Au/SnO_2/Au$ (100/340/5)	7 (black)	2X2 μm
$Ru/SnO_2/Ru$ (5/230/5)	4 (red)	
$Pt/SnO_2/Pt$ (100/340/5)	8 (black)	2X2 μm
$Pd/SnO_2/Pd$ (100/720/5)	6 (black)	4X4 μm
$Pt/SnO_2/Pt$ (100/632/5)	2 (black)	4X4 μm
ZnO (220 + 780)		grating 2x2 μm
Glass/SnO_2:N	11 (black)	by oxidation of Sn-N
$Pt/SnO_2/Pt$ (100/158/5)	3 NEW (black)	3 pieces
SnO_2 (d= 700)	9 (black)	
$Ru/SnO_2/Ru$ (100/450/5)	5 (red)	annealed
Glass/ ZnO:N	13(black)	by oxidation of Zn-N
$SnCl_2/Au/SnCl_2$ (300/10/300)	10 (black)	RTP: 500^o/ 10 min-N_2
$Pt/SnO_2/Pt/SnO_2/Pt$ (100/170/5/170/5)	1 (black)	4X4 μm
SnO_2 (1000)		period 2 μm 4 μm, groove depth ~

		800nm(RIE -> BU3)
ZnO/Au/ZnO (300/96/300)	12(black)	Zn 30 % O_2
Pd/SnO_2/Pd (100/450/5)	2 (black), 2 (red)	
Pt/SnO_2/Pt (100/720/5)	4 (black)	4X4 μm
SnO_2 (220 + 600)		grating 2/2 μm
Pd/SnO_2/Pd (5/230/5)	1 (black, 1(red)	

Table A1: Concise table of gratings tested

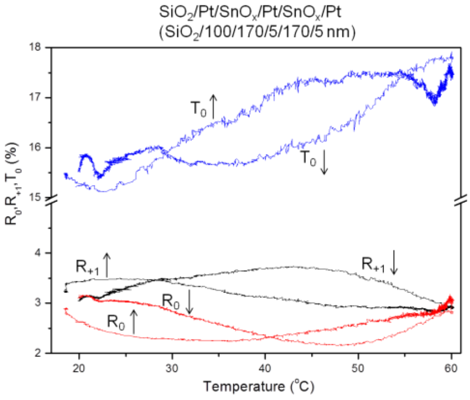

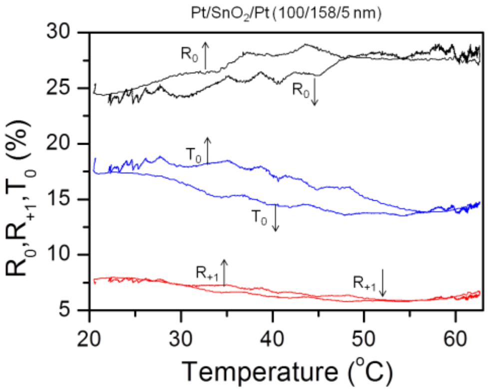

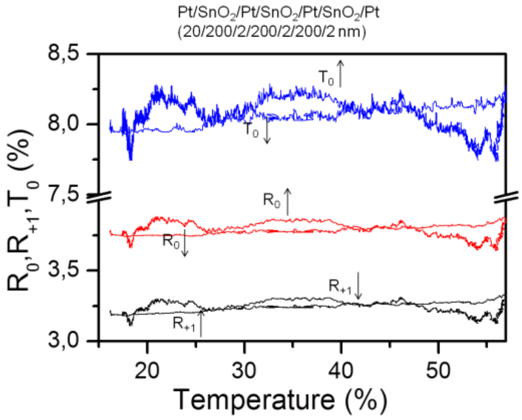

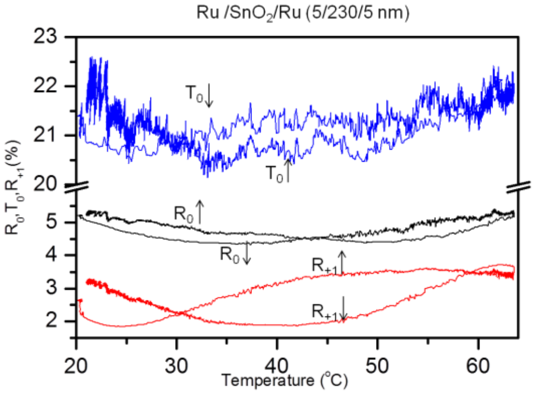

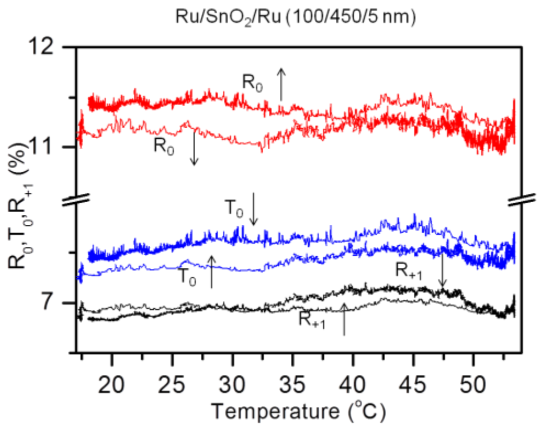
Ru/SnO$_2$/Ru (100/450/5 nm)
R_0, T_0, R_{+1} (%)
12
11
7
R_0
T_0
R_{+1}
20 25 30 35 40 45 50
Temperature (°C)

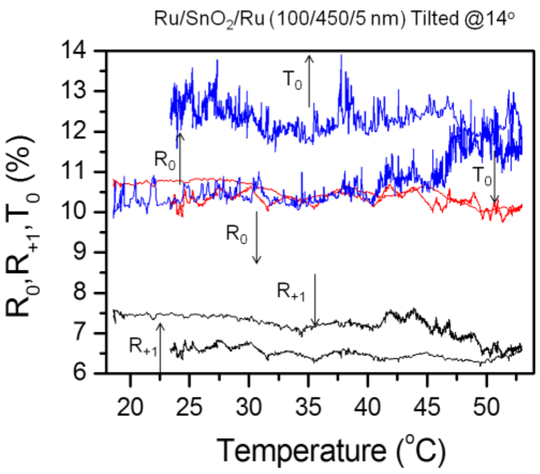
Ru/SnO$_2$/Ru (100/450/5 nm) Tilted @14°
R_0, R_{+1}, T_0 (%)
14 13 12 11 10 9 8 7 6
T_0
R_0
R_{+1}
20 25 30 35 40 45 50
Temperature (°C)

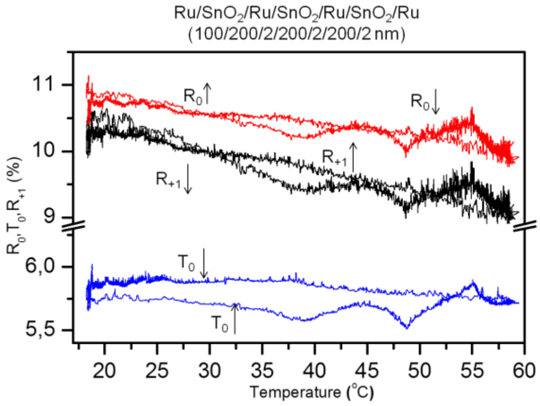
Ru/SnO$_2$/Ru/SnO$_2$/Ru/SnO$_2$/Ru
(100/200/2/200/2/200/2 nm)
R_0, T_0, R_{+1} (%)
11
10
9
6,0
5,5
R_0
R_{+1}
T_0
20 25 30 35 40 45 50 55 60
Temperature (°C)

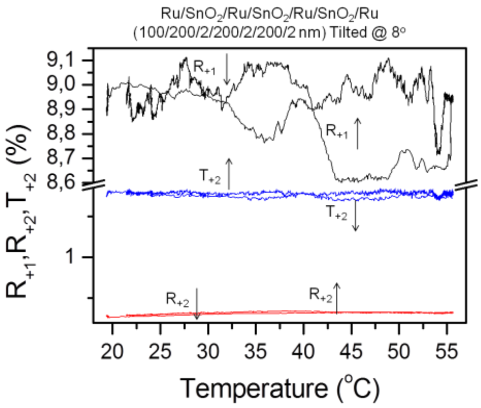
Ru/SnO$_2$/Ru/SnO$_2$/Ru/SnO$_2$/Ru
(100/200/2/200/2/200/2 nm) Tilted @ 8°
R_{+1}, R_{+2}, T_{+2} (%)
9,1 9,0 8,9 8,8 8,7 8,6
1
R_{+1}
T_{+2}
R_{+2}
20 25 30 35 40 45 50 55
Temperature (°C)

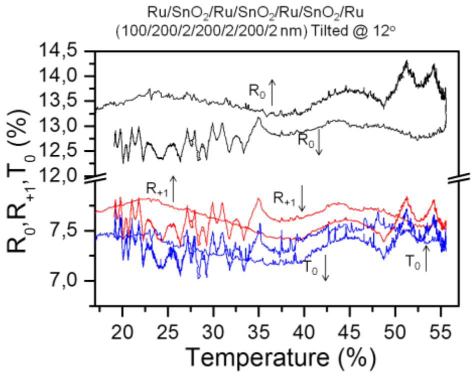
Ru/SnO$_2$/Ru/SnO$_2$/Ru/SnO$_2$/Ru
(100/200/2/200/2/200/2 nm) Tilted @ 12°
R_0, R_{+1}, T_0 (%)
14,5 14,0 13,5 13,0 12,5 12,0
7,5
7,0
R_0
R_{+1}
T_0
20 25 30 35 40 45 50 55
Temperature (%)

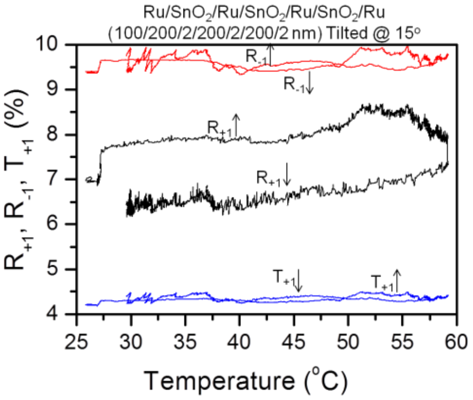
Ru/SnO$_2$/Ru/SnO$_2$/Ru/SnO$_2$/Ru
(100/200/2/200/2/200/2 nm) Tilted @ 15°
R_{+1}, R_{-1}, T_{+1} (%)
10 9 8 7 6 5 4
R_{-1}
R_{+1}
T_{+1}
25 30 35 40 45 50 55 60
Temperature (°C)

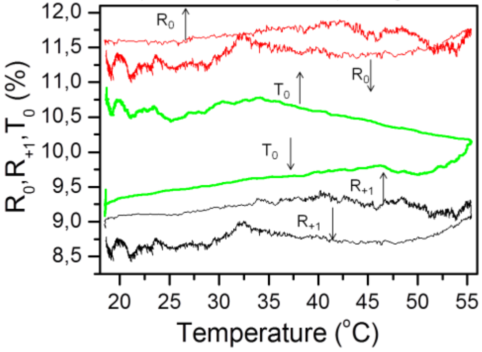
Ru/SnO$_2$/Ru/SnO$_2$/Ru/SnO$_2$/Ru (100/200/2/200/2/200/2 nm) Tilted @ 18°

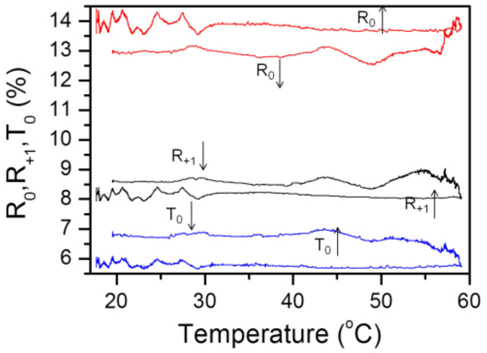
Ru/SnO$_2$/Ru/SnO$_2$/Ru/SnO$_2$/Ru (100/200/2/200/2/200/2 nm) Tilted @ 20°

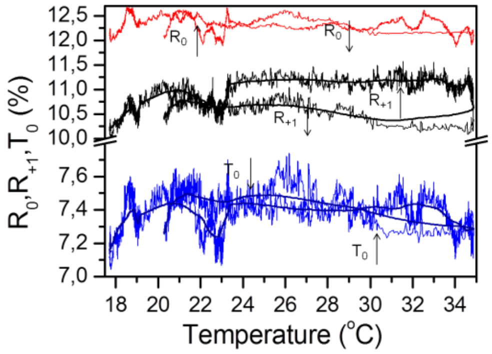
Ru/SnO$_2$/Ru/SnO$_2$/Ru/SnO$_2$/Ru (100/200/2/200/2/200/2 nm) Tilted @ 25°

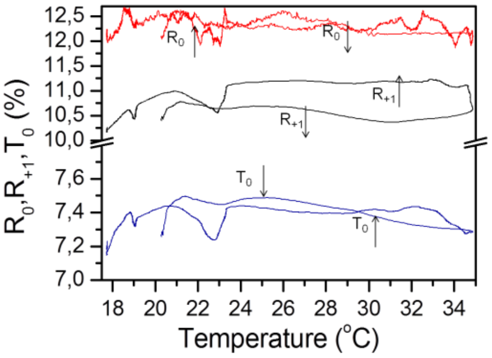
Ru/SnO$_2$/Ru/SnO$_2$/Ru/SnO$_2$/Ru (100/200/2/200/2/200/2 nm) Tilted @ 25°

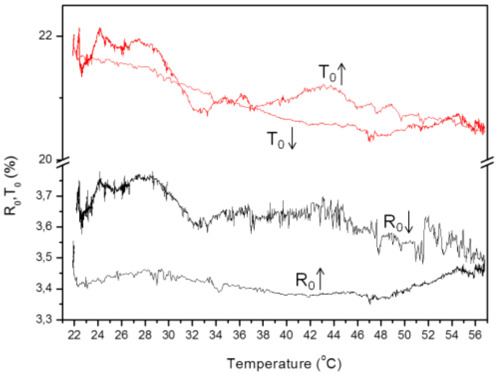
ZnO/glass (220/780 nm)

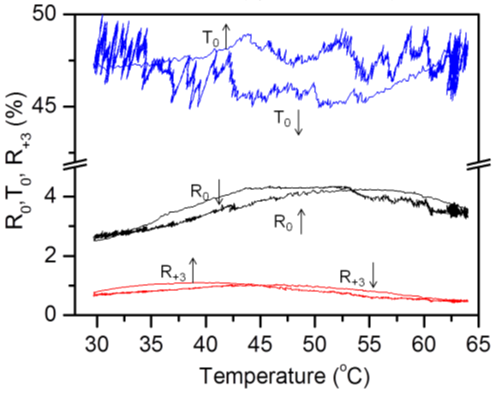
Glass/ZnO-N (by oxidation of Zn-N)

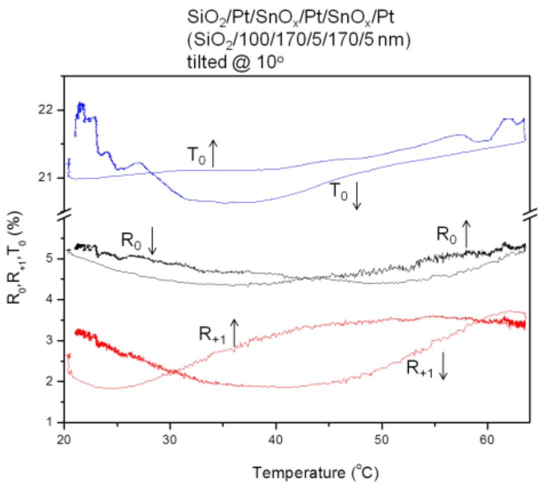

Figure A2: Sensor response curves for elevating temperatures in the case of various multilayer diffraction gratings.